
Search for Neutrinos Associated with
Gravitational Waves in
Super-Kamiokande

2021, March

Wenjie Ma

*Graduate School of Natural Science and Technology
(Master's Course)*

Okayama University

Abstract

This thesis focuses on neutrino searching associated with gravitational waves in Super-Kamiokande(SK) which is the largest Water-Cherenkov detector with the sensitivity of MeV to TeV. We get gravitational information from gravitational detector LIGO/VIRGO which was restarted in April 2019 called O3. O3 has improved sensitivity, and 56 gravitational waves quick alerts have already been observed and ended in April 2020. And at the catalogs of LIGO/VIRGO, they update data from Apr.2019 to Sep.2019 called O3a, reported 39 gravitational waves events. Gravitational waves can be generated by various processes such as the combination merger of black holes and black holes, the merger of neutron stars. Among them, the merger of neutron stars is considered to produce neutrino signals. If this kind of neutrino signal can be observed by us, it will have extremely profound significance for the study of the specific physical process of neutron star assembly and synthesis products. Immediate observation of neutrinos is considered to be important for transmitting the neutrino search results to the optical telescope in conjunction with the gravitational wave signal. For this, an automatic analysis system is needed. The purpose of this research is to create this automatic analysis system and search for neutrinos derived from gravitational waves.

In order to cover a very wide range of neutrino spectra, both low-energy (7–100 MeV) and high-energy (0.1–105 GeV) samples were analyzed. O3a reported the tracking of 36 gravitational waves (39 in total) and checked 2 catalogs. From the result in this study, in high energy region (from 100 MeV to 10 TeV), 10 neutrinos were observed, and the expected event was 4.8 (2σ) in high-energy. In low-energy (from 3.5 MeV to 100 MeV) for each event, the max observed signals are 3 events/1000s as the expected event was 0.729 /1000s (2σ).

In the first chapter, this thesis will discuss Einstein's theory of relativity and the generation of gravitational waves. In addition, the binary star system that can generate gravitational waves is explained. The neutron star merger is considered to be capable of generating neutrinos. According to different theoretical predictions, the energy of the generated neutrinos is also different. The main goal of this thesis is to detect neutrinos so that we can better understand the process of binary star system. The second chapter of this paper mainly introduces the super-Kamiokade(SK) detector, the main detector for detecting neutrinos. Introduce the history of the detector, the principle of detection (via Cerenkov light), and the operating system in SK. Chapter 3 mainly introduces the LIGO/VIRGO detectors of gravitational waves. The detection of gravitational waves is mainly carried out by the Michelson interferometer, and LIGO/VIRGO has the most sensitive Michelson interferometer (4km arm) in the world. In this chapter, I will introduce the history of LIGO/VIRGO and the detection principle of Michelson interferometer, as well as how to obtain the mass, distance and other data of the satellite system through the detected frequency. Chapter 4 mainly introduces the work of this paper: how to build an automated system that can automatically obtain gravitational wave data from LIGO/VIRGO and analyze it from the two region of high energy and low energy. Among them, in the low energy range (3.5MeV to 100MeV), because the background is not stable, after analyzing the energy higher than 3.5MeV, 5MeV, 6MeV, and 7MeV, it is decided to cut the data at 7MeV as the result of this detection. Chapter 5 mainly introduces the result processing and analysis in the two ranges of high energy and low energy respectively, and analyzes the sensitivity of the detected events. First, the data in the two energy ranges are analyzed by simple Poisson distribution. The results show that there is no neutrino signal. Then, in the high-energy range, considering the direction, energy, and location of gravitational waves, the Lambda and chi-square methods were used to analyze them, and the results showed that the neutrino signal was still not found. Although the neutrino signal could not be found, the upper limit of neutrino was still calculated, and the isotropic total neutrino energy was calculated at the same time. Chapter 6 mainly introduces the output results of the automation system. Chapter 7 and Chapter 8 respectively show the results of O3 and O3a of this research. The results show that there is no significant signal found.

Contents

1	Introduction	4
1.1	Gravitational waves	4
1.1.1	Newtonian gravity	4
1.1.2	Special relativity	4
1.1.3	Relativistic gravity	5
1.2	Binary star system	5
1.3	Neutrino	6
2	Super-Kamiokande(SK)	7
2.1	Detector Overview	7
2.2	SK history	7
2.3	Detector Principle	8
2.4	Photomultiplier Tubes	8
2.5	Water Systems	10
2.6	Radon Free Air Systems	10
2.7	Front-end Electronics and Data Acquisition System	12
2.8	Monitoring system	12
3	LIGO/VIRGO Detector	14
3.1	Introduction	14
3.2	Detector Principle	14
3.3	History	15
3.4	Signal Display	17
4	Automatic system and methods	21
4.1	Alert receiver and alert database	21
4.1.1	GCN Notice	21
4.1.2	GCN Notice receiver	21
4.2	High Energy analysis	23
4.2.1	Event selection	24
4.2.2	Background estimation and characteristics	25
4.2.3	Signal characteristics	26
4.2.4	Outputs	30
4.3	Low Energy analysis	32
4.3.1	Event selection	33
4.3.2	Background estimation and characteristics	34
4.3.3	Outputs	35
5	Statistical analysis	36
5.1	Introduction	36
5.1.1	Super-Kamiokande approach in previous analyses	36
5.2	Signal significance: first approach	37
5.3	Flux limits: sample-by-sample, position dependent	38
5.4	Flux limits: sample-by-sample, marginalised	41
5.5	Combined statistical analysis	42
5.5.1	Lambda method	42
5.5.2	Chi-square method	45
5.6	Flux limits: combined	49
5.6.1	Signal simulation	49
5.6.2	Marginalised limits	49
5.7	Isotropic total neutrino energy limits	51
5.7.1	High Energy sample	51
5.7.2	Low Energy sample	51

6	Result merger and result database	53
6.1	Inventory of different results	53
6.1.1	Alert receiver	53
6.1.2	High Energy analysis	53
6.1.3	Low Energy analysis	54
6.2	Output processing	54
6.3	Output formats	56
6.3.1	Results database	56
6.3.2	Web page	56
6.3.3	PDF	56
7	Follow-up of O3 real-time events	58
7.1	All GW triggers	58
8	Follow-up of O3a catalogued events	61
8.1	All GW triggers	61
8.2	Flux limits and Fluence limits	64
8.3	Total energy limits	66
9	Summary and Outlook	68
9.1	Summary	68
9.2	Outlook	68

1 Introduction

1.1 Gravitational waves

Gravitational waves were proposed by Henry Poincaré in 1905. They are disturbances in the curvature of space and time produced by accelerating masses and propagate from their source at the speed of light. Then in 1916, Albert Einstein made a prediction based on his theory of relativity. Gravitational wave is a wave similar to electromagnetic radiation, which transmits energy as gravitational radiation. In classical mechanics, according to Newton's law of universal gravitation, their existence is not stipulated, because Newtonian mechanics is based on the assumption that physical interaction is instantaneous (infinite speed) propagation.

1.1.1 Newtonian gravity

First, we conduct a qualitative analysis of gravitational waves. Gravitational radiation is a natural result of gravitational interaction. Then, compare the characteristics of gravitational waves and electromagnetic waves predicted by general relativity

Among the four basic interactions known in nature, the first to be discovered, described and modeled is universal gravitation. The law of universal gravitation was first published in 1687. The law states that two large point-shaped objects are attracted to each other by a force \vec{F} , and the force paradigm is $|\vec{F}| = Gm_1m_2/r^2$ is proportional to their masses m_1 and m_2 , and inversely proportional to the square of their interval r , where G is a universal constant. Recall that this force originates from the local potential Φ . A common form of Newton's law is the Poisson equation:

$$\nabla^2\Phi = 4\pi G\rho \quad (1)$$

with ρ the mass density of matter, acting as the source of the gravitational potential Φ . Hence, in Newtonian gravity, the gravitational interaction acts instantaneously. This was already of some concern to Newton himself, but it clearly became a significant problem with the advent of Einstein's theory of special relativity.

1.1.2 Special relativity

In 1887, Abraham Michelson and Edward Morley conducted an experiment aimed at detecting the relative movement of substances relative to luminescent ether. Using what is now called the Michelson interferometer, Michelson and Molly measured the speed of light in two orthogonal directions from a common light source.

The result of this experiment is negative, because it obtains the same speed of light, regardless of the position and motion of the earth around the sun. This posed a major problem in physics, and its solution led to the proposal of the theory of relativity in 1905. Einstein's theory is based on the following two assumptions:

(1) Principle of relativity: the equations describing the laws of physics have the same form in all inertial reference frames;

(2) Invariant light speed: in a vacuum, light propagates at a constant speed c , irrespective of the state of motion of the source.

Although the principle of relativity has been realized in Galileo and Newtonian mechanics, the second hypothesis is a drastic amendment to our understanding of time and space.

A central concept of special relativity is the space-time interval between two events. Let Δt , Δx , Δy and Δz denote the coordinate difference between the two events p and q relative to the global inertial reference system. Then, the space-time interval between these events is

$$\Delta s^2 = -c^2(\Delta t)^2 + (\Delta x)^2 + (\Delta y)^2 + (\Delta z)^2 \quad (2)$$

The form of the interval (2) is quadratic in the differences of the coordinates, and invariant under the Poincaré group (translations, rotations, boosts [20]), thus ensuring that the speed of light is indeed the same in all inertial frames. This observation suggests that, in full analogy with the Euclidean geometry of three-dimensional space, special relativity can be formulated as a theory of the Lorentzian geometry of four-dimensional spacetime.

In addition, the space-time interval can be used to explore the causal structure of space-time. See Figure 1. Given the event p , the light cone \mathcal{C}_p is the set of all events q , such that $\Delta s^2 = 0$. These events are called light related to p , because all these events can be reached by light passing through p . All events in \mathcal{C}_p make $\Delta s^2 < 0$. It is said that these events are time-dependent with p , because the massive particles passing through p can reach any of them at least in principle. The remaining events, that is, events other than \mathcal{C}_p , make $\Delta s^2 > 0$. Those events are

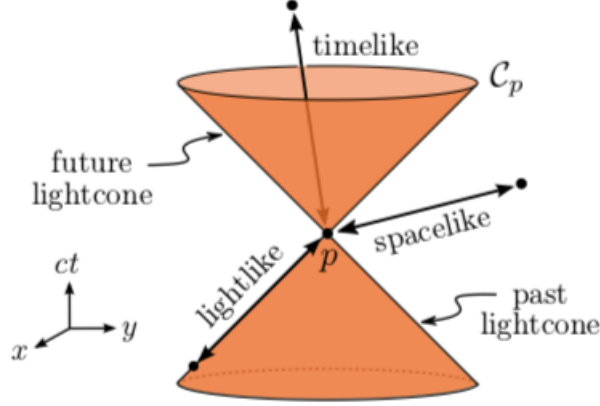


Figure 1: In special relativity, the causal structure of space-time defines a notion of light-cone C_p at any event p . All events on C_p are lightlike related to p , while all events within (respectively, outside) C_p are timelike (respectively, spacelike) related to p . [24]

called p -related spatial events because they cannot be reached without mass particles or any light passing through p . Two events related to space cannot have a causal relationship with each other.

1.1.3 Relativistic gravity

Next, let us explore whether gravitational interaction can adapt to the model of special relativity. For Poisson's equation (1), we extend it to replace the elliptic Laplace operator ∇^2 with the hyperbolic d'Alembert operator, and replace the mass density ρ with the Lorentz covariate source. Therefore, we can get the gravitational field equation as follows:

$$\square\Phi = -\frac{4\pi G}{c^2}T \quad (3)$$

Where $\square = -\frac{1}{c^2}\frac{\partial^2}{\partial t^2} + \nabla^2$ is the usual plane wave operator, and T is Trace of the energy momentum tensor of matter. This scalar gravity theory follows the principle of special relativity and reproduces Poisson's equation (1) in the non-relativistic limit, where $c^{-1} \rightarrow 0$.

This shows that gravitational propagation needs to be combined with a limited speed, just like the form of electromagnetic wave propagation, gravitational waves should also be in the form of traveling waves and propagate at the speed of light. Of course, the generation of gravitational waves is due to the vibration of space. There are many ways to generate gravitational waves. The most common is the merger of binary star systems. Of course, supernova explosions will also generate gravitational waves. This thesis mainly discusses the gravitational waves generated in the merger of binary star systems, especially the gravitational waves generated by the merger of neutron stars.

1.2 Binary star system

Binary neutron stars(BNS) Neutron stars are one of the strangest objects in the universe. The mass of the neutron star is about 1.5 of that of the sun, and the radius is about 10 km. It is the most compact stable structure. The degenerate pressure of the material can still balance gravity. Further compression will cause gravity to collapse and form a black hole. Since gravity is extreme, its rotation is extreme: A neutron star is the fastest known rotating star with a period as short as milliseconds. When a neutron star and a normal star are in a binary star system, its huge gravitational field can capture the material of the companion star accumulated on the neutron star. The huge release of the gravitational force of the accretion material makes the system's luminosity in the X-ray band as high as 100,000 suns. Neutron stars also have very strong surface magnetic fields, ranging from 10^7 Gauss to 10^{15} Gauss. The magnetic field can transfer the magnetic poles to the material near the surface. Under the action of such a high magnetic field of neutron stars, considering that most neutron stars are born with a certain angular

momentum, this periodic magnetic field changes are modulated during rotation. Make the neutron star a pulsar. Because neutron stars have a huge moment of inertia ($10^{45} g/cm^2$), neutron stars have become the most stable clock in the universe and beacons in cosmic navigation.

In the old binary star system, when the magnetic field of the neutron star decays to $10^8 \sim 10^9$ Gauss, the accumulation of matter and angular momentum can accelerate the neutron star to a very fast spin cycle, which can reach several hundred revolutions per second. The maximum rotation speed of a neutron star depends on its compactness, that is, its mass radius ratio. In other words, it depends on the equation of state of the ultra-dense matter in the neutron star. The search for the fastest spinning neutron star may impose important constraints on the equation of state for the densest matter configuration in the universe.

In this research, the main research goal is the neutrino signal that can be received in the binary neutron star merger (BNS), but because it is an automated system, when a gravitational wave signal is detected, we will also proceed accordingly Neutrino detection.

Binary black hole(BBH) A black hole is a place in space where the gravitational pull is so great that even light cannot be emitted. The force of gravity is so great because the matter is squeezed into a small space. This can happen when a star is about to die.

Because there is no light emission, people cannot see black holes. They are invisible. Black holes can only be observed indirectly by observing the shadow of the black hole and the nearby accretion disk. This black hole photo is the first photo of the black hole through the accretion disk around the black hole. Observing a black hole requires a telescope with an aperture equivalent to that of the Earth to effectively observe it. The telescope used for this observation is the Event Horizon Telescope, which can be observed simultaneously by combining radio telescopes around the world. The black hole photo shooting also won the Nobel Prize.

Because of the big mass, we can easier get the signal which from the black hole merger than BNS. But as we know there are nothing can escape from the black hole, also neutrinos. So in our research, the expected of neutrino signals which emitted by BBH is 0.

1.3 Neutrino

Pauli predicted in 1930 that neutrinos would retain the momentum of beta decay. Reines and Cowan conducted experimental observations in 1956. Initially, neutrinos were considered massless. Now, since neutrino oscillations are observed, they have mass. They have 3 flavors corresponding to light protein. Because their quality intrinsic state and flavor intrinsic state are different, the flavor oscillates or changes during driving. In the Standard Model, neutrinos are elementary particles. Since the interaction of gravity is very small, it can be ignored. It is electrically neutral and will not interact with strong forces. Weak nuclear force is the main interaction channel. Neutrinos pass through large objects with little interaction. Its experimental research requires large detectors and advanced technology.

Neutrinos are produced through nuclear reactions, such as the fusion of the sun, the fission of the crust and mantle of the earth, and reactors. When cosmic rays interact with atomic nuclei in the atmosphere, they also produce neutrinos, which produces unstable particles that decay. There are also artificial neutrino beams. The properties of neutrinos have been studied from these various sources. Neutrinos can also be used to study astronomical events. Many astronomical events produce or are expected to produce large numbers of neutrinos. Due to the low interaction rate of neutrinos, it can bring different information to the earth without scattering or shielding. The only astronomical neutrinos observed so far are from the sun and supernova 1987A. This thesis is to detect the neutrinos produced during the merger of celestial bodies when gravitational waves are generated, especially the neutrinos produced during the merger of neutron stars. According to different theoretical predictions and equation of state, the energy of neutrinos produced during the merger of neutron stars will be different to a certain extent (the figure [Figure 2](#) shows the prediction of neutrino production with different energies according to different equation of state). If the generated neutrinos can be detected The energy of neutrinos helps us to speculate on the reactions that take place during the merger of neutron stars, and provides the corresponding data basis for the merger of neutron stars.

EoS	Time(ms)	$\langle E_{\bar{\nu}_e} \rangle$ MeV	$\langle E_{\nu_e} \rangle$ MeV
DD2	3.0	18.3	14.6
DD2	7.9	13.2	10.2
NL3	2.5	18.5	15.2
NL3	8.4	13.4	9.8
SFHo	3.2	24.6	23.5

Figure 2: Observed at infinity neutrino average energies for electron neutrinos and electron antineutrinos for three different EoS[14]

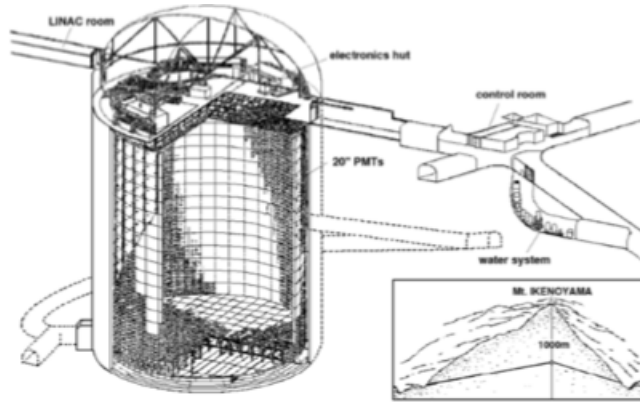


Figure 3: Super-Kamiokande Detector

2 Super-Kamiokande(SK)

2.1 Detector Overview

Super-Kamiokande (SK) is a 50kilo-ton Cherenkov water detector located in the Kamioka mining area. The cosmic ray muon reduced the 1,000m rock shield (2700 m.w.e.). The detector is cylindrical with a diameter of 39.3 m and a height of 41.4 m. The stainless steel frame structure divides the detector into two parts, the inner detector (ID) and the outer detector (OD). The structure forms an optical barrier and supports the photo-multiplier tube (PMT). In the OD, there are 1885 8-inch PMTs that monitor particles entering from the outside, and 2.5 m of water shields gamma rays from the rocks surrounding the detector.

The inner side of the frame structure is surrounded by a polyethylene terephthalate black sheet to reduce optical reflection. The ID is formed by 11,129 20-inch PMT, providing a photo coverage of $\sim 40\%$. The volume within 2 m from the ID wall is not used for SK analysis. The remaining volume of 22.5 tons is called the fiducial volume (FV). The space above the detector is a research dome with 4 electronic huts and a central control room.

2.2 SK history

SK's predecessor, the Kamioka Nuclear Decay Experiment (KamiokaNDE) detector, has a water tank with a diameter of 15.6 m and a height of 16 m. It contains about 3 tons of pure water and 948 tons of PMT, 123 tons of PMT in the OD. Observations were made from July 1983 to April 1996, during which time the neutrinos of the supernova (SN1987A) were observed. As the successor to the KamiokaNDE experiment, the construction of the SK detector began in 1991. For SK storage tanks, holes in the mine were dug until mid-1994. Thereafter, the construction of the water tank began and the PMT was installed until the end of 1995. Water injection started in

January 1996. The experimental data was collected after a month of test operation, starting from April 1, 1996. From the beginning of operation to the present, SK is divided into six stages (ie SK-I, SK-II, SK-III, SK-IV, SK-V and SK-Gd (SK-VI)).

1. SK-I started observation on April, 1996. This period ended on July, 2001.

2. After regular maintenance in July, 2001, a shock wave from the implosion of a PMT caused the chain implosion of almost half of the PMTs. Then, the remaining PMTs were re-distributed and SK-II started on October, 2002. From SK-II, PMTs are protected from shock waves by acrylic covers and fiberglass reinforced plastic (FRP). SK-II was stopped to mount new PMTs on October, 2005.

3. The data cycle from July 2006 to August 2008 is SK-III. In October 2005, SK re-installed the PMT and completed it in July 2006. SK-III has 11129 ID PMTs, and the coverage rate of photos is 40%.

4. Since September 2008, as all front-end electronics have been upgraded, the detector has been shut down. Then continue with SK-IV from September 2008 to June 2018. During this period, the T2K experiment using SK as a far detector was started, and the first event of the T2K experiment was successfully observed in SK on February 24, 2010.

5. In preparation for the SK-Gd phase, SK repaired the leak of the water tank, installed new pipes, replaced the failed ID and OD PMT, and cleaned the water tank. This stage is SK-V, which starts in January 2019 and ends in July 2020.

6. The SK-Gd phase has started in July 2020, which dissolve gadolinium in ultra-pure water at SK. Gadolinium has the largest cross-section of thermal neutron capture among natural elements, and a total of about 8 MeV gamma rays are emitted. Therefore, it is possible to distinguish between neutrino reactions with neutrons and those without.

2.3 Detector Principle

SK detects Cherenkov light, which is emitted when charged particles travel faster than the speed of light in the medium. Cherenkov light radiates in a cone shape along the path of charged particles. The angle between the direction of the charged particle and the direction of Cherenkov light is called Cherenkov angle θ_c , which can be calculated by the following formula

$$\cos \theta_c = \frac{1}{\beta n(\lambda)} \quad (4)$$

Where β is the speed of the charged particle relative to the speed of light in vacuum, and $n(\lambda)$ is the refractive index at the wavelength λ . In pure water, the refractive index at 589 nm is 1.33. For relativistic particles like electrons and positrons, θ_c is 42° also a muon with 1 GeV. The energy threshold of Cherenkov light emitted is determined by the following formula:

$$E_{thr} = \frac{m}{\sqrt{1 - (1/n)^2}} \quad (5)$$

where m is the rest mass of the charged particle. The number of Cherenkov photons along the trajectory per wavelength is calculated by

$$\frac{d^2 N}{d\lambda dx} = \frac{2\pi z^2 \alpha}{\lambda^2} \left(1 - \frac{1}{\beta^2 n^2(\lambda)}\right) = \frac{2\pi z^2 \alpha}{\lambda} \sin^2 \theta_c \quad (6)$$

where z is the particle charge in units of e and α is the fine structure constant.

2.4 Photomultiplier Tubes

The 20-inch PMT (R3600) [29] for the ID was developed by Hamamatsu Photonics. The schematic is shown in Figure 4.

Its photocathode is made of baikkali (Sb-K-Cs) and is sensitive to photons with wavelengths of 300 to 600 nanometers. Its quantum efficiency is about 20% at the maximum (Figure 5). Photoelectrons (pe) generated by the photoelectric effect are amplified $10^6 \sim 10^7$ by the dynode chain. The PMT dark noise is 4 kHz. The Helmholtz coil around the detector reduces the geomagnetic field that affects the PMT response from 450 mG to 50 mG.

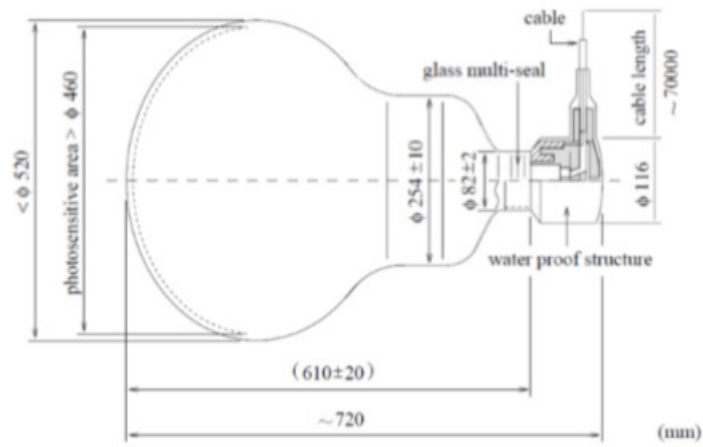


Figure 4: A schematic of the Hamamatsu R3500 PMT.[19]

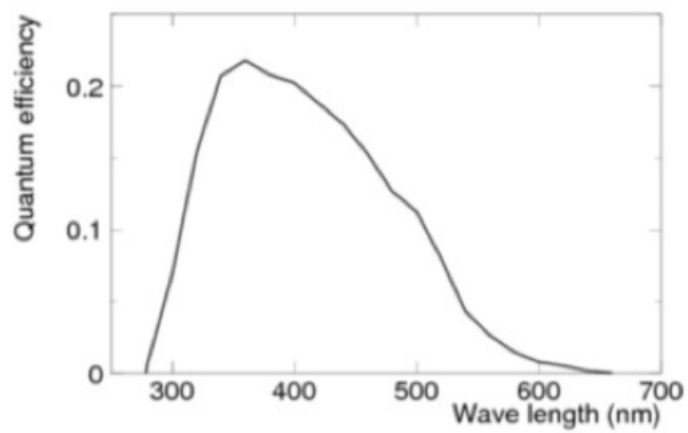


Figure 5: The quantum efficiency of the Hamamatsu R3600 as a function of wavelength.[19]

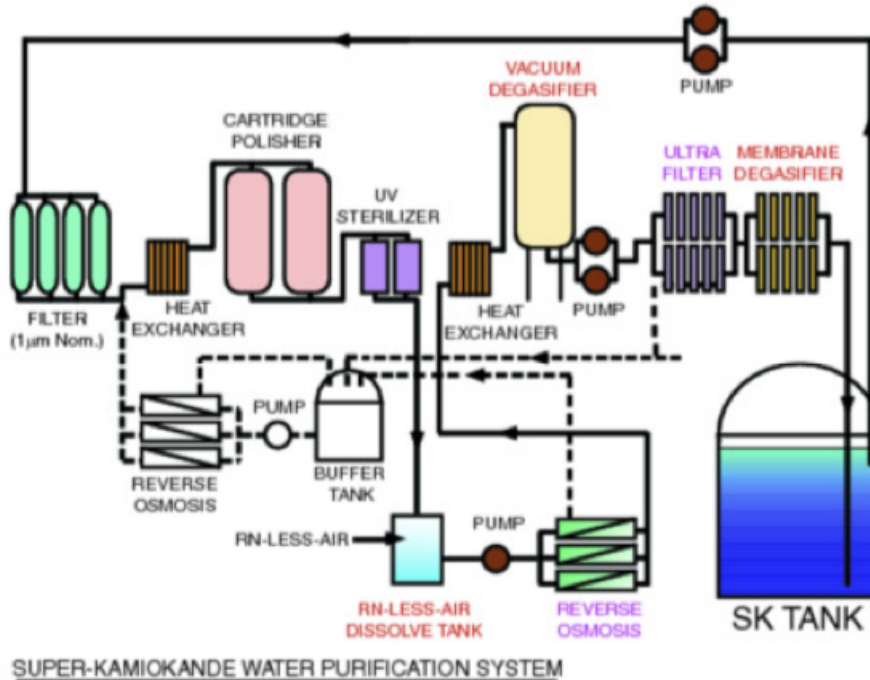


Figure 6: The SK water purification system.[19]

2.5 Water Systems

The water purification system (Figure 6) was developed to maintain the quality of water transparency and radioactivity. The higher transparency gives less attenuation of the Cherenkov light. Radioactivity can produce backgrounds in the low energy analysis.

The water system consists of the following components:

- $1\mu m$ filter: Removes large particles.
- Heat exchanger: Maintains the water temperature at $13^{\circ}C$. Water temperature variations cause convection, while higher temperatures increase PMT dark noise and the growth of bacteria.
- Cartridge polisher: Removes heavy ions.
- UV sterilizer: Kills bacteria.
- Vacuum de-gasifier: Removes oxygen and radon in water.
- Ultra filter: Removes particles larger than 10 nm .
- Membrane de-gasifier: Removes dissolved gas.
- Reverse osmosis: Removes large particles with molecular weight > 100 .

The water circulates at a rate of 60 tons per hour. It fills from the bottom of the detector and drains from the top (Figure 7).

The water temperature is monitored in the ID and OD. It is uniform from the bottom to 11m below the center and slightly increases with height (Figure 8). The difference between top and bottom is $0.2^{\circ}C$.

2.6 Radon Free Air Systems

The air in the mine includes radon in the surrounding rocks. Radon will affect the low energy background rate. SK's system can draw in air from outside the mine and reduce radon in the air. The schematic diagram of the air system without the radon is shown in Figure 9. It consists of the following components:

- Compressor: Provides air pressure up to 7-8.5 atm.
- Air filter: Removes dust in the air. The air goes through 3 types of filters, $0.3\mu m$, $0.1\mu m$, and $0.01\mu m$, from large to small.
- Air drier: Removes water and CO_2 in the air.
- Carbon column: Absorbs the radon in the air. 8 m^3 of charcoal is used in total.

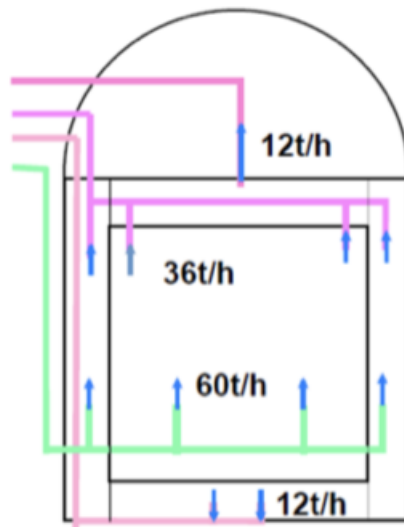


Figure 7: The SK water flow.[28]

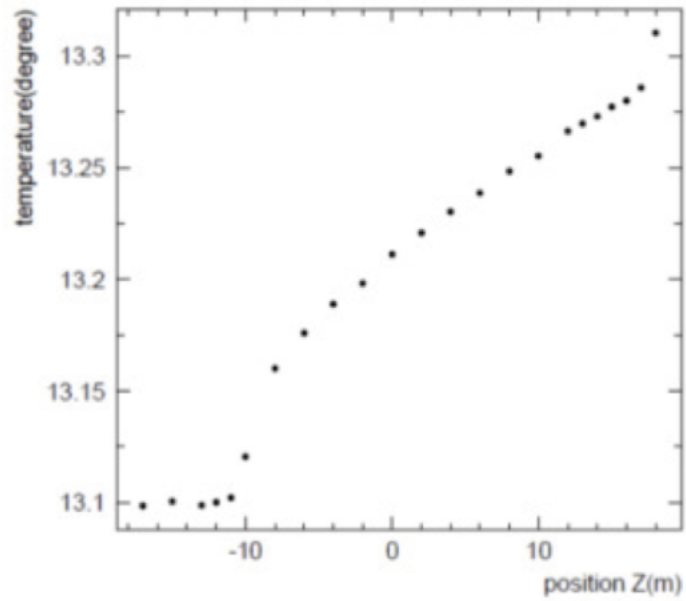


Figure 8: The z-dependence of the water temperature.[28]

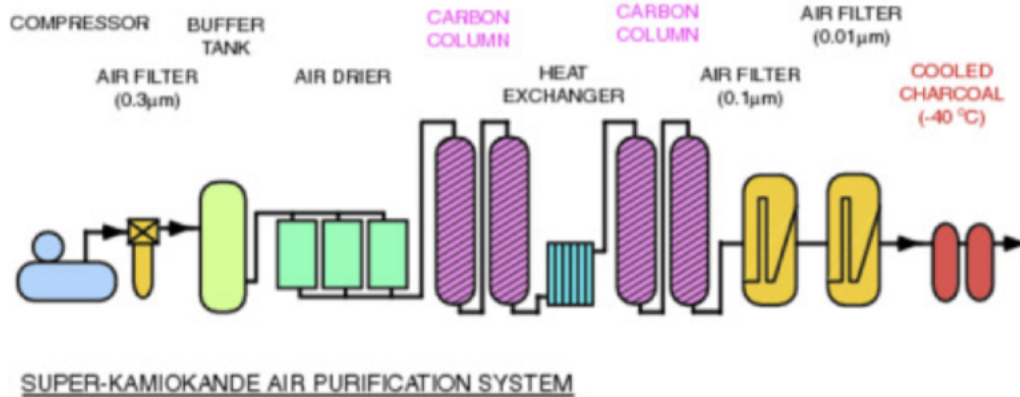


Figure 9: The radon free air system.[19]

- Cooled charcoal: Has better radon removal efficiency. The volume is 50 L.

The radon level increases to $\sim 2000 \text{ Bq/m}^3$ in summer and decreases to $\sim 260 \text{ Bq/m}^3$ in winter. The air system without radon is maintained in the experimental area $\sim 40 \text{ Bq/m}^3$. In order to prevent the air with radon in the mine from entering the tank, SK will make the pressure of the radon free air in the tank higher than the outside pressure (0.3 kPa)

2.7 Front-end Electronics and Data Acquisition System

The front-end electronics and data acquisition system (DAQ) was upgraded in August 2008. This upgrade can achieve more stable data collection and greater data throughput.

Each PMT hit is recorded without loss and selected by a trigger. Because SK has multiple physical purposes, multiple types of triggers are installed. Low energy (LE) trigger, high energy (HE) trigger and super high energy (SHE) trigger have a timing window of $40 \mu\text{s}$. Before the trigger, $5 \mu\text{s}$ is stored for pre-event γ research, and the subsequent $35 \mu\text{s}$ is used for post-event research. At the beginning of a new DAQ period, the trigger threshold is 47, 50, and 70 hits in 200 nsec for LE, HE, and SHE, respectively. The SHE threshold was changed to 58 hits in the summer of 2011.

Figure 10 shows the schematic of the DAQ system. The signals from PMTs go to the new front-end electronics, QTC (charge-to-time converter) Based Electronics with Ethernet (QBEE, Figure 11). The QBEE has a 24 analog input channel with a dynamic range of 0.2 to 2500 pC. It works 5-times faster than the previous electronics[28]. 8 QTC chips mounted in the QBEE integrate the input charge and output a pulse of proportional width. The pulse width and timing is digitized by a time-to-digital converter (TDC). The digital information is processed by a Field Programmable Gate Array (FPGA)[27].

TCP(Transmission Control Protocol) which is one of the main protocols of the Internet protocol suite packets from 500 QBEE are sent to 20 front-end PCs. The front-end PC will sort the data in time, and then send the data to 10 combined PCs. The merged PC also sorts the data by time, and then applies the event construction process to the data in the same time zone. During the event building process, the trigger will scan data from 20 front-end PCs. The triggered event will be sent to the organizer's PC and recorded on the disk. Gigabit Ethernet is used for data transmission between PCs.

2.8 Monitoring system

The status of data acquisition is monitored by various tools. The "Slow Control" monitor checks the high voltage status and the temperature of the electronic equipment. The data flow, PMT conditions and trigger rate are monitored by the distributed process. It also monitors data transfer and offline processes. The online program displays visual images of events in real time. This display helps to monitor DAQ system and PMT.

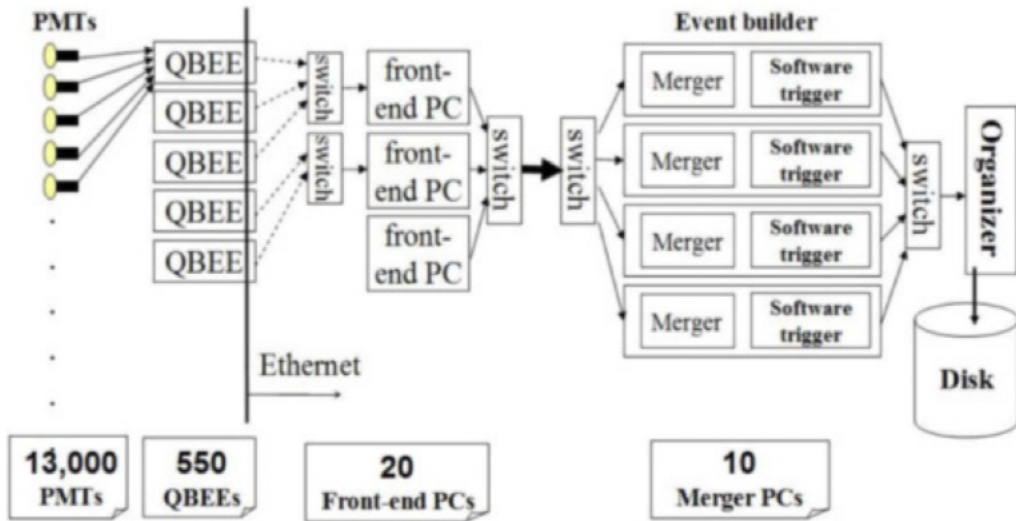


Figure 10: The schematic of the DAQ system.[32]

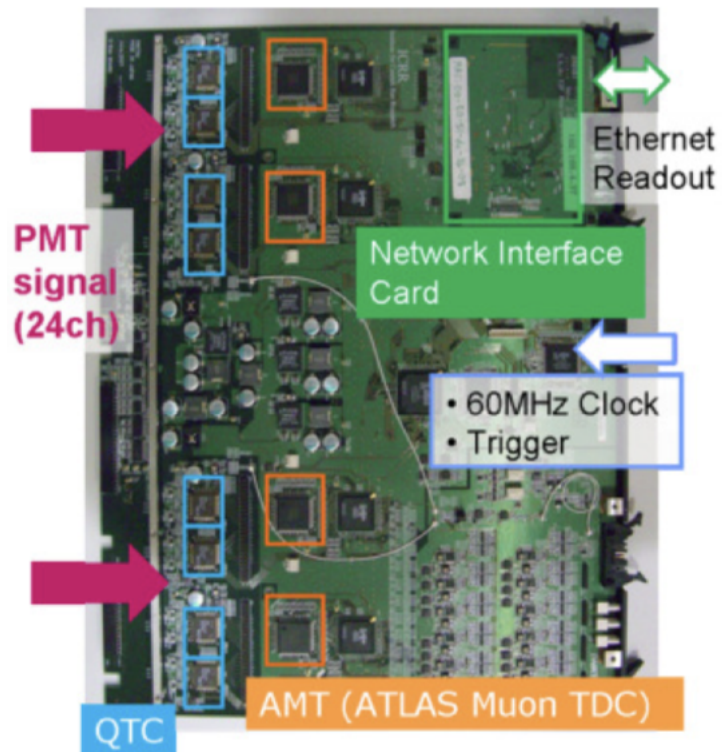


Figure 11: QBEE.[28]



Figure 12: LIGO Livingston

3 LIGO/VIRGO Detector

3.1 Introduction

LIGO is the abbreviation of Laser Interferometer Gravity Wave Observatory. It is currently the most sensitive and largest gravitational wave detector in operation in the world. LIGO first observed gravitational waves in 2015 and won the Nobel Prize for it. LIGO has two observation points, which are located in Hanford, Washington, and Livingston, Louisiana, USA, which are 3000km apart. Simultaneous observation of the two observation points can greatly reduce the possibility of misjudgment of gravitational waves, and pass The time difference between the arrival of the gravitational wave signal and the distance between the two can roughly determine the source and direction of the signal. LIGO mainly uses the Michelson Observer to observe the gravitational wave. The observation principle will be described in the next section.

LIGO has super large interference arms (each interference arm has 4km), which can improve the accuracy of observation. Since the observation of gravitational waves is different from other astronomical observations, and there is no electromagnetic interference in traditional observations, the components of LIGO's detectors are completely isolated. The detector consists of 1.2m wide steel vacuum tubes arranged in an L-shape and covered by a concrete bunker 10 feet wide and 12 feet high.

3.2 Detector Principle

The LIGO detector is designed to detect the differential strain of the incident GW based on a simple Michelson interferometer (see Figure 12). This design starts from the input laser incident on the beam splitter located at the origin, and its face forms an angle of 45 degrees between the x-axis and the y-axis. The beam splitter directs 50% of the light in two vertical directions x and y. The light travels to the mirrors located at the end of the arm $(L_x, 0)$ and $(0, L_y)$, which redirect the light back to the beam splitter. The cumulative phase of the light from the beam splitter to the end mirror is given by:

$$\Phi = \int_0^L \frac{2\pi}{\lambda} dx = \frac{2\pi L}{\lambda} \quad (7)$$

Where L is the distance traveled and λ is the wavelength of light. The total phase of such a round trip will be the sum of the integral drop and the integral return. When the light returns to the beam splitter, the two beams interfere with each other under such conditions. In this way, depending on the length of the differential arm, the light will either return to the laser (symmetric port), or toward the photodetector (antisymmetric port), or a

combination of both. Then, by looking at the power of the light from the antisymmetric port P_{AS} , the differential arm length $L_x - L_y$ can be measured in a way that the mode is a wavelength. This is caused by

$$P_{AS} = P_0 \sin^2(\phi_x - \phi_y) = P_0 \sin^2\left(\frac{4\pi}{\lambda}(L_x - L_y)\right) \quad (8)$$

Where P_0 is the input laser power, ϕ_x is the cumulative phase of the beam in the x arm, and ϕ_y is the cumulative phase of the beam in the y arm. This shows that P_{AS} depends on the length of the differential arm. Let us assume that the length of the arm is the same L and the amplitude of the incident GW is h . It stretches the detector along the x-axis and squeezes it along the y-axis. This effect causes The distance the light needs to travel is given by $L' \approx L(1 \pm h/2)$, and ϕ_x and ϕ_y are

$$\begin{aligned} \phi_x &= \int_0^{L'} \frac{2\pi}{\lambda} dx - \int_{L'}^0 \frac{2\pi}{\lambda} dx \\ &\approx \frac{4\pi L}{\lambda} \left(1 + \frac{h}{2}\right) \end{aligned} \quad (9)$$

$$\phi_y \approx \frac{4\pi L}{\lambda} \left(1 - \frac{h}{2}\right) \quad (10)$$

With these phase shifts, we find that P_{AS} is then given by

$$P_{AS} = P_0 \sin\left(4\pi \frac{hL}{\lambda}\right)^2 \quad (11)$$

Thus, for the same change of P_{AS} , the strain h is inversely proportional to the length L of the arm. However, although the antisymmetric port of this interferometer has a signal, it is a The method of detecting GW is poor. First, since the above power on the asymmetric port is proportional to $\sin^2(\Delta\phi)$, Taylor can be expanded to approximately $\Delta\phi^2$ about zero, so the signal we are measuring It is square and proportional to the small GW signal we want to sense. In addition, there is no information that we need to move the mirror to bring the signal back to the dark fringe.

In order to solve these problems, LIGO adopted the "heterodyne detection" technology, which combines the phase modulation input laser with Schnupp asymmetric technology. In this setting, before the laser enters the interferometer, the light is phase-modulated at the frequency Ω . In this way, instead of the three superimposed laser beams incident at three frequencies, they all enter the detection at one frequency. The electric field amplitude: the original beam with frequency ω and amplitude E_0 , also called carrier, and two sidebands with frequency $\omega \pm \Omega$ and amplitude E_1 .

When the arm lengths are exactly equal, all these beams will exit at the symmetrical port, which will produce the same answer as above. However, there will be a different response when Schnupp asymmetry is introduced between the two arms. This happens when the unequal amount of the arm of the interferometer is an integer multiple of the wavelength of the carrier, rather than an integer multiple of the wavelength of the sideband. In this case, in the absence of a GW signal, the carrier light will be emitted from the symmetric port, and the sideband will be transmitted to the antisymmetric port. When a GW signal is present, a phase shift will be introduced on all three beams so that a mixture of all three beams will exit the antisymmetric port. Performing demodulation processing on the signal from the asymmetric port as needed will cause the error signal to be linear in the GW amplitude.

In order to improve the sensitivity of the detector, LIGO modified the standard Michelson interferometer twice. The first is to use Fabry-Perot cavities in the two arms to increase the storage time of light in the arms, effectively increasing the length of the arms, thereby increasing the phase shift of the light by the same factor. The second is to increase the power recovery mirror to enhance the light circulating in the interferometer under a given laser input power. The design schematic diagram of LIGO, including all the additional functions of the standard Michelson interferometer, is shown in [Figure 13](#).

3.3 History

Till now, there are three phases in LIGO history called O1,O2,O3.

O1 It started on September 18, 2015 and ended on January 12, 2016. The data from the surrounding engineering period is of sufficient quality to be included in the analysis, which means that the observation data was collected from September 12, 2015 to January 19, 2016. The operation involves Hanford (H) and Livingston (L) detectors.

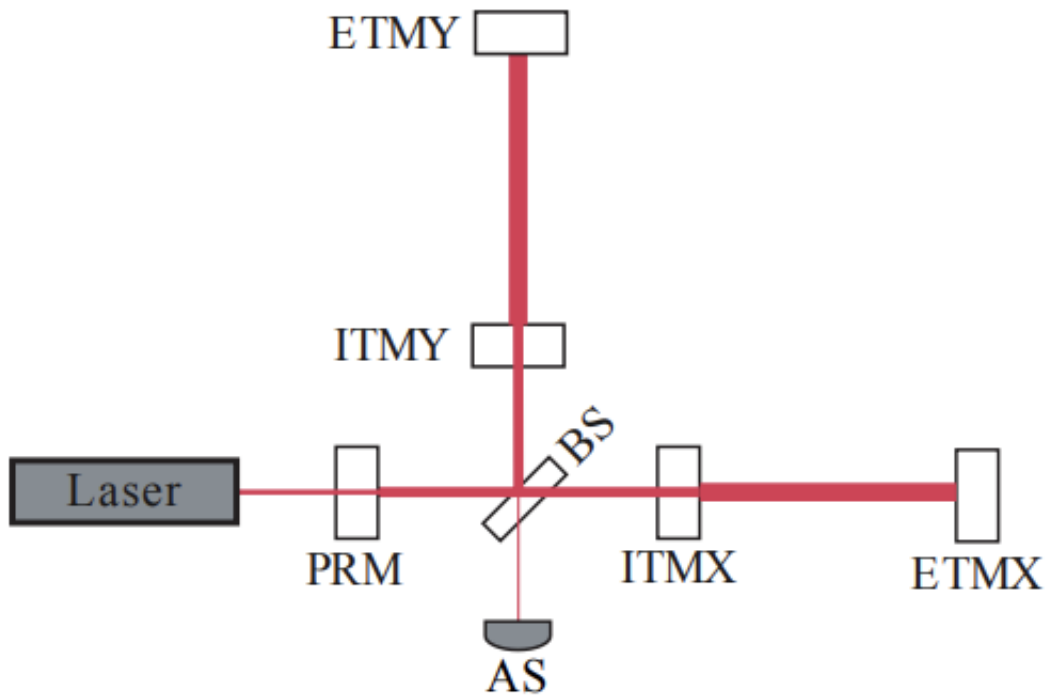


Figure 13: A simple schematic of the LIGO detectors. The mirror labels are as follows: PRM (power recycling mirror), BS (beam splitter), ITMX/Y (x-/y- arm input test mass), ETMX/Y (x-/y- arm end testmass), AS (antisymmetric port). The width of the laser beam denotes power in different portions of the detector. A simple Michelson interferometer includes the mirrors BS and ETMX/Y. The addition of the ITMX/Y mirrors makes use of Fabry-Perot cavities for the arms. The use of the PRM boosts the power circulating in the whole interferometer

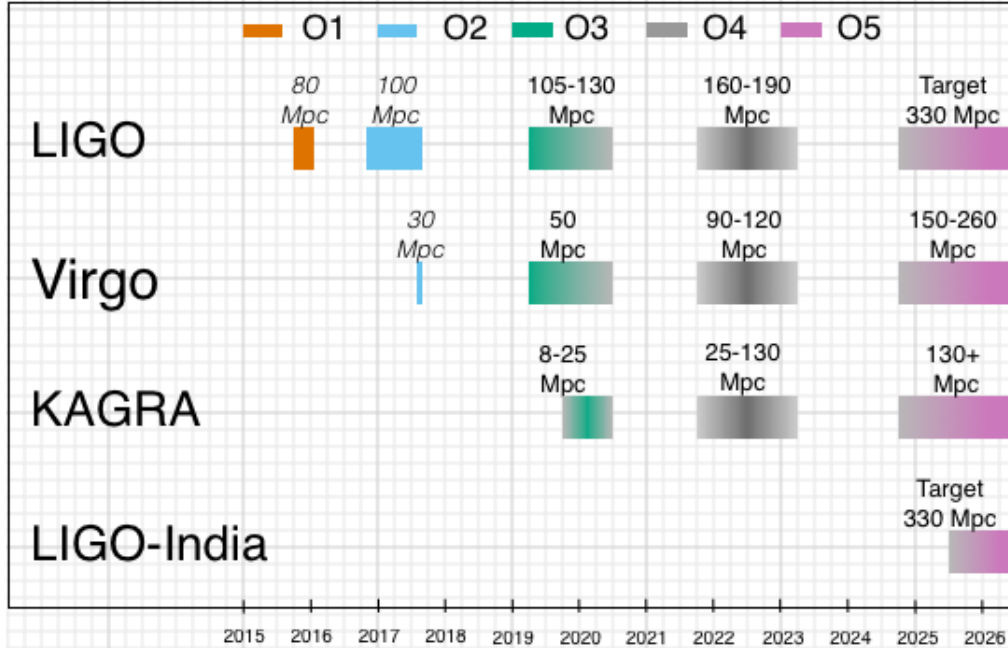


Figure 14: LIGO phases

O2 The project started on November 30, 2016 and will end on August 25, 2017. Prior to this, the project began on October 31, 2016 in Livingston and on November 14, 2016 in Hanford. Hanford’s delay was to facilitate additional commissioning activities. The sensitivity achieved during the whole operation is usually in the BNS range of 80-100 Mpc. AdV interferometer joined O2 on August 1, 2017, forming a network of three detectors in the last month of operation. The target is a BNS range of 40 Mpc. Since the vacuum contamination problem has been solved, AdV uses steel wire instead of fused silica fiber to suspend the test substance. This limits the maximum BNS range of AdV; in O2, the BNS range reaches 30 Mpc.

O3 The third observing run started on April 1, 2019 and was expected to end on April 30, 2020, with a commissioning break from October 1, 2019 to November 1, 2019. While this article was in review the COVID-19 Pandemic led to suspension of the observing run on March 27, 2020. The increase in sensitivity of the LIGO detectors (whose target sensitivity was expected to be 120 Mpc) comes from a variety of changes, chiefly from increasing the input laser power, adding a squeezed vacuum source at the interferometer output and mitigating noise arising from scattered light. Additionally, end test-mass optics with lower-loss coatings, along with new reaction masses, have been installed in each interferometer. The Livingston instrument began the run with an average BNS range of 130 Mpc and the Hanford instrument typically operates with an average range of 110 Mpc. Fused silica fibers were installed on the AdV test mass suspensions in preparation for O3. Other improvements included reduction of technical noises, increasing the input laser power and installation of a squeezed vacuum source. The result was a BNS range of 50 Mpc at the start of O3.

3.4 Signal Display

In the gravitational waves detection, the most important indicator is frequency. By using Numerical Relativity, we can define a Chirp-Mass[12] as $\mathcal{M} = M\eta^{3/5}$ which $\eta = \frac{\mu}{M}$, $\mu = \frac{m_1 m_2}{M}$, $M = m_1 + m_2$. And we can also compute this chirp-Mass from frequency like

$$\mathcal{M} = \frac{c^3}{G} \left[\frac{5}{96} \pi^{-8/3} f^{-11/3} \dot{f} \right]^{3/5} \quad (12)$$

where f and \dot{f} are the observed frequency and its time derivative and G and c are the gravitational constant and speed of light. By using this equation, the chirp-Mass can be computed by frequency. For GW150914, LIGO estimates f and \dot{f} based on the data in Figure 16[4]. We get the chi mass of $\mathcal{M} \simeq 30M_\odot$, which shows that the total mass $M = m_1 + m_2$ in the detector frame is $> 70M_\odot$. This limits the sum of the Schwarzschild radii of the

binary components to $2GM/c^2 > 210\text{km}$. In order to reach the 75 Hz orbital frequency (half the frequency of the gravity wave), objects must be very close and very compact; orbits equal to the mass of the Newtonian point are only 350 km apart at this frequency. Although a pair of neutron stars is compact but will not have the required mass, a black hole neutron star binary with inferential chi mass will have a very large total mass and therefore will merge at a much lower frequency. This leaves a black hole because the only known object is compact enough to reach an orbital frequency of 75 Hz without contact.

Next, we can use the max amplitude to get the distance of the source by

$$h_{max} = \frac{4G^2 M\mu}{c^4 Dr} = \frac{4(G\mathcal{M})^{5/3}(\pi f)^{2/3}}{c^4 D} \quad (13)$$

Where D is the distance , f is frequency, G is gravitational constant, \mathcal{M} is chirp-Mass. For the emitted energy, we can compute by the wave function that

$$\frac{dE}{dt} = \frac{2c^3}{15G} \left(\frac{dA}{du}\right)^2, h = A(u) \sin^2 \theta / r \quad (14)$$

And we can also compute merger time by using those parameters like

$$t_0 = \frac{5}{256(Gc^{-3}\mathcal{M}^{5/3}(\pi f_0)^{8/3})} \quad (15)$$

From [Figure 15](#) ,comparing the t_0 of each signal ,So we can easily distinguish Binary Neutron Star or Black Hole Merger.

For each GW event , we get information from frequency and merger times and we can compute distances , mass,and so on.

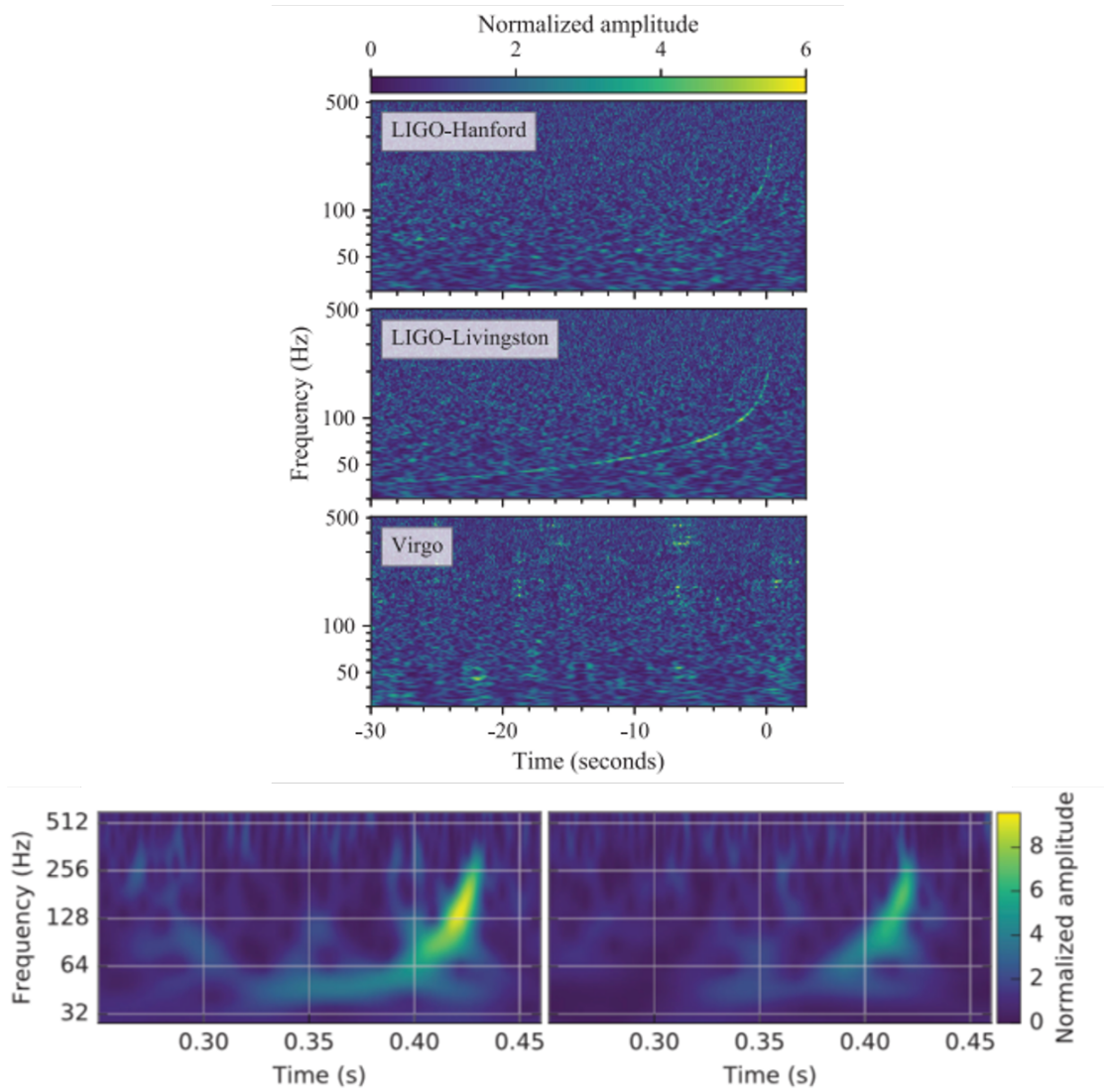


Figure 15: merger time for Binary Neutron star(up) and Black hole Merger(down)

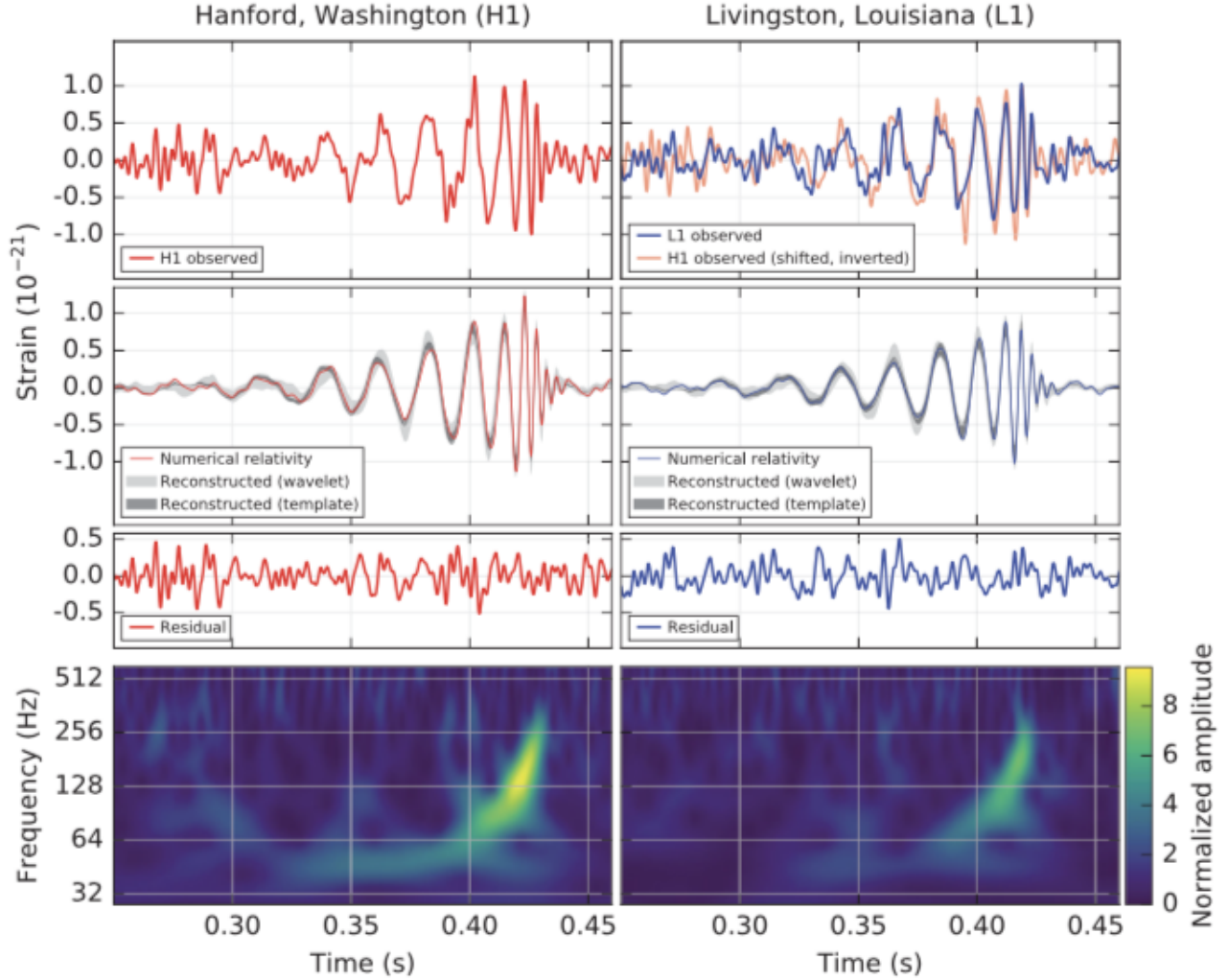


Figure 16: The gravitational-wave event GW150914 observed by the LIGO Hanford (H1, left column panels) and Livingston (L1, right column panels) detectors. Times are shown relative to September 14, 2015 at 09:50:45 UTC. For visualization, all time series are filtered with a 35–350 Hz bandpass filter to suppress large fluctuations outside the detectors’ most sensitive frequency band, and band-reject filters to remove the strong instrumental spectral lines seen in the Fig. 15 spectra. Top row, left: H1 strain. Top row, right: L1 strain. GW150914 arrived first at L1 and $6.9^{+0.5}_{-0.4}$ ms later at H1; for a visual comparison, the H1 data are also shown, shifted in time by this amount and inverted (to account for the detectors’ relative orientations). Second row: Gravitational-wave strain projected onto each detector in the 35–350 Hz band. Solid lines show a numerical relativity waveform for a system with parameters consistent with those recovered from GW150914 [26][17] confirmed to 99.9% by an independent calculation based on [15]. Shaded areas show 90% credible regions for two independent waveform reconstructions. One (dark gray) models the signal using binary black hole template waveforms [6]. The other (light gray) does not use an astrophysical model, but instead calculates the strain signal as a linear combination of sine-Gaussian wavelets [17][5]. These reconstructions have a 94% overlap, as shown in [6]. Third row: Residuals after subtracting the filtered numerical relativity waveform from the filtered detector time series. Bottom row: A time-frequency representation [16] of the strain data, showing the signal frequency increasing over time. [3]

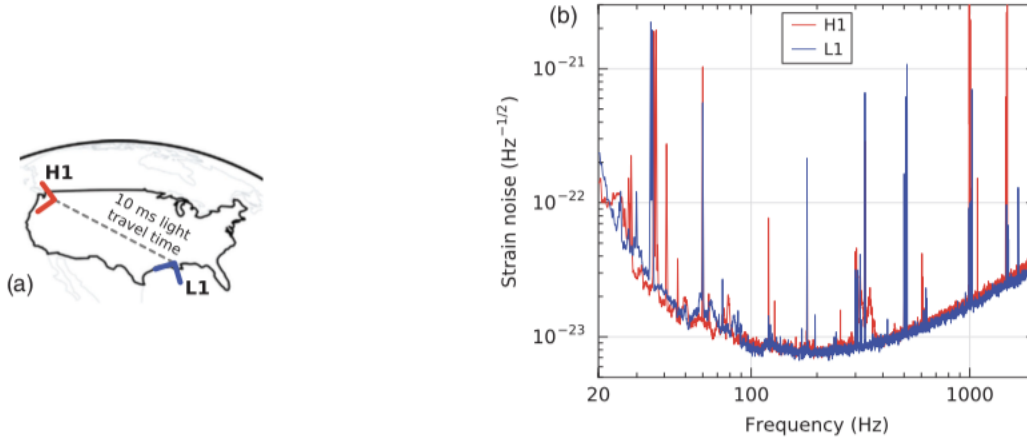


Figure 17: (a): Location and orientation of the LIGO detectors at Hanford, WA (H1) and Livingston, LA (L1). (b): The instrument noise for each detector near the time of the signal detection; this is an amplitude spectral density, expressed in terms of equivalent gravitational-wave strain amplitude. The sensitivity is limited by photon shot noise at frequencies above 150 Hz, and by a superposition of other noise sources at lower frequencies[3]. Narrow-band features include calibration lines (33–38, 330, and 1080 Hz), vibrational modes of suspension fibers (500 Hz and harmonics), and 60 Hz electric power grid harmonics.[3]

4 Automatic system and methods

4.1 Alert receiver and alert database

4.1.1 GCN Notice

Alerts of the gravitational wave detection by LIGO and Virgo are public since the beginning of their third operation period, so-called O3. They are distributed to the follow-up observers of these events via the Gamma-ray Coordinates Network (GCN). GCN has been originally developed by NASA for quick distribution of gamma-ray burst alerts from satellite experiments to the follow-up telescopes on the ground, and now it extends its activity into many types of astronomical transient events, high-energy neutrino events and supernova neutrino events, as well as GW events. The information and results of the follow-up observations are shared with the registered individuals and institutes via GCN also. The former function, alert distribution, is called as *Notice*, and the later one is called as *Circular*.

GCN Notice messages are distributed via a packet connection between a GCN server in NASA and a client machine of a follow-up observer. Several protocols, 160 bytes binary and XML text, are available for Notice, and the format is well defined for each type of the alerts. The messages of GCN Circulars are distributed via E-mail, and they are human-readable descriptions about follow-up results. All Notice and Circular messages are archived in the official web page of GCN.

4.1.2 GCN Notice receiver

A receiver of GCN Notice is implemented by using the python library, `gcn`. The library provides functions for initialization of a packet connection to the NASA server and listening of notices, and they enable us to implement a GW alert receiver by a very simple code. A GW notice message is received as the VOEvent format written in XML, and we can extract several information from the message such as event ID, trigger time, classification of the event, a type of the alert, and links to a web page and a fit file of the event in GraceDB (describe later). These extracted information of the event is filled out into a data base written with a CSV format, and the original VOEvent message (Figure 18) is also saved into a single file.

As an example of the notice, Fig. 18 shows the parameters of a first GW event in O3, which is published on April 8, 2019. Each event is given an unique identification number, such as "S190408an" (see the parameter, TRIGGER_NUM). Usually more than one notice are published for a single GW event based on a LIGO/Virgo alert sequence. The first notice is called as *Preliminary*. It is sent fully automatically within some minutes from the GW event. The others are *Initial* and *Update*. They include additions or updates of the information of the event considering results of other analysis pipelines, and they are published in a few hour and a few days for *Initial* and *Update*, respectively. The type is found in the NOTICE_TYPE row in Fig. 18. Figure 19 describe the alert time line

of LIGO/VIRGO. Sometimes, they find that the event already published by a *Preliminary* notice is background. In this case, *Retraction* notice is sent in order to inform it to the follow-up observers. In case we receive a *Retraction* notice, we remove the event from our database. A GW notice also includes the information of GW event type, such as BBH, BNS and NSBH (neutron star black hole merger), which is provided as event probability of each type (see PROB_XXX). The most important parameter for our analysis is the time of the event, given in TRIGGER_TIME. Another important parameter, especially for the High Energy analysis, is the location of the event in the sky. This is not provided as a simple parameter but a probability-density map of the event location on the sky. It can be addressed via a Fits-formatted file downloaded from the link provided in the notice, SKYMAP_FITS_URL. As an example, the probability density distribution of the GW event S190408an is shown in Fig. 20. A header of the fits file contains some additional information of the event such as the estimated distance between the GW object and the earth, as well as the basic information of the sky map, e.g. the pixel size.

The all public information of the GW candidate events is achieved into a dedicated database for GW, Gravitational-Wave Candidate Event Database (GraceDB [25]). In the web page, all Notice messages, sky map, and reports of follow-up observations for each event are available. If a notice is missed due to a maintenance of the software, the SK server and etc., we can download the notice message from the GraceDB web page (or the NASA GCN web page). An automatic script to do it have already been prepared.

```

TITLE:      GCN/LVC NOTICE
NOTICE_DATE: Mon 08 Apr 19 18:52:34 UT
NOTICE_TYPE: LVC Preliminary
TRIGGER_NUM: S190408an
TRIGGER_DATE: 18581 TJD; 98 DOY; 2019/04/08 (yyyy/mm/dd)
TRIGGER_TIME: 65882.288180 SOD {18:18:02.288180} UT
SEQUENCE_NUM: 1
GROUP_TYPE: 1 = CBC
SEARCH_TYPE: 1 = AllSky
PIPELINE_TYPE: 4 = GSTLAL
FAR:        2.811e-18 [Hz] (one per 4117051101094.8 days) (one per 11279592057.79 years)
PROB_NS:    0.00 [range is 0.0-1.0]
PROB_REMNANT: 0.12 [range is 0.0-1.0]
PROB_BNS:   0.00 [range is 0.0-1.0]
PROB_NSBH:  0.00 [range is 0.0-1.0]
PROB_BBH:   1.00 [range is 0.0-1.0]
PROB_MassGap: 0.00 [range is 0.0-1.0]
PROB_TERRES: 0.00 [range is 0.0-1.0]
TRIGGER_ID: 0x10
MISC:       0x1898407
SKYMAP_FITS_URL: https://gracedb.ligo.org/api/superevents/S190408an/files/bayestar.fits.gz
EVENTPAGE_URL: https://gracedb.ligo.org/superevents/S190408an/view/
COMMENTS:   LVC Preliminary Trigger Alert.
COMMENTS:   This event is an OpenAlert.
COMMENTS:   LIGO-Hanford Observatory contributed to this candidate event.
COMMENTS:   LIGO-Livingston Observatory contributed to this candidate event.
COMMENTS:   VIRGO Observatory contributed to this candidate event.

```

Figure 18: The message of GCN Notice for the GW event, S190408an [11]. This was a first notice for the event in O3, and the information was updated by the second notice labelled as *Initial*, which was published 1.5 hour later than the first notice.

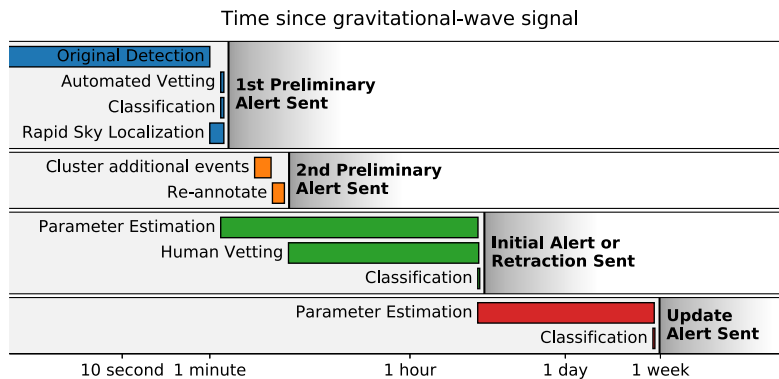


Figure 19: The types of GW alerts and related timelines

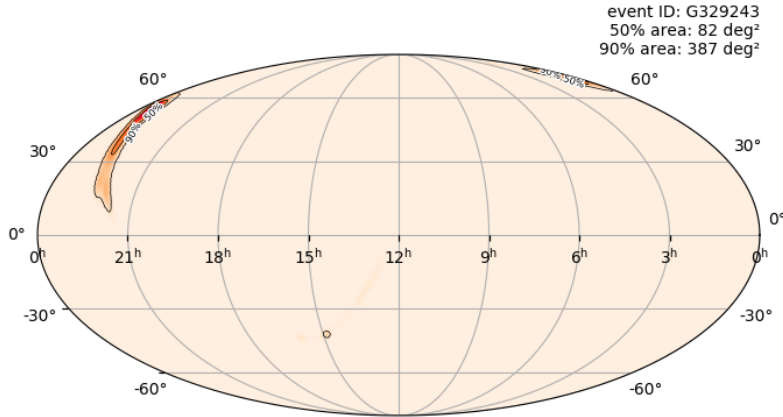


Figure 20: The probability density map of the GW event, S190408an[25]

4.2 High Energy analysis

The High Energy(ATMPD which notates ATMOspheric neutrino and Proton Decay analysis)framework is built independently of the rest of the framework. It consists in a watcher script waiting for new gravitational wave events in the alert database. When it is received, the script is then looking for the processing of the Super-Kamiokande data of the few minutes around the time of the external trigger, there are three possible scenarios:

- **data already processed:** the High Energy analysis can be launched directly
- **data not processed:** the script is waiting for the data to be ready. More precisely, we wait till the last processed run (according to the run summary file on the analysis machine) has an end time later than $(t_{\text{alert}} + 1000 \text{ s})$. When this condition is fulfilled:
 - if there is **no run covering the $\pm 500 \text{ s}$ time window** centered on the external trigger, the High Energy analysis is anyway launched, in order to produce the minimal output.
 - if there are **some runs covering the time window**, we wait for the end of the processing of FC, PC and UPMU files

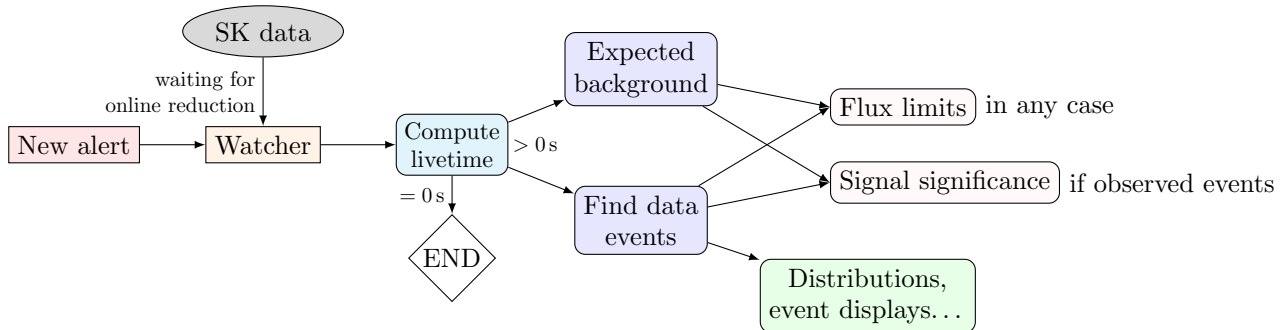


Figure 21: Overview of the High Energy analysis

4.2.1 Event selection

In High Energy region , we have three samples:

- Fully-Contained (FC): neutrino interacts in the inner detector and the outgoing lepton has a short range, leading to a clear ring in the inner detector and nothing in the outer detector. The typical neutrino energy range is 0.1 GeV to 10 GeV.
- Partially-Contained (PC): neutrino interacts in the inner detector and the outgoing lepton exits the detector, leading to a disk in the inner detector and one cluster in the outer detector. The typical neutrino energy range is 0.1 GeV to 100 GeV.
- Up-going muons (UPMU): neutrino interacts in the rock or in the water in the outer detector. One or two clusters are detected in the outer detector as well as light in the inner detector. Most of the events are through-going, which means it can be fitted with a straight line crossing the full detector. Only events coming from above horizon are selected, in order to reject most of the down-going atmospheric muon background. The typical neutrino energy range is 1.6 GeV to 10 000 GeV.

When an external trigger comes, only the files containing the runs covering the 1000 s time window are processed. As runs are typically 24h-long, we need to further pre-select the events within the time window. This is done by using `jd` and `fjd` variables (where `jd` and `fjd` are respectively the integer and the fractional part of the Julian date of event).

The final selection cuts applied in the analysis are following the standard cuts used in the official ATMPD software:

- FC:
 - `wall>100` (cut on the distance to the wall in cm)
 - `evis>30` (cut on visible energy in MeV)
 - `nhitac<16` (cut on number of OD hits)
- PC:
 - `wall>200` (cut on the distance to the wall in cm)
 - `evis>350` (cut on visible energy in MeV)
 - `nhitac>=16` (cut on number of OD hits)
- UPMU:
 - `Fit_directional z>0` (up-going events)
 - Stopping muons: `Fit_pid==1` and `Fit_mom>1.6` (cut on fitted momentum in GeV)
 - Or through-going muons: `Fit_pid==2` and `Fit_len>700` (cut on fitted track length in cm)

We store all events in the time window of each sample in ROOT files, and make official sample reductions. This paper will use these samples for analysis, regardless of whether they passed the official sample reduction or failed (because the latter can be used for further inspection or adjustment). In addition to the official variables, three new variables have been added:

- `selected` is a boolean variable indicating if the event passed the official sample cuts or not. The events with `selected==True` are the ones to be considered for final analysis.
- `delta_t` is the time difference [in seconds] between the neutrino event and the external trigger time.
- `sigma_ang` is the expected $1 - \sigma$ angular resolution of the event. It is estimated as a function of reconstructed energy.

4.2.2 Background estimation and characteristics

The three High-Energy samples are dominated by atmospheric neutrinos, that will therefore be the dominant background for the analysis. Fortunately the rate of such events is quite stable with time and their angular distribution only depends on zenith angle θ . However, it will have to be carefully treated in the subsequent statistical analysis, as the Earth rotation makes the background at a given position (δ, α) is varying with time, because the corresponding θ changes with time .

$$\begin{aligned}\sin \delta &= \cos \phi_{SK} \cos a \cos A + \sin \phi_{SK} \sin a \\ \cos h &= \frac{\sin a - \sin \delta \sin \phi_{SK}}{\cos \delta \cos \phi_{SK}} \\ \sin h &= \frac{-\sin A \cos a}{\cos \delta} \\ \alpha &= \theta_L - h\end{aligned}\tag{16}$$

For the integrated expected number of background event, due to its stability, it can easily estimated by multiplying Super-Kamiokande livetime in the selected time window by the average background rate.

Background: For each sample, the background rate is estimated using the full dataset of the current SK period, where background is assumed to be stable. This is done by counting the total number of events passing the selection cut and dividing by the total livetime.

For the real-time processing (and therefore during SK data acquisition), the full SK dataset is not available. We then use a sufficiently large sub-sample of data that have already been processed. When the dataset is officialised (after e.g. eye-scans and use of official calibration constants), we can use it in order to estimate the background event rate. Results are shown in [Table 1](#).

Table 1: Background event rate using realtime processing (runs 80027 ~ 82389) and official SK5 dataset of May 2020 (runs 80031 ~ 82585) with the associated statistical errors.

	Sample	Event rate [s^{-1}]	Error on event rate [s^{-1}]
Realtime	FC	1.109×10^{-4}	0.021×10^{-4}
	PC	7.262×10^{-6}	0.540×10^{-6}
	UPMU	2.102×10^{-5}	0.092×10^{-5}
Official	FC	1.120×10^{-4}	0.020×10^{-4}
	PC	7.279×10^{-6}	0.490×10^{-6}
	UPMU	1.637×10^{-5}	0.073×10^{-5}

Livetime: In SK analysis, we usually take 24 hours data as a normal run, and divide into subruns. The livetime is estimated using the specific run(s) overlapping with the selected time window. For each run, contains the computed livetime L_s and deadtime D_s for each subrun, but the subrun start time t_s is only precise to the minutes and therefore it is not enough to know which fraction of a given subrun is overlapping with the time window.

Taking into account the fact that each subrun is approximately 2 min-long, we select the subruns that are located within few minutes of the selected time window $[t_1, t_2]$:

$$t_1 - 3 \text{ min} < t_s < t_2 + 1 \text{ min}\tag{17}$$

For these subruns, the reformatted root files are used to extract the precise start and end time of the subrun (using GPS time, precise to the nanoseconds). We can then compute the fractional overlapping O_s of the subrun with the time window. We have $O_s = 0$ (resp. $O_s = 1$) if the subrun is completely outside (resp. inside) the time window.

The total livetime of Super-Kamiokande over the selected time window $[t_1, t_2]$ is:

$$L = \sum_s O_s \times L_s\tag{18}$$

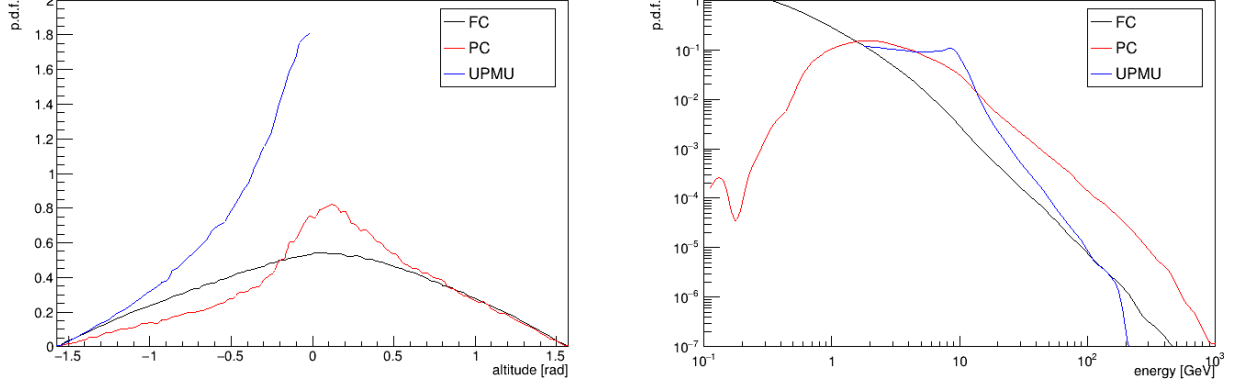


Figure 22: Angular and energy dependence of atmospheric neutrino background, using SK4 Monte Carlo. The distributions are normalised to unity.

Background characteristics: For the statistical analysis, it will be needed to quantify if a given event in Super-Kamiokande is compatible with background or not. This is done by using two discriminatory variables: direction and energy. Background will have one behaviour (atmospheric-like spectrum, isotropic angular distribution) while signal will behave differently (different spectrum, pointing to the source).

The Fig.21 shows the angular and energy distribution for background using SK4 Monte Carlo and the selection cuts described in Sec.4.2.1.

4.2.3 Signal characteristics

In order to extract some limits, sensitivity and significance from the observations, it is needed to characterise the behaviour of the expected astrophysical neutrino signal.

Neutrino effective area: Neutrino effective area allows converting from an incoming flux to a number of expected events in the detector.

$$n_{\text{sig}} = \int A_{\text{eff}}(E, \Omega) \frac{d^2 n}{dE d\Omega} \times dE d\Omega \quad (19)$$

For an instantaneous flux $\frac{dn}{dE} [\text{cm}^{-2} \text{GeV}^{-1}] = \phi_0 [\text{cm}^{-2} \text{GeV}^{-1+\gamma}] E^{-\gamma}$ from a source at position Ω_{src} :

$$n_{\text{sig}} = \int A_{\text{eff}}(E, \Omega_{\text{src}}) \times \phi_0 E^{-\gamma} \times dE \quad (20)$$

The effective area (A_{eff}) depends on the considered sample, on the considered neutrino flavour ($\nu_\mu, \nu_e, \bar{\nu}_\mu, \bar{\nu}_e$), on neutrino energy and on direction (more precisely the zenith angle θ , for simplicity we neglect the dependency with azimuth)

The effective area can be estimated using Monte Carlo simulations. For Super-Kamiokande, the biggest available sample is the standard atmospheric MC, corresponding to 500-years-equivalent. In the analysis, we use the SK4 Monte-Carlo.

For a given neutrino flavour, we know the atmospheric neutrino flux $\Phi_{\text{atm}}(E, \theta) [\text{GeV}^{-1} \text{cm}^{-2} \text{s}^{-1} \text{sr}^{-1}]$. For a given bin $[E, E + dE]$, $[\theta, \theta + d\theta]$ (integrating over azimuth angle) in terms of truth information, for a given livetime T (e.g. 500 years), we then define $M_{\text{true}}^{\text{bin}}$ [in cm^{-2}]:

$$M_{\text{true}}^{\text{bin}} = \Phi_{\text{atm}}(E, \theta) \times dE \times \sin \theta d\theta \times 2\pi \times T \quad (21)$$

For a given sample and neutrino flavour, we can look for the number of events after simulation + reconstruction + selection in the same bin (truth information) $N_{\text{selected}}^{\text{bin}}$. The effective area for this particular sample is estimated to be:

$$A_{\text{eff}}^{f,s}(E, \theta) = \frac{N_{\text{selected}}^{\text{bin}}}{M_{\text{true}}^{\text{bin}}} \quad (22)$$

By averaging over the zenith angles[?] [?], we can get the effective area as a function of energy only, as it is often pictured in astrophysical publications(e.g[1]).

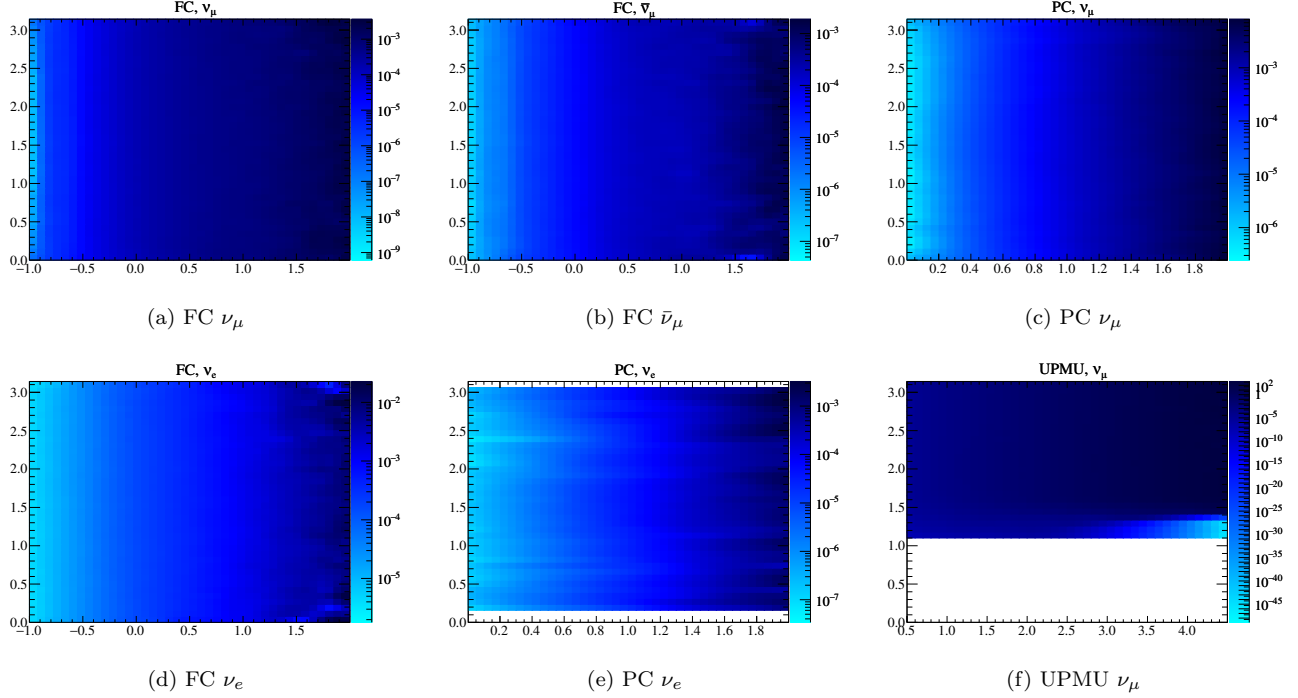


Figure 23: Effective area as a function of neutrino energy ($\log(E[\text{GeV}]$ on x-axis) and zenith angles (rad on y-axis) for a selection of samples and neutrino flavours.

We see a small dip in the FC plot, around $\log(E[\text{GeV}])=-0.6$ corresponding to $E \sim 250$ MeV.

Angular resolution: For a given neutrino detection in Super-Kamiokande, the reconstructed direction is not pointing exactly to the neutrino direction. There are two reasons for that:

- During a neutrino-nucleus scattering, the outgoing muon is not aligned with the incoming neutrino direction because there is a momentum exchange with the nucleus. This effect is particularly important for the lower momentum, as shown in Fig.25: 30° at 1 GeV and 0.01° at 3 TeV.
- The Super-Kamiokande reconstruction is not perfect and therefore the angle between the reconstructed direction of the muon and its true direction is not zero. This effect depends on the considered sample but is more independent of the initial neutrino energy.

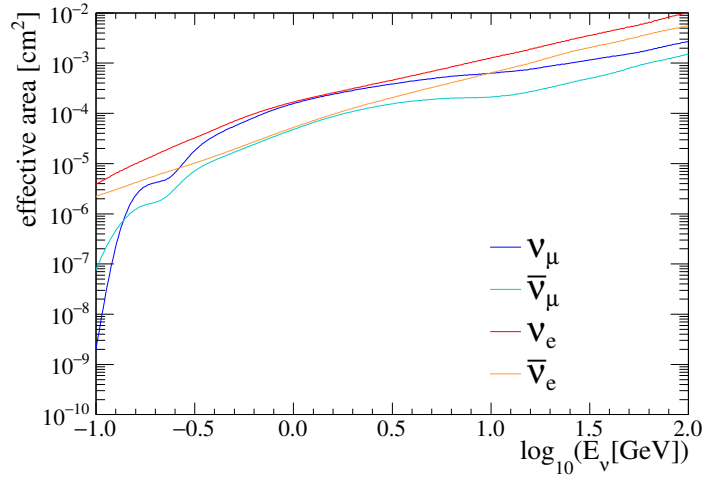
As the goal in this analysis is to reconstruct the position of the source (a.k.a. the neutrino direction) based on the only information we have, i.e. the direction of reconstructed event. Therefore we only care about the composition of the two effects: resolution for the angle between true neutrino and reconstructed direct of the event.

In order to estimate the resolution, we use SK4 Monte Carlo. For each sample (FC, PC, UPMU), we apply the normal event selection and plot $\Delta\Phi = \text{Angle}(a_\nu^{\text{true}}; a_{evt}^{\text{reco}})$ vs reconstructed energy (visible energy for FC/PC, fitted momentum for UPMU).

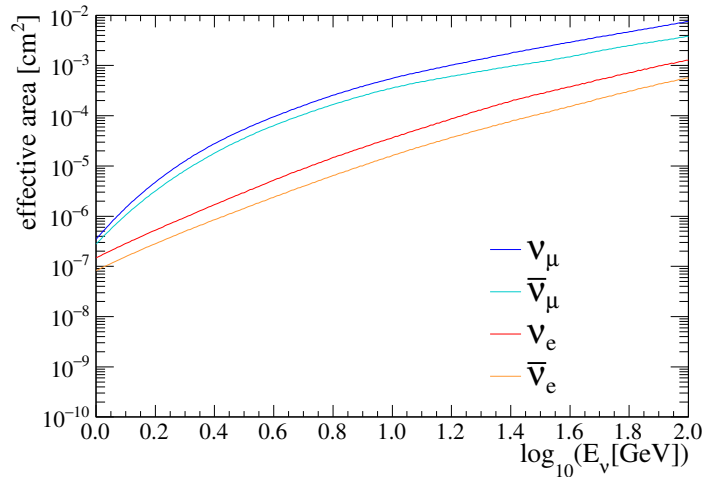
Then, for different bins in reconstructed energy (sufficiently large to contain enough statistics, we project the previous plot in one-dimension:Fig.26. This allows to obtain the p.d.f. describing the distribution of $\Delta\Phi$ for a given reconstructed energy.

This will be of particular importance in two occasions:

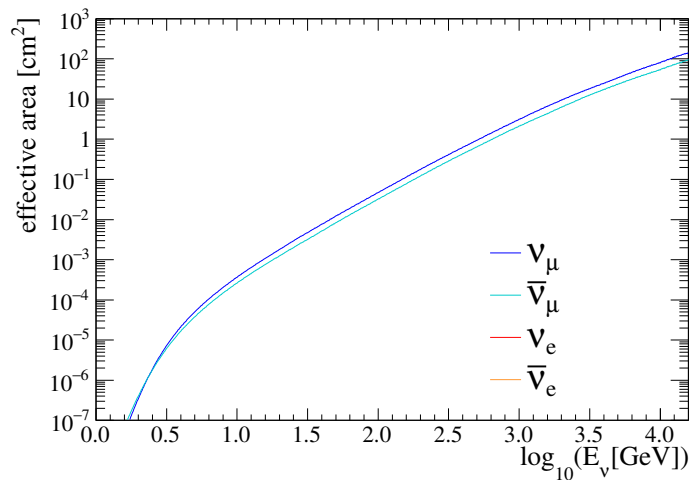
- quantify the agreement between the reconstructed direction of a given event and an assumed source direction
- simulate fake signal event from a given point source, taking into account resolution effect



(a) FC



(b) PC



(c) UPMU

Figure 24: Effective area as a function of neutrino energy for the three ATMPD samples. The different lines correspond to the different neutrino flavours.

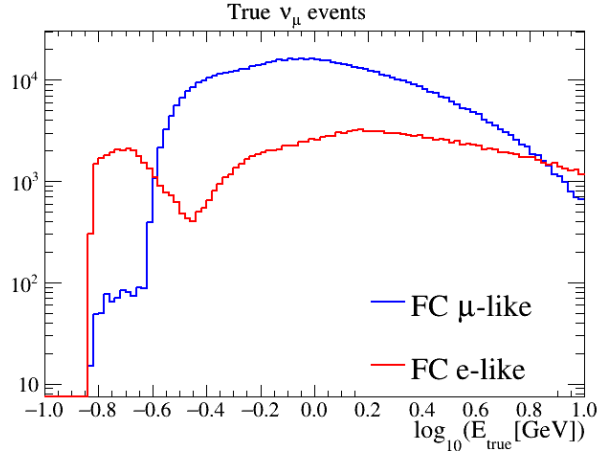


Figure 25: Distribution of true neutrino energy for true ν_μ events, separated between events reconstructed as μ -like or e -like.

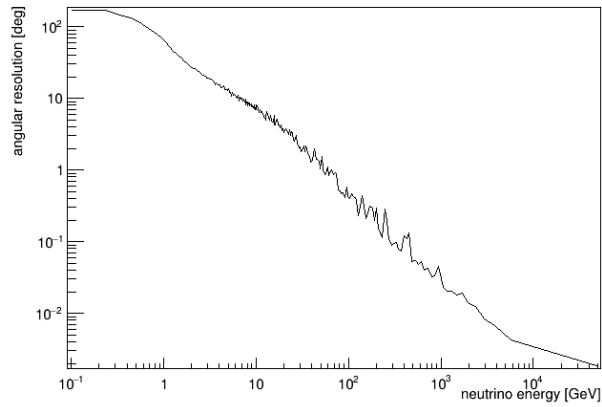


Figure 26: Root mean square of the angle between the true direction of the neutrino and the true direction of the muon, for different values of energy.

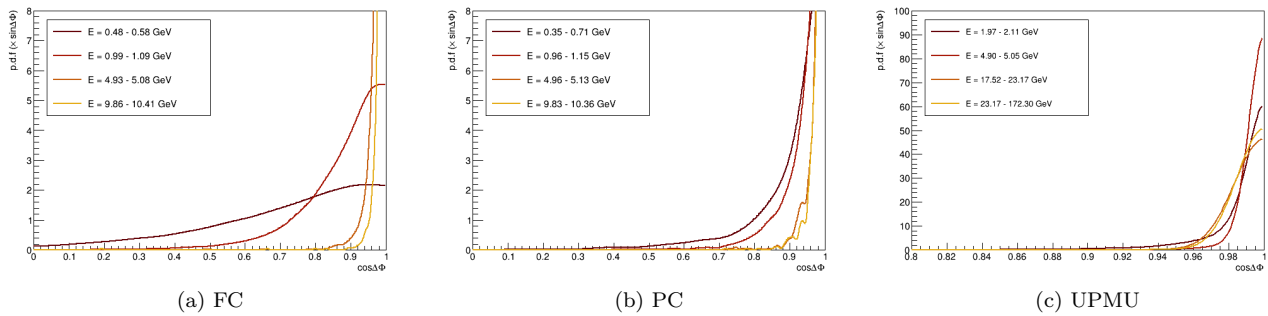


Figure 27: Probability density function of $\cos \Delta\Phi$ for different bins in energy.

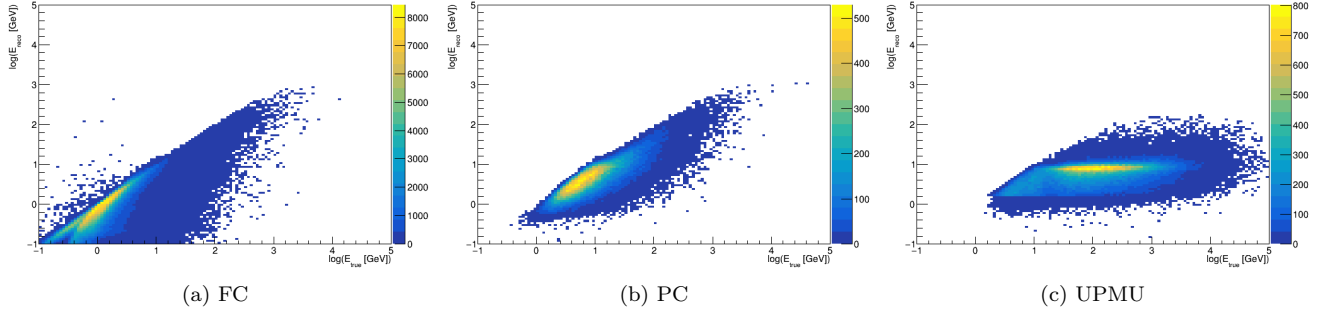


Figure 28: Distribution of true neutrino energy (quantity of interest) vs reconstructed event energy (measured quantity) for the different samples.

For these purposes, it is needed to smoothen the distribution: this is done by fitting it.

For a given energy, we expect:

$$P(\Delta\Phi; E) = A \sin \Delta\Phi \exp\left(-\frac{\Delta\Phi^2}{2\sigma(E)^2}\right) \quad (23)$$

where $\sigma(E)$ is the angular resolution. Therefore:

$$P(x = \cos \Delta\Phi; E) = A' \exp\left(-\frac{(\arccos x)^2}{2\sigma(E)^2}\right) \quad (24)$$

As the plots are done for a range of energy instead of one, the p.d.f. are better fitted with the sum of two distributions Eq.24 with different sigma values (to cover the difference in angular resolutions over the energy range).

Energy reconstruction: The true neutrino energy spectrum of the signal is often thought as being of the form:

$$\frac{dn}{dE} = \phi_0 E^{-\gamma} \quad (25)$$

where γ is the spectral index. While atmospheric neutrinos correspond to $\gamma_{\text{atm.}} = 3$, astrophysical publications are often referred to $\gamma_{\text{astro.}} = 2$ when giving upper limits on flux or significance, even though there are some hints that this is not fitting perfectly the current data.

Even if the true neutrino spectrum is fixed, it is still needed to convert to reconstructed energy in order to predict the expected energy distribution of observed events from the source. The Fig.27 shows how true neutrino energy relates to the reconstructed energy.

As we have done for the angular resolution, we can project in 1D and plot $R = E_{\text{reco}}/E_{\text{true}}$ for different true energy bins. Some example plots are shown in Fig.28.

To convert from true energy E_{true} to reconstructed energy E_{reco} , we select the correct 1D plot and select one value of R using this plot and use $E_{\text{reco}} = R_{\text{thrown}} \times E_{\text{true}}^{\text{initial}}$.

4.2.4 Outputs

We can separate the output in three categories:

- **Basic information about SK data-taking:** Was the detector running? What is the coverage of the sky if we consider only upgoing muons (relevant for the UPMU sample)? ...
- **Event information:** How many events are observed in SK? what is the expected background? What are the energy/direction of these events?
- **SK-GW information:** What is the distribution of the time difference between neutrino detection and trigger? Where are the events localised with respect to the gravitational wave skymap?

In the following, I want to make the example of S190513bm.

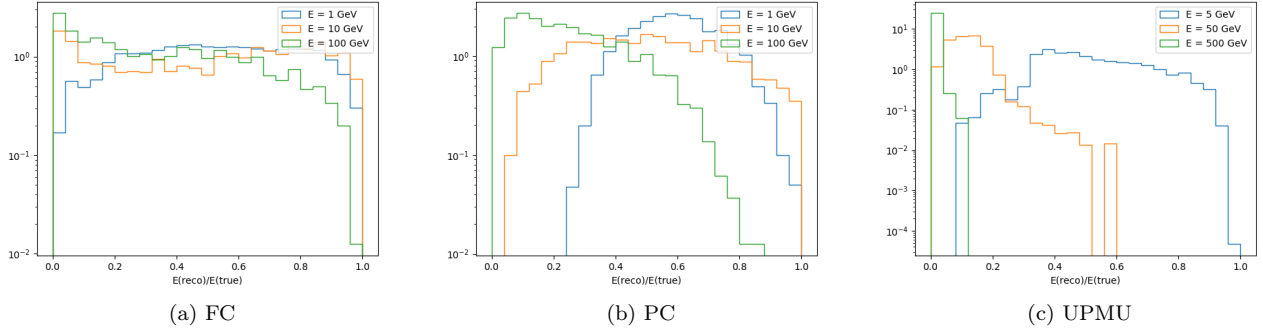


Figure 29: Distribution of $E_{\text{reco}}/E_{\text{true}}$ for different true neutrino energies and different samples.

Detector status The list of runs/subruns that are covering the 1000 s time window around a given gravitational event is given, with their corresponding livetime and fractional overlapping with the time window (according to the method presented in Sec.4.2.2), as shown in Tab.2. The main output is then the total livetime of Super-Kamiokande over the 1000 seconds.

Table 2: Status of Super-Kamiokande on the 1000 seconds time window around S190513bm.

Run	Subrun	Start time (JST)	Livetime (seconds)	Overlapping (%)
81163	334	190514/05:44	116.44	30.80
81163	335	190514/05:46	116.11	100.00
81163	336	190514/05:48	114.80	100.00
81163	337	190514/05:50	114.74	100.00
81163	338	190514/05:52	113.10	100.00
81163	339	190514/05:54	114.68	100.00
81163	340	190514/05:56	117.77	100.00
81163	341	190514/05:58	117.79	100.00
81163	342	190514/06:00	116.60	100.00
81163	343	190514/06:02	115.60	27.78
TOTAL (over 1000s)			993.57	

The Super-Kamiokande status can then be classified into three main categories:

- Livetime > 950 s: Super-Kamiokande is taking good quality data over the full time window (sign of normal operation of the detector).
- $0 < \text{Livetime} < 950$ s: Super-Kamiokande is taking good quality data only for a fraction of the time window (sign that there may have been a change of run in the middle or some calibration ongoing).
- Livetime = 0 s: Super-Kamiokande was down during the time window (because of an ongoing calibration period or other issues)

The upcoming muon sample can only be used to detect neutrinos coming from a negative altitude. The coverage skymap is showing which part of the sky is accessible at the time of the alert, e.g. Fig.29. This plot is obtained by simply computing the altitude a corresponding to each point of the sky at the time of the alert and checking if a is positive (above horizon, not seen by UPMU, coverage=0 in the plot) or negative (below horizon, seen by UPMU, coverage=1 in the plot). The boundary between the two regions are intermediary values, because they correspond to sky positions that are below the horizon only for a fraction of the time window ; as the time window is short with respect to one day (1000 s over 86 400 s), this effect is relatively small.

Events in Super-Kamiokande All the events passing the selection of Sec.4.2.1 are saved in a list. It is then saved in a text file with all relevant information.

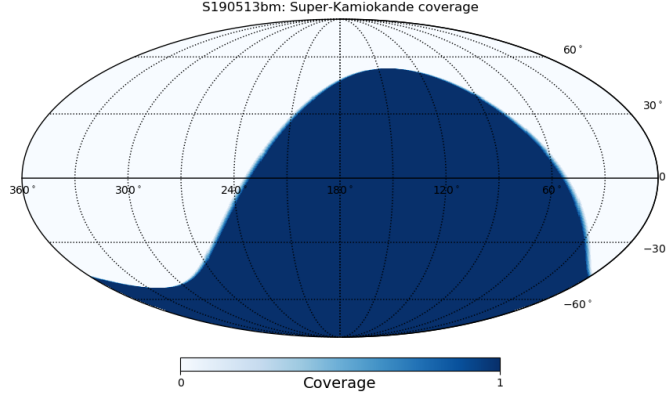


Figure 30: Coverage of the sky with UPMU sample, for the S190513bm event.

Table 3: List of Super-Kamiokande events for S190513bm

Event Time	Delta T	Event Type	Energy [GeV]	RA [deg]	Dec [deg]
2019-05-13 20:51:28	-183.273	FC	0.678	278.722	-37.455

Plots showing their time distribution and the spatial distribution are also obtained, as shown in Figures 31a and 31b. The spatial distribution is superimposed with the skymap provided by the LIGO/Virgo collaboration, allowing direct comparison of sky positions.

Based on the reconstructed energy, the angular uncertainty for each SK events can also be provided.

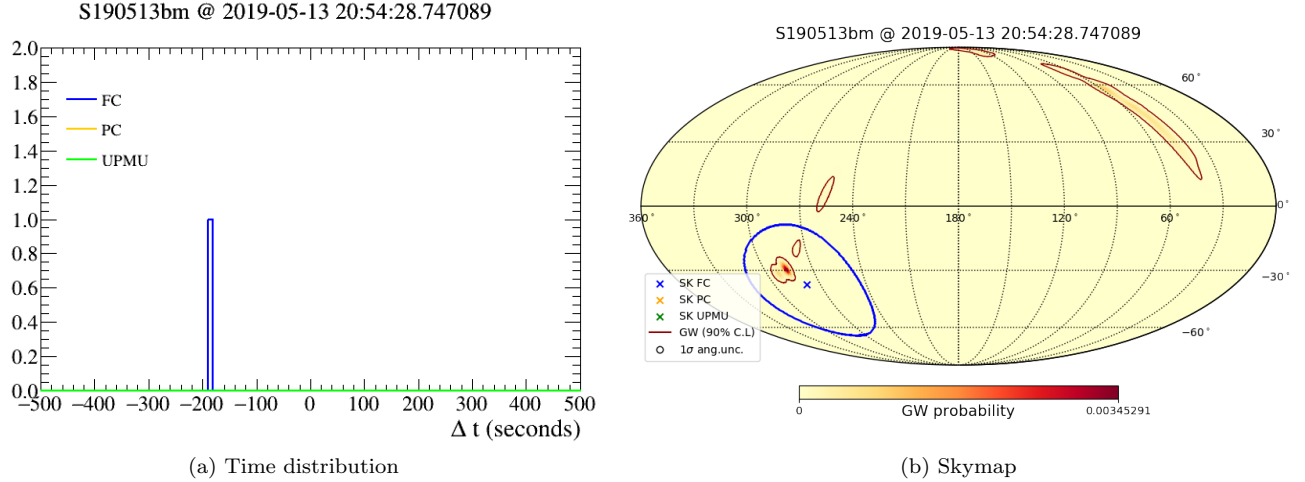


Figure 31: Plots of Super-Kamiokande events for S190513bm.

Summary of number of observed events and expected background The number of observed events in Super-Kamiokande can be compared to the expected background (coming mainly from standard neutrino interactions).

4.3 Low Energy analysis

The LOWE framework is also built independently of the rest of the framework and also consists in a watcher script waiting for new gravitational wave events in the alert database. When it is received, the script is then looking for the processing of the Super-Kamiokande data of the few minutes around the time of the external trigger, the LOWE energy range is 3.5 Mev to 100 MeV.

- **data already processed:** the LOWE analysis can be launched directly
- **data not processed:** the script is waiting for the data to be ready. More precisely, we wait till the last processed run (according to the run summary file on sukup) has an end time later than ($t_{\text{alert}} + 1000\text{s}$). When this condition is fulfilled:
 - if there is **no run covering the $\pm 500\text{s}$ time window** centered on the external trigger, the LOWE analysis is anyway launched, in order to produce the minimal output
 - if there are **some runs covering the time window**, we wait for the end of the processing of make lowe sample

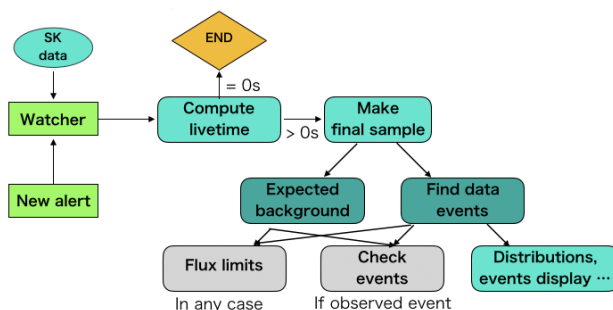


Figure 32: LOWE framework.

4.3.1 Event selection

Assuming that the flux is approximately equally distributed among flavors, as for a core-collapse supernova, the dominant channel in the 3.5 MeV to 100 MeV range is the inverse beta decay of electron antineutrinos $\bar{\nu}_e + p = e^+ + n$. The second-most dominant one is neutrino elastic scattering $\nu + e^- = \nu + e^-$, which is sensitive to all neutrino flavors but dominated by electron neutrinos. Positrons or electrons from these interactions can produce observable signals in the SK detector. There are other charged-current and neutral-current interactions with ^{16}O nuclei that are subdominant.

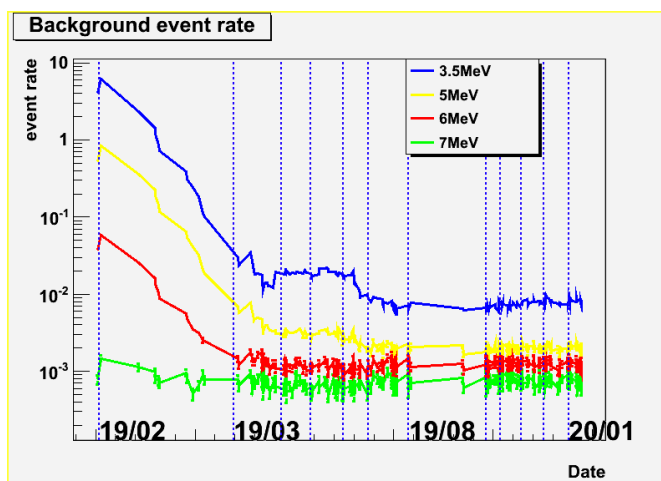


Figure 33: LOWE background event rate.

But in our analysis we choose to use 7 MeV to 100 MeV because we compared with the background of low event (with over 3.5 MeV, 5 MeV, 6 MeV, 7 MeV).

By comparing with background event rate in low cases, we found that event rate which is over 7 MeV is most stable in this analysis. The reason is when in the beginning of SK5 state, the water system is not stable and more noise is appeared like decay of Radon. It is necessary to cut with 7 MeV that we can get a more stable data.

4.3.2 Background estimation and characteristics

As we discussed in low events selection, we cut both background and signal event in 7 MeV and

For the integrated expected number of background event, due to its stability, it can easily estimated by multiplying Super-Kamiokande livetime in the selected time window by the average background rate.

Background rate For each sample, the background rate is estimated using the full dataset of the current SK period, where background is assumed to be stable. This is done by counting the total number of events passing the selection cuts and dividing by the total livetime.

Background selection In LowE cases, we try to compare with the background only in one SK normal run and a week before GW event. The data shows that one week background is more stable than one SK normal run data. We calculate the average of background event rate is 0.729(events/1000s) by using all of the data from SK5 beginning, and compared average of all data with recent 7 days data.

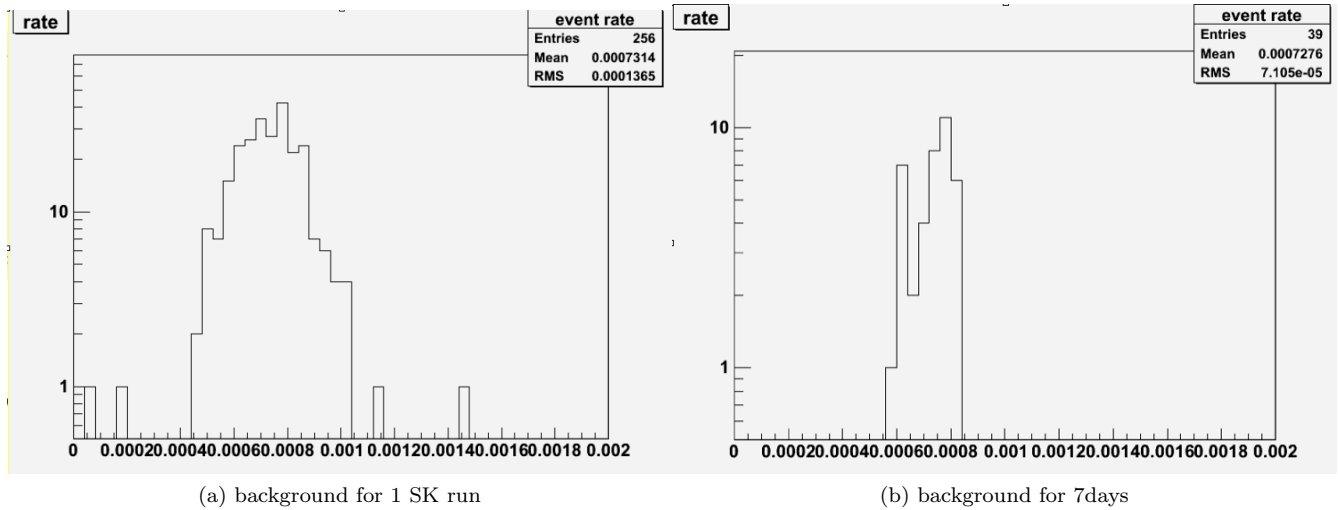
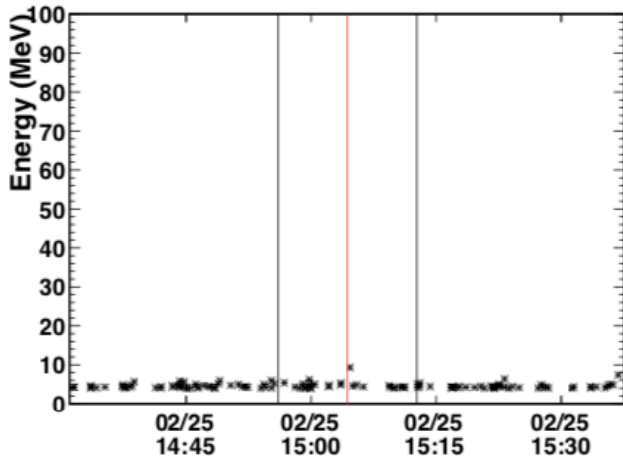


Figure 34: Estimation of the background rate

If the Recent background data is 3σ greater than average background, we choose to use the Recent background and if not we use the average background to calculate.



(a) Time plot

Event Time	Delta T [s]	Energy [MeV]
2020-02-25 15:04:40.396973	19	9.30239

(b) List of selected events

Figure 35: Example of S200225q.

Table 4: Fluence limit sample for S200316bj.

GW alert S200316bj	FL(Fer-Dir) ν_e	FL(Fer-Dir) $\bar{\nu}_e$	FL(Fer-Dir) ν_x	FL(Fer-Dir) $\bar{\nu}_x$
	1.1E+10	6.8E+10	9.7E+08	8.0E+10
GW alert S200316bj	FL(Flat) ν_e	FL(Flat) $\bar{\nu}_e$	FL(Flat) ν_x	FL(Flat) $\bar{\nu}_x$ (%)
	1.2E+10	7.2E+10	1.1E+09	8.4E+10

4.3.3 Outputs

Like High Energy work we can separate the output in two categories:

- **Event information:** How many events are observed in SK(Energy from 3.5MeV to 100MeV)? what is the expected background? What are the energy/direction of these events?
- **Calculate information:** 90 percent Confidence level and fluence limit for Fermi-Dirac spectrum($E_{ave} = 20$ MeV), Flat spectrum, and some energies(5,7,10,14,20,30,50,80,100MeV)

Event information We make plot for each event in ± 500 s in low region(Energy from 3.5MeV to 100MeV).And we select event over 7MeV in N90 calculation and fluence limit calculation.

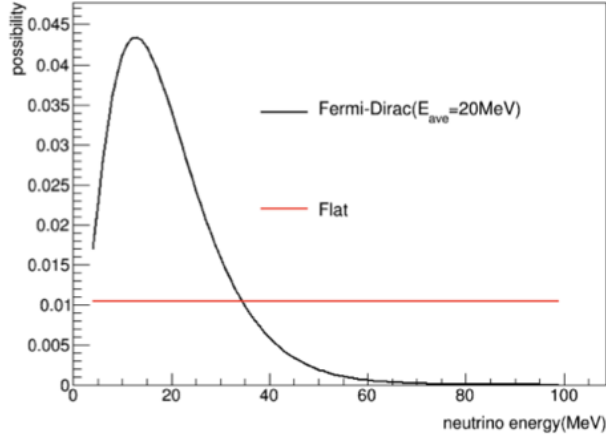


Figure 36: Fermi-Dirac Spectrum ($E = 20$ MeV).

Calculate information We calculate N90 and fluence limit event by event by using low energy event ($E_i > 7$ MeV).For fluence limit, we calculate in 2 types of energy spectrum(Fermi-Dirac,flat) and in mono-energetic(5,7,10,14,20,30,50,80,100MeV).

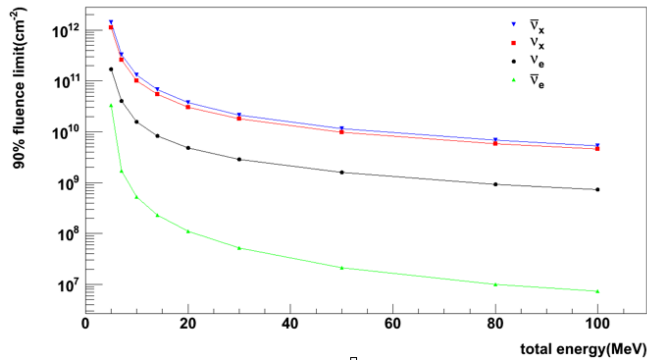


Figure 37: Fluence limit as a function of energy.

5 Statistical analysis

5.1 Introduction

The main goal of the Gravitational Wave follow analysis is to conclude whether or not we have detected a joint source of gravitational waves and neutrinos. If there is no conclusive observations, we want to be able to put upper limits on the incoming neutrino flux from the GW source.

There have been numerous publications in Super-Kamiokande and in other collaborations where different methods have been used in order to obtain such results, going from the simple flux limits to some extensive frequentist or bayesian studies.

5.1.1 Super-Kamiokande approach in previous analyses

In the recent years, the Super-Kamiokande collaboration has published several papers related to the search for neutrinos in coincidence with detected gravitational waves or other transient events: Gamma-Ray Bursts from 1996 to 2000 [18], GRB 080319B [30], GW150914 & GW151226 [8], GW170817 [9], Blazar TXS 0505+056 [21].

In all the papers mentioned above, there have been no significant enough observation to claim for discovery from the various tests performed in the analyses (searching for time coincidence only, searching for spatial coincidence in all data, ...). However, all of them use a very similar approach to extract limits on the neutrino flux/fluence.

Fluence limits Assume an observation of N_{obs} events in a time window T_w centered on the alert time. The expected number of events from background-only can be simply expressed as: $N_b = \delta t(T_w) \times r$, where r is the background event rate. These two information is converted to an upper limit on the number of signal events N_s by using Poisson statistics where N_{obs} is a realisation of the Poisson process with $\lambda = N_s + N_b$. There are different methods to obtain an upper limit N_s^{CL} at a given confidence level CL directly from the Poisson probability (we get for instance $N_s^{90\%} = 2.3$ for $N_{\text{obs}} = N_b = 0$).

As we have seen in Eq.19, the number of signal events can be related to the flux by integrating over energies with an additional factor A_{eff} that is taking into account all the effects related to the detector and to neutrino interaction properties. In all previous Super-Kamiokande publications, the notion of effective area is not used explicitly but its different components are explicited.

It is worth noting that, depending on the considered sample (FC, PC, UPMU, LOWE), the formula to be used is not the same because these different samples do not have the same energy ranges and efficiencies.

In the following, we write the flux from a point-source for a given neutrino flavour f :

$$\frac{dn}{dE} [\text{GeV}^{-1} \text{cm}^{-2}] = \Phi^f [\text{cm}^{-2}] \times \lambda(E) [\text{GeV}^{-1}] \quad (26)$$

where $\lambda(E)$ is a shape function such that $\int \lambda(E) dE = 1$ and Φ^f is the fluence (in cm^{-2}). For an assumed neutrino energy spectrum with spectral index γ , we have $\lambda(E) \propto E^{-\gamma}$ and we can also rewrite the flux as:

$$\frac{dn}{dE} = \phi_0 \times E^{-\gamma} \quad (27)$$

where ϕ_0 is the flux constant and can easily be related to the fluence:

$$\Phi^f = \frac{\phi_0}{1-\gamma} \left(E_{\text{max}}^{1-\gamma} - E_{\text{min}}^{1-\gamma} \right) \quad (28)$$

for $\gamma \neq 1$, using simple integration of the spectrum between its boundaries E_{min} and E_{max} .

In high energy, we have:

$$\Phi_{\text{FC}}^{\nu_x + \bar{\nu}_x} = \frac{N_{90}^{\text{FC}}}{N_T \int dE_\nu (\sigma^{\nu_x}(E_\nu) \varepsilon^{\nu_x}(E_\nu) + \sigma^{\bar{\nu}_x}(E_\nu) \varepsilon^{\bar{\nu}_x}(E_\nu)) \lambda(E_\nu)} \quad (x = e, \mu), \quad (29)$$

$$\Phi_{\text{PC}}^{\nu_\mu + \bar{\nu}_\mu} = \frac{N_{90}^{\text{PC}}}{N_T \int dE_\nu (\sigma^{\nu_\mu}(E_\nu) \varepsilon^{\nu_\mu}(E_\nu) + \sigma^{\bar{\nu}_\mu}(E_\nu) \varepsilon^{\bar{\nu}_\mu}(E_\nu)) \lambda(E_\nu)}, \quad (30)$$

$$\Phi_{\text{UPMU}}^{\nu_\mu + \bar{\nu}_\mu} = \frac{N_{90}^{\text{UPMU}}}{A_{\text{eff}}(\theta) \int dE_\nu (P^{\nu_\mu}(E_\nu) S^{\nu_\mu}(\theta, E_\nu) + P^{\bar{\nu}_\mu}(E_\nu) S^{\bar{\nu}_\mu}(\theta, E_\nu)) \lambda(E_\nu)}. \quad (31)$$

where N_T is the number of nucleons (targets) in the fiducial volume, σ is the neutrino-nucleus cross section, ϵ refers to detection efficiency, P is the probability for a neutrino to produce a muon in the surrounding rock that will reach the detector, S covers the neutrino flux attenuation from the Earth and $A_{\text{eff}}(\theta)$ is the muon geometrical effective area (function only of zenith angle).

In this particular example, neutrino and anti-neutrinos of the same flavour are considered together but they can also be considered separately.

In [21], the integration boundaries are 5.1 GeV to 10 GeV for FC, 1.8 GeV to 100 GeV for PC, 1.6 GeV-10 TeV for UPMU. In [9], they are 0.1 GeV to 10 GeV for FC-PC, 1.6 GeV-100 PeV for UPMU.

And also in Low energy, we have:

$$\Phi_{LowE} = \frac{N_{90}^{LowE}}{N_T \int dE_v \lambda(E_v) \sigma(E_v) R(E_v, E_{vis}) \epsilon(E_{vis})} \quad (32)$$

Where R is the response function to convert electron or positron energy (E_e) to kinetic energy in SK (E_{vis}). The response function and the detection efficiency (ϵ) are calculated using SK detector Monte Carlo simulation

λ is the density of E_μ assuming an energy spectrum. Here we assume the spectrum is fermi-dirac distribution, flat and mono-energetic. (See in Fig.35 Fig.36)

We have seen we can rewrite all the previous equations in a simpler form using neutrino effective area:

$$\Phi_{90}^{s,f} = \frac{N_{90}^s}{\int dE_\nu A_{\text{eff}}^{s,f}(E_\nu, \theta) \lambda(E_\nu)} \quad (33)$$

for all samples s (\in FC, PC, UPMU, ...) and all flavours f (\in $\nu_\mu, \nu_e, \bar{\nu}_\mu, \bar{\nu}_e, \nu_\mu + \bar{\nu}_\mu, \nu_e + \bar{\nu}_e$). The effective area computation was already presented in Sec.4. It is worth noting that effective area depends on the zenith angle θ , so that fluence limits will depend on the position of the source. Previous analyses have either considered a fixed source position (because the position was well known from external observations) or scan over the sky (and therefore over different zenith angles).

Some of the previous analyses have also reported mono-energetic fluence limits, i.e. assuming $\lambda(E) = \delta(E - E_0)$ rather than a continuous spectrum. In [18], such limits $\Phi_{\text{mono}}(E)$ are computed and can therefore be used to obtain fluence limits assuming a given continuous spectrum λ by doing a convolution:

$$\Phi_\lambda = \left[\int \frac{\lambda(E)}{\Phi_{\text{mono}}(E)} dE \right]^{-1} \quad (34)$$

Observation significance In order to quantify if an observation done with Super-Kamiokande is consistent with the existence of a correlation between detected neutrino flux and external trigger, there have been different methods in the different publications.

The Table 5 summarises the analyses from these publications.

As can be seen, beyond simple Poisson tests and different methods for fluence limits, there have been no special statistical treatment to quantify if data indicate the discovery of a GW+ ν or not. We will therefore suggest new methods in the following sections.

5.2 Signal significance: first approach

If we want to quickly say if data are consistent or not with background-only hypothesis without any complicated statistical treatment, we can proceed with simple counting.

In Sec.4.2.2, we saw the expected number of events in a 1000 s time window is around $n_B = 0.111, 0.007$ and 0.021 , respectively for FC, PC and UPMU. In the background-only hypothesis, for a given sample, the number of observed events N should be distributed according to a Poisson distribution $\text{Poisson}(N, n_B)$.

For a given GW event, we get specific values of N and n_B (n_B can vary from above values if SK livetime is not 100%). We can therefore compute the p-value of the observation for each sample s :

$$p_s = \sum_{k=N_s}^{\infty} \text{Poisson}(k, n_B^s) \quad (35)$$

If we have $N = 0$, we get $p = 100\%$ (observation fully consistent with background). If we have $N_{\text{FC}} = 1$ (resp. $N_{\text{UPMU}} = 1$), we get $p \sim 10.5\%$ (resp. $p \sim 2.1\%$).

¹special sample of events with $> 1.75 \times 10^6$ p.e in the ID

Table 5: Summary of the different strategies to evaluate neutrino+external trigger coincidence.

Ref.	Evt.type	SK samples	Time/spatial window	Tests	Spectrum
[18]	GRBs 1996 ~ 2000	LE HE- e HE- μ UPMU	$\pm 10 - 100 - 1000s$ $\pm 10 - 100 - 1000s$ $\pm 10 - 100 - 1000s$ $\pm 1000s, < 15^\circ$	Poisson p-value	E^{-2} , mono-E
[30]	GRB 080319B	LowE FC PC UPMU UHE ¹	$\pm 1000s$	-	E^{-2}
[8]	GW150914 GW151226	LowE FC+PC UPMU	$\pm 500s$	-	flat, mono-E E^{-2} E^{-2}
[9]	GW170817	LowE FC+PC UPMU	$\pm 500s$ $\pm 500s, +14d$ $\pm 500s, +14d < 5^\circ$	-	flat, Fermi-Dirac E^{-2} E^{-2}
[21]	Blazar TXS 0506+056	FC,PC UPMU	1996 ~ 2018, $< 10^\circ$ $\pm 500s, < 5^\circ$	event rate evolution (dev. from const.rate)	E^{-2} E^{-2} , mono-E

We can also do the test with the sum of the contribution of the different channels:

$$p = \sum_{k=\sum_s N_s}^{\infty} \text{Poisson}(k, \sum_s n_B^s) \quad (36)$$

If we have $N = 0$ (resp. $N = 1$), we get $p = 100\%$ (resp. $p \sim 12.9\%$).

Also in low energy, we use Poisson-distribution to calculate the p-value.

These tests are quite limited because they only consider the time correlation of the SK events with the GW. Moreover, they only probe the agreement of data with background hypothesis and not with the signal+background hypothesis.

However, it can be quite interesting to do the test with the combination of all GW events. In the following section, we will consider more advanced methods which take into account both time and spatial correlations in order to quantify signal significance.

5.3 Flux limits:sample-by-sample, position dependent

In a first time, we will reproduce the limits with a similar method with respect to what has been done in previous Super-Kamiokande publications. The inputs to the analysis will be the same:

- number of observed events in a given sample N_{obs}^s
- number of expected background events in the same sample B_{exp}^s

We produce a flux limit map following the current procedure:

1. Given an external trigger at time t_0 , for each sky position (δ, α) , we compute the corresponding zenith angle θ . We obtain a map as the one presented in [Figure 38](#).
2. For each SK sample, we compute the upper limit on the number of signal events from N_{obs}^s and B_{exp}^s using the Kraft, Burrows, and Nousek method [\[23\]](#). We will consider four different samples: FC, PC, UPMU and FC+PC (where we sum the contribution of the two samples). In the case of each flavour, we will consider this upper limit to be an upper limit on the number of signal neutrinos of this given flavour, even though we expect signal neutrinos to be distributed among the different flavours (with mixture 1:1:1 after standard oscillations).

3. For each neutrino flavour, SK sample and for each pixel of the map, we compute limit on $E^2 dn/dE$, assuming E^{-2} spectrum:

$$\phi_{90}^{s,f} = \frac{N_{90}^s}{\int dE_\nu A_{\text{eff}}^{s,f}(E_\nu, \theta) E_\nu^{-2}} \quad (37)$$

where the integration boundaries used in the analysis are covering the full range $E = 0.1 \text{ GeV}$ to 10^5 GeV .

4. This allows to obtain maps of flux limits. For UPMU, limits are computed only for zenith angles above $\pi/2$ i.e. positions below the horizon.
5. We can extract important numbers from these maps: the minimum and maximum values of the flux limits within the 90% contour. An example is illustrated in [Table 6](#).

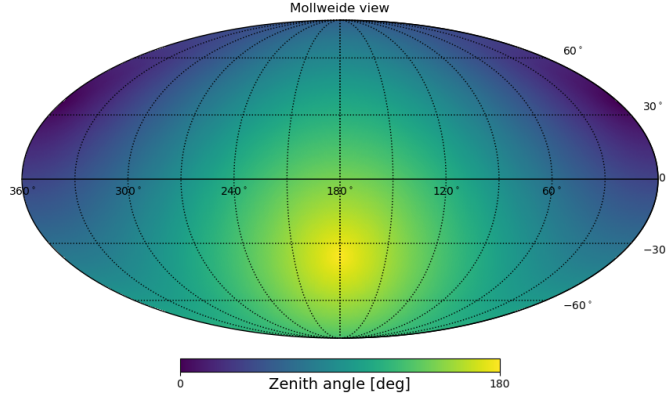


Figure 38: Example of zenith angle map for $LST = 0 \text{ h}$.

Table 6: Output of the analysis in terms of flux 90% upper limits (in $\text{GeV}\cdot\text{cm}^{-2}$) for the different samples and flavours, for the GW event S190412m. We assume E^{-2} spectrum.

Sample	Flavour	Min 90% _{GW}	Max 90% _{GW}	Marginalised
FC	ν_μ	$3.89 \cdot 10^3$	$4.03 \cdot 10^3$	$3.97 \cdot 10^3$
	ν_e	$2.16 \cdot 10^3$	$2.36 \cdot 10^3$	$2.28 \cdot 10^3$
	$\bar{\nu}_\mu$	$9.22 \cdot 10^3$	$9.58 \cdot 10^3$	$9.45 \cdot 10^3$
	$\bar{\nu}_e$	$4.76 \cdot 10^3$	$4.99 \cdot 10^3$	$4.88 \cdot 10^3$
	$\nu_\mu + \bar{\nu}_\mu$	$5.47 \cdot 10^3$	$5.67 \cdot 10^3$	$5.60 \cdot 10^3$
	$\nu_e + \bar{\nu}_e$	$2.97 \cdot 10^3$	$3.18 \cdot 10^3$	$3.10 \cdot 10^3$
	all	$3.88 \cdot 10^3$	$4.06 \cdot 10^3$	$3.99 \cdot 10^3$
PC	ν_μ	$4.83 \cdot 10^3$	$4.93 \cdot 10^3$	$4.86 \cdot 10^3$
	ν_e	$3.35 \cdot 10^4$	$3.92 \cdot 10^4$	$3.78 \cdot 10^4$
	$\bar{\nu}_\mu$	$7.23 \cdot 10^3$	$8.76 \cdot 10^3$	$8.44 \cdot 10^3$
	$\bar{\nu}_e$	$8.93 \cdot 10^4$	$1.27 \cdot 10^5$	$1.10 \cdot 10^5$
	$\nu_\mu + \bar{\nu}_\mu$	$5.82 \cdot 10^3$	$6.31 \cdot 10^3$	$6.16 \cdot 10^3$
	$\nu_e + \bar{\nu}_e$	$5.27 \cdot 10^4$	$5.76 \cdot 10^4$	$5.59 \cdot 10^4$
	all	$1.05 \cdot 10^4$	$1.14 \cdot 10^4$	$1.11 \cdot 10^4$
UPMU	ν_μ	$3.16 \cdot 10^1$	$3.73 \cdot 10^1$	$3.35 \cdot 10^1$
	$\bar{\nu}_\mu$	$3.65 \cdot 10^1$	$4.51 \cdot 10^1$	$4.27 \cdot 10^1$
	$\nu_\mu + \bar{\nu}_\mu$	$3.67 \cdot 10^1$	$3.81 \cdot 10^1$	$3.73 \cdot 10^1$

The second computation that can be performed in the same fashion is by assuming mono-energetic emission, as described in Sec.5.2. The method is the same as above except that $\lambda(E) = \delta(E - E_0)$ and we scan different values of E_0 between 0.1 GeV and 100 TeV .

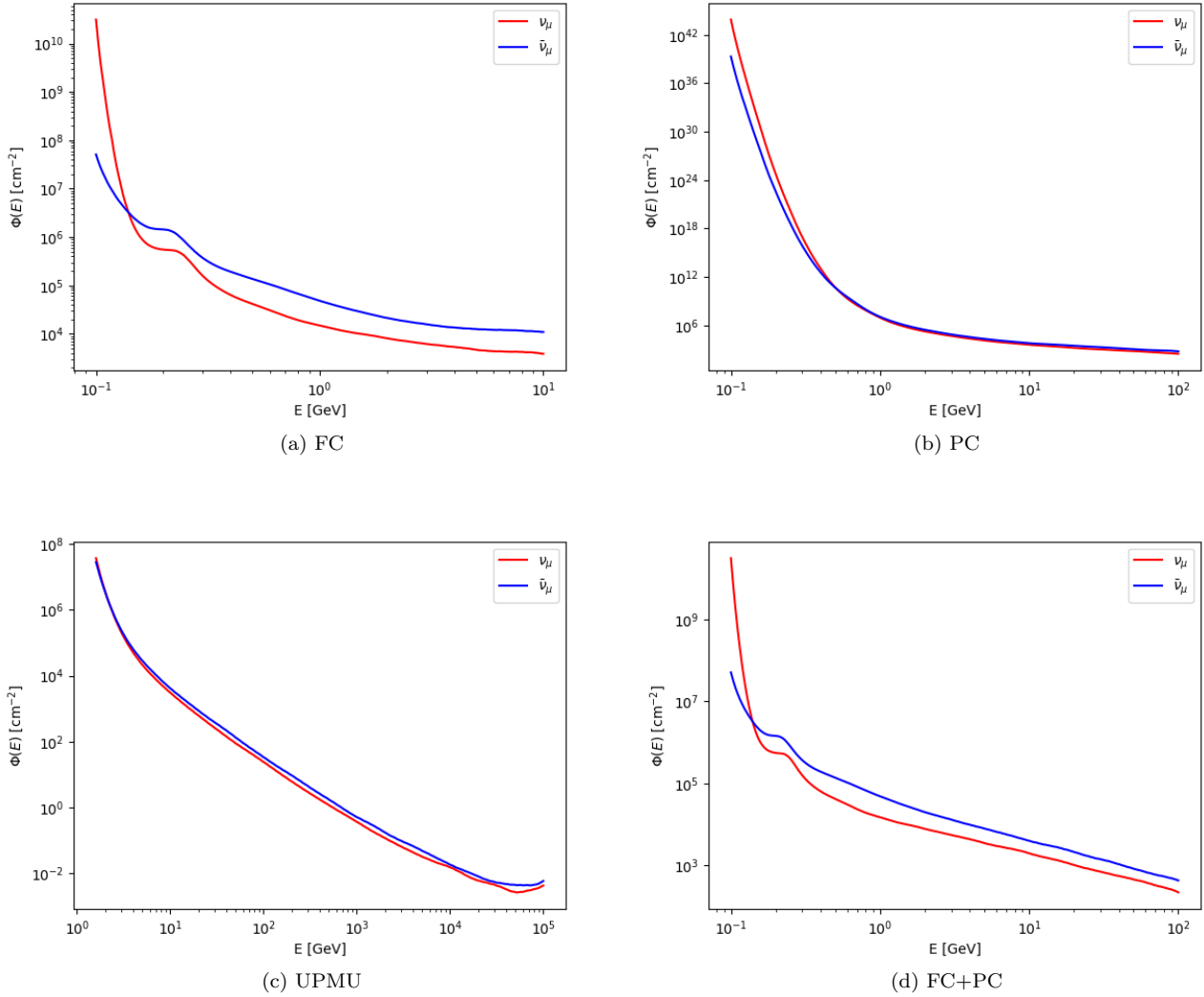


Figure 39: Energy-dependent fluence 90% upper limits for ν_μ and $\bar{\nu}_\mu$ for FC, PC, UPMU and FC+PC.

$$\begin{aligned}
 \Phi_{\text{mono}}(E) &= \frac{N_{90}}{\int dE_\nu A_{\text{eff}}(E_\nu, \theta) \delta(E_\nu - E)} \\
 &= \frac{N_{90}}{A_{\text{eff}}(E, \theta)}
 \end{aligned}
 \tag{38}$$

As this procedure has to be repeated independently for all pixels of the sky map, it is not easy to visualise². In the [Figure 39](#), we show the result of such computation at the best-fit position of S190412m.

Several remarks on the results can be made:

- For FC and PC, the result does not depend very much on the sky position: the skymap is more or less uniform and the results from the [Table 6](#) are similar for average/min/max... This is expected because the efficiency of the selection and the acceptance of Super-Kamiokande does not depend much on event direction³.
- For UPMU, as the sample is only covering the sky below the horizon, we get an “incomplete” flux limits map. It can then happen that some of the numerical applications from [Table 6](#) cannot be done for UPMU, as

²In [\[18\]](#), it was more straightforward as the external trigger was well localised and therefore only one possible position was considered

³This was indeed assumed implicitly in previous analyses where the flux formula was not depending on θ at all

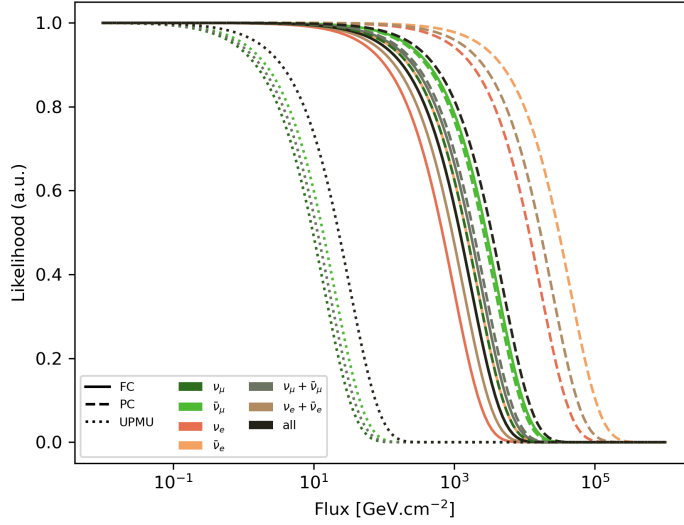


Figure 40: Example of flux likelihood using Equation 39, for the different samples (FC/PC/UPMU) and neutrino flavours.

e.g. the best-fit of the GW contour is above the horizon. In the worst case, if the full GW 90% is above the horizon, the UPMU sample can only be used to constrain the sky-averaged (below the horizon) flux limits, but this quantity is of little relevance as the astrophysical event is most probably located in the “unseen” region.

- The energy-dependent fluence limits are a simple reflection of the effective area as expected from Equation 38.

5.4 Flux limits:sample-by-sample, marginalised

The approach presented in previous section is ideal if the position of the source is known precisely, so that the limit at this position can be computed directly. However, the GW sky localisation are generally quite large.

The first strategy is to simply quote a range of limits covering the full sky localisation by using the values obtained above, while a second strategy consists in marginalising over the localisation to get only one value at the end.

The N_{90} limit in the previous section is obtained by using the Poisson likelihood with $n = N_{\text{obs}}$ and $\lambda = N_{\text{exp}}$. Similarly, we define the following likelihood based on Poisson statistics and weighted by GW localisation probability:

$$\mathcal{L}(\phi_0; n_B, N) = \int \frac{(c(\Omega)\phi_0 + n_B)^N}{N!} e^{-(c(\Omega)\phi_0 + n_B)} \mathcal{P}_{\text{GW}}(\Omega) d\Omega \quad (39)$$

where $c(\Omega)$ is the conversion factor from $E^2 dn/dE$ to number of events (this is the denominator in Equation 37), n_B is the expected background, N is the observed number of events and $\mathcal{P}_{\text{GW}}(\Omega)$ is the GW localisation.

The 90% upper limit is simply obtained by solving:

$$\int_0^{\phi_0^{\text{0,up}}} \mathcal{L}(\phi_0) d\phi_0 = 0.90 \quad (40)$$

assuming \mathcal{L} is correctly normalised. This effectively corresponds to a Bayesian upper limit, with flat prior on ϕ_0 . This has to be repeated independently for each SK sample and neutrino flavour.

The Figure 40 shows an example of likelihood as a function of ϕ_0 and the results for S190412m are presented in Table 6, in comparison with the min-max range computed in the previous section.

It is also possible to compute upper limits on $\nu_\mu + \bar{\nu}_\mu$, $\nu_e + \bar{\nu}_e$ and $\nu_\mu + \bar{\nu}_\mu + \nu_e + \bar{\nu}_e (= \text{ALL})$, assuming equipartition of the incoming flux between the considered flavours.

Conversion from flux to source energy release For each GW event, we have provided upper limits on the detected neutrino flux. However, the true physical quantity is rather the total energy emitted in neutrinos from the source. We often use E_{iso} to refer to this energy, assuming spherical symmetry.

If the position of the source is perfectly known (distance r , sky position Ω), we have:

$$\begin{aligned} \frac{E_{\text{iso}}}{4\pi r^2} &= \int_{E_{\text{min}}}^{E_{\text{max}}} \frac{dn_{\text{tot}}}{dE} E dE \\ &= \phi_{0,\text{tot}} \int_{E_{\text{min}}}^{E_{\text{max}}} E^{-2} E dE \end{aligned} \quad (41)$$

Using this formula, it is easy to convert from previously computed flux limits to limits on E_{iso} . However; the distance to the source has some uncertainty and there are some correlations between distance and angles. It is then needed to use a more sophisticated approach, as it will be described later.

5.5 Combined statistical analysis

We have discussed the observation significant that we compute it by using Poisson distribution. This method is only depended on observed number, But in high-energy region, we have angular-distribution and energy-distribution. To get a more accurate data, we use the follow two method to compute the significance and flux limits.

Here we discuss this following parameter:

- Angular distribution: The neutrino events should cluster around a given direction that is compatible with the GW, with a spread that is related to the detector angular resolution (both due to experimental resolution and to the scattering angle between the neutrino and the outgoing muon).
- Energy distribution: While the background from atmospheric neutrinos have an energy spectrum following approximately a power law $E^{-2.7}$, the signal should have a distinct shape. In the case of simple Fermi acceleration mechanisms, we can expect a power law E^{-2} . In the following, we will assume a generic power law $E^{-\gamma}$.

We want to use our data D in order to distinguish between two hypotheses:

- H_0 : data can be completely described by background atmospheric neutrinos
- H_s : data consists in a superposition of atmospheric neutrinos and astrophysical neutrinos

To do so, we will use as test statistic the following likelihood ratio:

$$\Lambda = 2 \ln \left[\frac{P(D|H_s)}{P(D|H_0)} \right] \quad (42)$$

where $P(D|H_s)$ and $P(D|H_0)$ are the likelihood associated to signal+bkg and bkg hypotheses respectively, using all our present knowledge on angular and energy distributions for both atmospheric background and astrophysical events. This definition of Λ is convenient because large values would correspond to the case where data favours H_s while small values correspond to the case where data favours H_0 .

5.5.1 Lambda method

Likelihood definition In a point-source search, assuming a direction \vec{x}_S , we can build the following likelihood, as it has been done in [22, 2]:

$$\mathcal{L}_\nu(n_S, \gamma; \vec{x}_S) = \frac{e^{-(n_S+n_B)} (n_S + n_B)^N}{N!} \prod_{i=1}^N \frac{n_S \mathcal{S}(\vec{x}_i, E_i; \vec{x}_S, \gamma) + n_B \mathcal{B}(\vec{x}_i, E_i)}{n_S + n_B} \quad (43)$$

where n_S is the number of signal events (variable of interest), \vec{x}_S is the test source direction, γ is the spectral index of the signal ($dn/dE \propto E^{-\gamma}$) the n_B is the expected number of background events, N is the number of observed events in the selected time window centered on GW trigger, the product is over these events (characterised by their direction \vec{x}_i and their energy E_i) and \mathcal{S} (resp. \mathcal{B}) are signal (resp. background) p.d.f. that encodes expected behaviour as a function of energy and direction.

It is possible to rewrite $P(D|H_S)$ and $P(D|H_0)$ using this likelihood and assuming that the signal hypothesis is the one corresponding to $n_S = \widehat{n}_S$ and $\gamma = \widehat{\gamma}$, where \widehat{n}_S and $\widehat{\gamma}$ are the values maximising the likelihood:

$$\begin{aligned} P(D|H_S) &= \mathcal{L}_\nu(\widehat{n}_S, \widehat{\gamma}; \vec{x}_S) \\ P(D|H_0) &= \mathcal{L}_\nu(n_S = 0; \vec{x}_S) \\ \Lambda_\nu(\vec{x}_S) &= 2 \ln \left[\frac{\mathcal{L}_\nu(\widehat{n}_S, \widehat{\gamma}; \vec{x}_S)}{\mathcal{L}_\nu(n_S = 0; \vec{x}_S)} \right] \end{aligned} \quad (44)$$

In the case of Gravitational Wave follow-up analysis, the direction of the test source is not known perfectly, but we rather have a probability density distribution represented by a skymap $w_L(\vec{x}_S)$. We can insert it in the previous formula as an additional weight.

$$\Lambda(\vec{x}_S) = 2 \ln \left[\frac{\mathcal{L}_\nu(\widehat{n}_S, \widehat{\gamma}; \vec{x}_S)}{\mathcal{L}_\nu(n_S = 0; \vec{x}_S)} \right] + 2 \ln w_L(\vec{x}_S) \quad (45)$$

$$= 2 \left[-\widehat{n}_S + \sum_{i=1}^N \ln \left(1 + \frac{\widehat{n}_S S_i}{n_B B_i} \right) \right] + 2 \ln w_L(\vec{x}_S) \quad (46)$$

This procedure can be repeated for every pixels of the GW skymap, effectively scanning all the sky in search for a point-source. We will then use as a test statistic the best fit position in the sky:

$$TS = \max_{\vec{x}_S} [\Lambda(\vec{x}_S)] \quad (47)$$

Signal and background p.d.f. We have used $\mathcal{S}_i = \mathcal{S}(\vec{x}_i, E_i; \vec{x}_S, \gamma)$ and $\mathcal{B}_i = \mathcal{B}(\vec{x}_i, E_i)$ to quantify how likely a given event i is compatible with signal and background. It is trivial that \mathcal{S}_i depends on the characteristics of the source (n_S, γ) while \mathcal{B}_i is independent from them.

To ensure proper mathematical and statistical properties, we should have:

$$\begin{cases} \int \int \mathcal{S}(E, \Omega; \vec{x}_S, \gamma) dE d\Omega = 1 \text{ for all values of } \vec{x}_S, \gamma \\ \int \int \mathcal{B}(E, \Omega) dE d\Omega = 1 \end{cases} \quad (48)$$

where we integrate over the full energy-angle phase-space.

We have already characterised in details how they are both distributed with respect to energy and angle and can therefore define them as it has been done in [13].

For background, assuming angular and energy dependencies are uncorrelated, we can then write:

$$\mathcal{B}(E_i, \vec{x}_i = [\theta, \phi]) = B_{\text{ene}}(E_i) \times B_{\text{ang}}(\theta_i) \quad (49)$$

For signal, the same decomposition can be performed:

$$\mathcal{S}(E_i, \vec{x}_i; \vec{x}_S, \gamma) = S_{\text{ene}} \times S_{\text{ang}} \quad (50)$$

The angular component is directly obtained from the angular resolution,

$$S_{\text{ang}}(\vec{x}_i; E_i, \vec{x}_S) = P(\Delta\Phi = \text{Angle}(x_i^{\text{astro}}, \vec{x}_S); E_i) \quad (51)$$

It is worth noting that the angular component depends on detected neutrino energy and on the test source direction. The notation x_i^{astro} is used to highlight the fact that we should compare the neutrino and the test source direction in the same coordinate system⁴. As the SK standard ROOT files after reduction already contain the direction of each events in equatorial coordinates (α_i, δ_i) , we will use the system by convenience⁵.

Finally the signal energy component is the result of the correlation between the detector energy resolution (see Figure 29) and the assumed signal energy spectrum. More precisely, if we note $F(r = \frac{E_{\text{reco}}}{E_{\text{true}}}; E_{\text{true}})$ the distributions of Figure 29 (we have one such distribution for each value of E_{true}), we can then write:

$$S_{\text{ene}}(E_i; \gamma) = C \times \int F(r = \frac{E_i}{E_\nu}; E_\nu) \times E_\nu^{-\gamma} dE_\nu \quad (52)$$

where C ensures normalisation to unity.

⁴Reminder: we can convert from (θ, ϕ) (or rather altitude-azimuth (a, A)) to (δ, α) (and reverse). If we know the current local sidereal time θ_L

⁵The choice does not matter as the angular distance between two directions is an invariant in the change of coordinate system.

Combination of different samples In the case of High-Energy analyses, we have defined three different and independent samples: FC, PC and UPMU. Of course, these samples will have different angular resolution, energy reconstruction, . . . , we may wonder then how to combine them efficiently. The likelihood from Equation 43 can easily be expressed independently for each sample s :

$$\mathcal{L}_\nu^{(s)}(n_S^{(s)}, \gamma; \vec{x}_S) = \frac{e^{-(n_S^{(s)} + n_B^{(s)})} (n_S^{(s)} + n_B^{(s)})^{N^{(s)}}}{N^{(s)}!} \prod_{i=1}^{N^{(s)}} \frac{n_S^{(s)} \mathcal{S}^{(s)}(\vec{x}_i, E_i; \vec{x}_S, \gamma) + n_B^{(s)} \mathcal{B}^{(s)}(\vec{x}_i, E_i)}{n_S^{(s)} + n_B^{(s)}} \quad (53)$$

where we only consider events in the specified sample s .

We can then simply define a combined Λ where $n_S^{(s)}$ and γ are maximised independently for each sample⁶:

$$\Lambda(\vec{x}_S) = 2 \left[- \sum \widehat{n}_S^{(s)} + \sum_{i=1}^N \ln \left(1 + \frac{\widehat{n}_S^{(s)} \mathcal{S}_i^{(s)}(\dots, \widehat{\gamma}^{(s)})}{n_B^{(s)} \mathcal{B}_i^{(s)}} \right) \right] + 2 \ln w_L \quad (54)$$

where the sum is over all the events.

The test statistic TS is defined as before.

Obtaining p-value In an ideal scenario where both background and signal have a very predictive behaviour, we could simply compute the test statistic for data and compare it to the expected distributions for background and for signal+background.

However, both the strength (n_S) and the shape (γ) are unconstrained parameters⁷. What is fixed, nonetheless, is the background behaviour: we know the event rate, its energy distribution and its angular distribution.

We can then compute a p-value, which quantifies how likely the observation is compatible with the background-only hypothesis. For a given gravitational wave event, this can be obtained in two steps:

1. Compute TS background distribution using randomised neutrinos (random energy, direction and time) and the fixed GW sky map $\Rightarrow P_{\text{bkg}}(TS)$
2. Compute the observed TS_{data} and compare to the background distribution:

$$p = \int_{TS_{\text{data}}}^{\infty} P_{\text{bkg}}(TS) dTS \quad (55)$$

This procedure is repeated independently for all the GW events. In the case where data are completely compatible with background-only hypothesis, the distribution of the p-values between 0 and 1 should be uniform. If there is some signal evidence, there should be an excess toward $p = 0$.

To handle with the combination of the different samples, the distribution $P_{\text{bkg}}(TS)$ is simply obtained using randomised neutrinos with representative proportions of the different samples.

The zero event toys One particular issue has to be taken care of: the background event rate in SK is relatively small, such that in any given 1000 s time window, only 0.14 events are expected. This rises a $P_0 \sim 87\%$ probability to observe no event. In such case, it is irrelevant to compute signal significance, as we would always obtain $TS = \max_{\vec{x}_S} 2 \ln [w_L(\vec{x}_S)] \equiv \kappa$.

Nevertheless, these scenarii should in principle affect $P_{\text{bkg}}(TS)$: when doing background toys to estimate $P_{\text{bkg}}(TS)$, 87% of the toys would have no event and therefore $P_{\text{bkg}}(TS)$ would have a big peak containing 87% of the probability at $TS = \kappa$. Then, when computing the p-value for a given GW follow-up, there are two possibilities:

- if there are no SK events in the 1000 s time window, we have $TS_{\text{data}} = \kappa$ and $p = 100\%$
- if there are some SK events in the 1000 s time window, we have $TS_{\text{data}} > \kappa$ and $p < 1 - P_0\%$ (as we are surely located after the peak containing P_0 of $P_{\text{bkg}}(TS)$ integral)

⁶In principle, there is no need to maximise γ independently if the spectrum follows an unique power-law $E^{-\gamma}$, but doing so allow to handle the possibility e.g. that FC sample sees a different spectrum than UPMU sample between they have different energy ranges.

⁷Even if we had a perfect modelling of all astrophysical sources, they would depend on the distance to the source and the type of the source.

This leaves a big unfilled gap of values between $1 - P_0$ and 1, that has no physical meaning.

However, we can get rid of this situation by simply changing point of view: as stated before, it only makes sense to compute the p-value in the case where we have detected some events in Super-Kamiokande. Then, what we really need is the probability for the observation to be compatible with background **given that we have at least one event in time coincidence**. Effectively, it is equivalent to the suppression of zero event toys in $P_{\text{bkg}}(TS)$ distribution.

Then, the p-value will be distributed between 0 and 1 continuously, as expected and if an observation is fully inconsistent (resp. consistent) with the signal direction, we will get p close to 1 (resp. 0).

The additional interesting feature is that, if one wants to obtain the p-value taking into account the zero background toys (i.e. the fact that observing at least one event in time coincidence is already quite “rare”), one can simply multiply the above p-value by $1 - P_0$ (for a simple order of magnitude, let’s say divide by a factor 10), that would effectively reintroduce the zero event toys in the game.

Example of application Before presenting the general implementation of the analysis, let’s discuss one specific example: S190513bm.

Results for this particular event have already been presented in [section 4.2.4](#). The most important piece of information is presented in [Figure 31](#): there was one SK event (in FC sample), with a reconstructed energy of 0.68 GeV and with a reconstructed direction close to the GW contour.

For every pixel of the sky, we compute Λ using [Equation 54](#). We obtain [Figure 41](#).

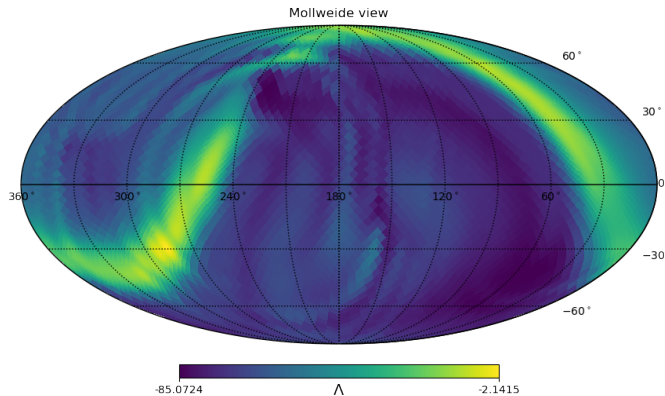


Figure 41: Lambda map for S190513bm.

The final value of the test statistic correspond to the maximum value of above map: $TS_{\text{data}} \sim -2.1415$.

Using the rates from [Table 1](#), we throw randomly the number of observed events in FC/PC/UPMU (with the constraint that $N_{\text{FC}} + N_{\text{PC}} + N_{\text{UPMU}} > 0$). For each event, its energy and direction are chosen randomly from the expected background distribution obtained from SK4 MC⁸.

After throwing $\sim 50\text{k}$ toys, we can plot the distribution presented in [Figure 42](#). From this, we can easily extract the p-value by comparing it with TS_{data} .

We obtain $p = 4.8\%$. This should only be interpreted in frequentist fashion: if there is truly no signal and if we were able to reproduce the same conditions (same detector status, same GW localisation) N times, 4.8% of such hypothetical experiments would have a test statistic at least as high as the one from real data.

Final results For reference, the [Table 7](#) shows the results for all gravitational waves from April 2019 to March 2020 in real-time, with a SK event detected in the 1000s time window.

We see some minor disagreements between the two methods, which are simply due to statistical fluctuations and precision loss in the operations.

5.5.2 Chi-square method

As a cross-check, it can be interesting to consider a second approach, with a different method to obtain a p-value. We will follow the method presented in [\[10\]](#).

⁸This could be performed using data directly.

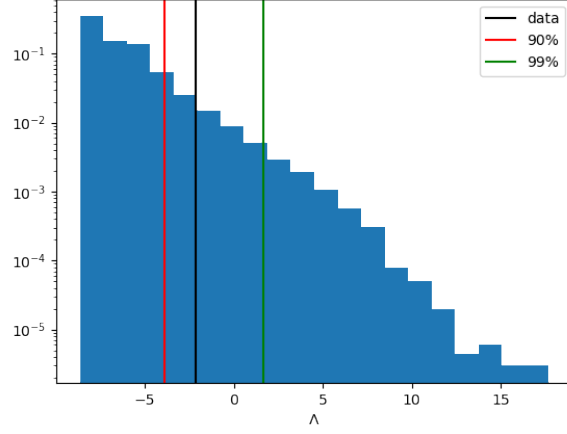


Figure 42: Background TS distribution for S190513bm.

Table 7: Results of the likelihood statistical analysis for all gravitational waves from April 2019 to March 2020 with a SK event detected in the 1000s time window. We remind the date/time of the event, the number of detected events in the different samples. Two set of p-values are provided: p_{old} corresponds to the one without using the pre-computation trick (where we take the time to do the full computation from scratch); $p_{\text{pre.}}$ is obtained using the pre-computation trick.

Trigger	Date/time	$N_{\text{obs}}^{\text{FC}}$	$N_{\text{obs}}^{\text{PC}}$	$N_{\text{obs}}^{\text{UPMU}}$	p_{old} (%)	$p_{\text{pre.}}$ (%)
S190426c	2019-04-26 15:21:55	0	0	1	100.0	100.0
S190513bm	2019-05-13 20:54:28	1	0	0	5.2	4.9
S190602aq	2019-06-02 17:59:27	1	0	0	2.5	2.6
S190728q	2019-07-28 06:45:10	1	0	0	17.0	17.9
S190814bv	2019-08-14 21:10:39	1	0	0	100.0	100.0
S190924h	2019-09-24 02:18:46	1	0	0	53.2	51.5
S191213g	2019-12-13 04:34:08	1	0	0	16.0	15.4
S200316bj	2020-03-16 21:57:56	0	0	1	57.4	56.1

First, we define the likelihood:

$$\mathcal{L} = \int L(\vec{x}_S) d\vec{x}_S \quad (56)$$

$$\text{with } L(\vec{x}_S) = \frac{S_{GW}(\vec{x}_S) \prod_j S_\nu^j(\vec{x}_j, \vec{x}_S; E_i)}{B_{GW}(\vec{x}_S) \prod_j B_\nu^j(\vec{x}_j, \vec{x}_S)} \quad (57)$$

where the products is over all SK events in the 1000s time window and the S_X / B_X are normalised to unity (when integrating over the full sky) and are respectively characterising signal and background angular distribution for the component X .

More precisely, S_ν^j is defined in the same way as in Equation 51 and B_ν^j is defined as being the angular component from Equation 49. $S_{GW}(\vec{x}_s)$ is the GW probability distribution from LIGO-Virgo and $B_{GW}(\vec{x}_s) = 1/(4\pi)$.

From this likelihood, we can directly define a p-value that is covering only the possible angular correlations between neutrinos and the gravitational wave:

$$p_{\text{sky}} = \int_{\mathcal{L}_{\text{data}}}^{\infty} P_{\text{bkg}}(\mathcal{L}') d\mathcal{L}' \quad (58)$$

where $P_{\text{bkg}}(\mathcal{L}')$ is the distribution of likelihood obtained with a sample of $\mathcal{O}(100)$ k background toys. This is obtained in the same way as for the Λ method, with the exact same consideration of removing the toys with zero event in the time window.

We then define several p-values that will cover different points:

- $p_{\text{GW}} = 1 - \text{Poisson}(0, T \cdot \text{FAR})$ is the probability for such a GW event to raise from background. FAR is the false alarm rate of the given event and T is the considered coincidence time window.
- $p_\nu^{(j)} = \int_{E_j}^{\infty} P_{\text{bkg}}(E') dE'$ is the p-value obtained by comparing reconstructed neutrino event energy with the background distribution.
- $p_{\text{cluster}} = 1 - \sum_{i=0}^{N-2} \text{Poisson}(i, n_B)$, where n_B is the expected number of background events. This will favour the case where more than 1 event are detected in the time window ($p_{\text{cluster}} = 1$ if $N = 1$).

The different p-values are then combined in a joint χ^2 :

$$\chi_{\text{data}}^2 = -2 \ln \left[p_{\text{sky}} \times p_{\text{GW}} \times \prod_j p_\nu^{(j)} \times p_{\text{cluster}} \right] \quad (59)$$

From this new test statistic, we can compute the final p-value:

$$p = \int_{\chi_{\text{data}}^2}^{\infty} P_{\text{bkg}}(\chi^2) d\chi^2 \quad (60)$$

In [10], the background distribution $P_{\text{bkg}}(\chi^2)$ is obtained using time-scrambled neutrino data **and** time-scrambled GW data. As the goal here is to do a cross-check with the previously described Λ method, with a given GW event, in the following, we will consider the GW event fixed, even for the background estimation. Therefore, FAR will always have the same issue, so that we can remove p_{GW} from the Equation 59.

Combination of different samples As for the previous method, we may wonder how to combine FC, PC and UPMU efficiently. Here, it is quite straightforward that we can consider all the events from the different samples (with their different p.d.f.) together in Equation 57 and $n_B = \sum_s n_B^{(s)}$ for p_{cluster} .

Example of application Let's consider again S190513bm. The Figure 43 shows the background distribution and the value for data of the likelihood from Equation 57, while the Figure 44 shows the background distribution and the value for data of χ^2 .

We have $\mathcal{L}_{\text{data}} = 2.17$ and $\chi_{\text{data}}^2 = 62.66$. From the background distributions, we directly obtain the final p-value: 12.9%

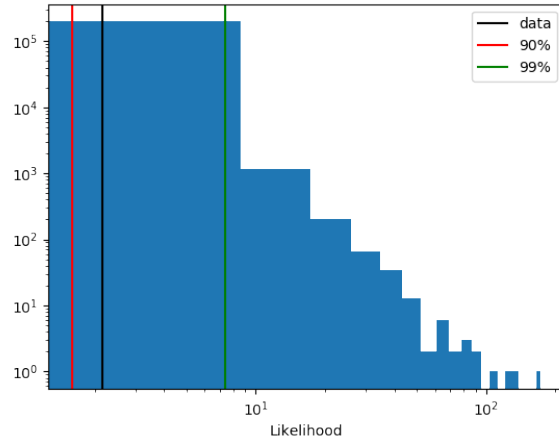


Figure 43: Background likelihood distribution compared to the value obtained for data for S190513bm.

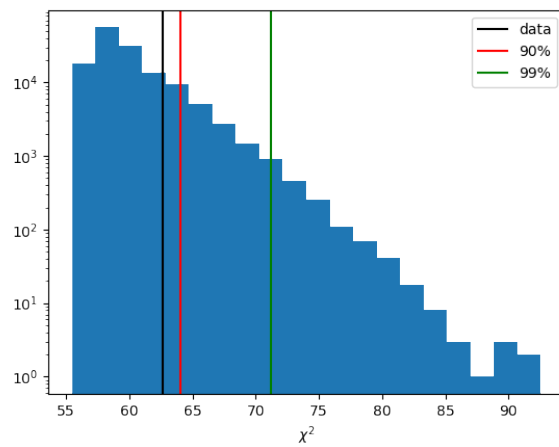


Figure 44: Background χ^2 distribution compared to the value obtained for data for S190513bm.

5.6 Flux limits: combined

5.6.1 Signal simulation

In order to compute flux limits, we will need to be able to simulate neutrino signal events from a given source direction. Fortunately, we already have most of the needed ingredients.

We have defined how signal and background are distributed with energy and angles. We can use this to do simulations.

For a given sample and neutrino flavour, we can generate a signal event by applying the following procedure:

1. generate E_{true} following $A_{\text{eff}}(E, \theta) \times \lambda(E)$
2. obtain E_{reco} by generating $r = \frac{E_{\text{reco}}}{E_{\text{true}}}$ following $F(r; E_\nu)$ (already used in [Equation 52](#))
3. generate the angular distance $\Delta\Phi$ between true neutrino direction (α, δ) and reconstructed direction, following the angular resolution p.d.f. $P(\Delta\Phi; E_i)$ (already used in [Equation 51](#))
4. generate the actual reconstructed direction randomly on the circle of center (α, δ) and of radius $\Delta\Phi$

For the combined analysis (combining the samples), every event is assigned randomly to a SK sample based on the relative weights:

$$\int A_{\text{eff}}(s, f)(E, \theta) \times \lambda(E) dE \text{ for } s \in \{FC, PC, UPMU\} \quad (61)$$

In the case of combining flavours, e.g. $\nu_\mu + \bar{\nu}_\mu$, the flavours is also assigned randomly to the event by using similar weights.

5.6.2 Marginalised limits

A second approach using the test statistic (Λ method) has been implemented. It follows the procedure described in [\[31\]](#). Instead of computing flux limits for each direction of the sky, the direction is marginalised by defining the flux likelihood:

$$\mathcal{L}(\phi_0; TS_{\text{data}}, \mathcal{P}_{GW}) = \int \sum_{k=0}^2 \left[\frac{(c(\Omega)\phi_0)^k}{k} \exp(-c(\Omega)\phi_0) \times P_k(TS_{\text{data}}) \right] \times \mathcal{P}_{GW}(\Omega) d\Omega \quad (62)$$

where $c(\Omega)$ is the conversion factor from ϕ_0 to the expected number of signal events in SK, $P_k(TS)$ is the test statistic distribution for k injected signal events, simulated using the strategy described in [section 5.6.1](#)), TS_{data} is the measured test statistic and $\mathcal{P}_{GW}(\Omega)$ is the GW skymap provided by LIGO-Virgo.

The [Figure 45](#) shows the distributions $P_i(TS)$ ($i = 0, 1, 2$) for the simulation of ν_μ events. From these normalised distribution, we can extract $P_i(TS_{\text{data}})$.

One example of $\mathcal{L}(\phi_0; TS_{\text{data}}, \mathcal{P}_{GW})$ for S190408an is shown in [Figure 46](#).

$\phi_0 = E^2 dn/dE$ limits are simply obtained by solving:

$$\int_0^{[\phi_0]_{90}} \mathcal{L}(\phi_0) \times d\phi_0 = 0.90 \int_0^\infty \mathcal{L}(\phi_0) \times d\phi_0 \quad (63)$$

The example of S190408an and S190412m is presented in [Table 8](#).

Table 8: Computation of the limits on $\phi_0 = E^2 \frac{dn}{dE}$ for S190408an and S190412m [in $\text{GeV} \cdot \text{cm}^{-2}$], obtained using the combined method compared with the sample-by-sample results.

Trigger	Flavour	FC	PC	UPMU	Combined
S190408an	ν_μ	$4.00 \cdot 10^3$	$5.16 \cdot 10^3$	$2.47 \cdot 10^5$	$2.27 \cdot 10^3$
	$\bar{\nu}_\mu$	$9.19 \cdot 10^3$	$8.94 \cdot 10^3$	$7.48 \cdot 10^5$	$4.53 \cdot 10^3$
S190412m	ν_μ	$3.97 \cdot 10^3$	$4.86 \cdot 10^3$	$3.35 \cdot 10^1$	$3.38 \cdot 10^1$
	$\bar{\nu}_\mu$	$9.45 \cdot 10^3$	$8.44 \cdot 10^3$	$4.27 \cdot 10^1$	$4.31 \cdot 10^1$

We can see that the marginalised results is consistent with the min-max range, but it has the advantage of consisting in one value instead of two

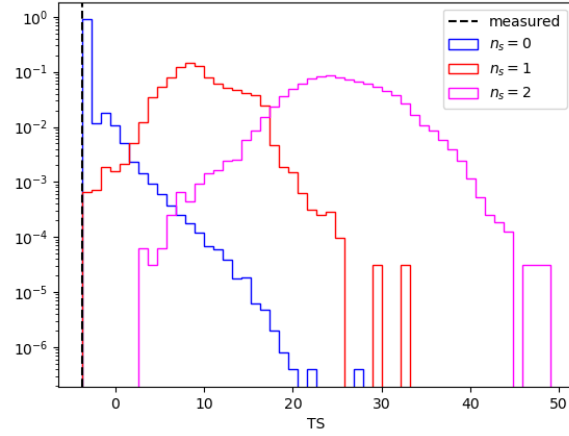


Figure 45: Test statistic distribution for $n_S = 0$ (only background), $n_S = 1$ (background + 1 ν_μ signal events), $n_S = 2$ (background + 2 ν_μ signal events).

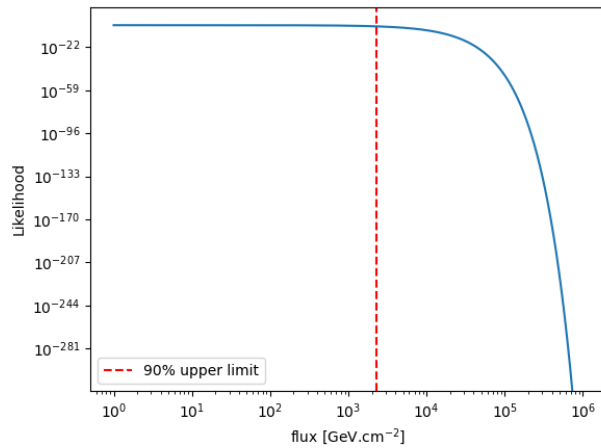


Figure 46: Flux likelihood after marginalising over the sky, for S190408an.

5.7 Isotropic total neutrino energy limits

5.7.1 High Energy sample

Individual upper limits The physical quantity of interest is the total energy emitted in neutrinos by the source (correcting by distance), assuming isotropy. We can use the same method than for flux limits presented in [section 5.6](#) but using the 3D skymap (r in Mpc) $\mathcal{V}_{GW}(r, \Omega)$ as in [\[31\]](#):

$$\mathcal{L}(E_{\text{iso}}) = \int \sum_{k=0}^2 \left[\frac{(c'(r, \Omega) E_{\text{iso}})^k}{k!} e^{-c'(r, \Omega) E_{\text{iso}}} \times P_k(TS_m) \right] \mathcal{V}_{GW}(r, \Omega) r^2 dr d\Omega \quad (64)$$

where $c'(r, \Omega)$ is the factor to convert E_{iso} to number of signal events (combining all the samples) for known source position Ω and distance r .

Upper limit $E_{\text{iso}}^{\text{up}}$ is obtained by using:

$$\int_0^{E_{\text{iso}}^{\text{up}}} \mathcal{L}(E_{\text{iso}}) dE_{\text{iso}} = 0.90 \quad (65)$$

assuming the likelihood is correctly normalised.

For a given neutrino flavour, we can then get an upper limit on the energy in neutrinos that would be detected as this particular flavour at Earth. For instance, using ν_μ , this allows to put a limit on $E_{\text{iso}}^{\nu_\mu}$.

In order to extrapolate to the total energy emitted in neutrinos by the source, we can assume equipartition on Earth, i.e. $\nu_e : \nu_\mu : \nu_\tau : \bar{\nu}_e : \bar{\nu}_\mu : \bar{\nu}_\tau = 1 : 1 : 1 : 1 : 1 : 1$. This assumption is reasonable is the main production channel for neutrinos is pion decay in the astrophysical source vicinity.

In the case of the example above, we can extrapolate as $E_{\text{iso}}^{\text{all}} = 6 \times E_{\text{iso}}^{\nu_\mu}$.

If the likelihood of [Equation 64](#) is computed for $\nu_\mu + \bar{\nu}_\mu$, one can constrain jointly the two flavours and can extrapolate to total energy: $E_{\text{iso}}^{\text{all}} = 3 \times E_{\text{iso}}^{\nu_\mu + \bar{\nu}_\mu}$. The situation is similar for $\nu_e + \bar{\nu}_e$. Finally, if all flavour are considered together, i.e. $\nu_\mu + \bar{\nu}_\mu + \nu_e + \bar{\nu}_e$, we get $E_{\text{iso}}^{\text{all}} = 3/2 \times E_{\text{iso}}^{\nu_\mu + \bar{\nu}_\mu + \nu_e + \bar{\nu}_e}$.

The [Table 9](#) summarises the results for GW190521. As the flux limits for ν_e and $\bar{\nu}_e$ are dominated by FC and are much less stringent than ν_μ and $\bar{\nu}_\mu$ limits, the final $E_{\text{iso}}^{\text{all}}$ are dominated by muon limits and $E_{\text{iso}}^{\text{all, up}} \sim 3 \times E_{\text{iso}}^{\nu_\mu + \bar{\nu}_\mu, \text{up}}$.

Table 9: Example of summary of flux and E_{iso} limits, for the different samples and flavours.

Name	Sample	ν_μ (ν_x)	$\bar{\nu}_\mu$ ($\bar{\nu}_x$)	ν_e	$\bar{\nu}_e$
GW190521	FC	$3.96 \cdot 10^3$	$9.60 \cdot 10^3$	$2.28 \cdot 10^3$	$4.71 \cdot 10^3$
	PC	$4.89 \cdot 10^3$	$8.35 \cdot 10^3$	$3.99 \cdot 10^4$	$1.02 \cdot 10^5$
	UPMU	$4.24 \cdot 10^1$	$4.96 \cdot 10^1$	-	-
	Combined	$3.73 \cdot 10^1$	$4.93 \cdot 10^1$	$2.21 \cdot 10^3$	$4.60 \cdot 10^3$
HE E_{iso}	Per-flavour	$2.61 \cdot 10^{57}$	$3.70 \cdot 10^{57}$	$1.70 \cdot 10^{59}$	$3.43 \cdot 10^{59}$
	$\nu + \bar{\nu}$	$3.22 \cdot 10^{57}$		$2.26 \cdot 10^{59}$	
	All	$9.30 \cdot 10^{57}$			

5.7.2 Low Energy sample

As High-Energy sample, the E_{iso} can be defined as

$$E_{\text{iso}}/(4\pi d^2) = \int_{E_{\text{min}}}^{E_{\text{max}}} \Phi_{\text{lowe}} \times \lambda(E) \times E dE = \Phi_{\text{lowe}} \int_{E_{\text{min}}}^{E_{\text{max}}} \lambda(E) \times E dE \quad (66)$$

In Low-energy cases, we assume the energy spectrum as Fermi-Dirac spectrum. That we can get $\lambda(E) = \lambda(FD)$. And compute E_{iso} like:

$$E_{\text{iso}}/(4\pi d^2) = \int_0^{100} \Phi_{\text{lowe}}^{\text{total}} \times \lambda(FD) \times E dE \quad (67)$$

We know that the Fermi-Dirac distribution is $\frac{cE^2}{e^{\frac{E}{E_{\text{ave}}(20)/3.15}} + 1}$ (here we assume the average energy is 20 MeV)

)and we can get :

$$E_{\text{iso}} = (4\pi d^2) \times \int_0^{100} \Phi_{\text{lowe}}^{\text{total}} \times \frac{CE^2}{e^{\frac{E}{3.15}} + 1} \times EdE \quad (68)$$

where C is Integral constant. As we discussed in High energy , the Fluence-limit of all flavor can be 6 times one flavor(In low energy cases , the most of neutrino is anti-election neutrino,So here we use $6 \times \Phi(\bar{\nu}_e)$)

Limit with likelihood Here we compute the isotropic with a simple method.Like the High-Energy, here we must consider the distance uncertainty.So we must consider it with a likelihood. Here we use Poisson likelihood that:

$$\mathcal{L}(N_{\text{sig}}; N_{\text{obs}}, N_{\text{bkg}}) = \frac{(N_{\text{bkg}} + N_{\text{sig}})_{\text{obs}}^N}{N_{\text{obs}}!} e^{-(N_{\text{bkg}} + N_{\text{sig}})} \quad (69)$$

And we can get the likelihood with limit is:

$$\mathcal{L}(\Phi; N_{\text{obs}}, N_{\text{bkg}}) = \frac{(N_{\text{bkg}} + C\Phi)_{\text{obs}}^N}{N_{\text{obs}}!} e^{-(N_{\text{bkg}} + C\Phi)} \quad (70)$$

where C is the conversion from fluence to N_{sig} : $C = \int A_{\text{eff}}(E)\lambda(E)dE$

We can get Likelihood with E_{iso} for known distance d is :

$$\mathcal{L}(E_{\text{iso}}; N_{\text{obs}}, N_{\text{bkg}}) = \frac{(N_{\text{bkg}} + C'/d^2 \times E_{\text{iso}})_{\text{obs}}^N}{N_{\text{obs}}!} e^{-(N_{\text{bkg}} + C'/d^2 \times E_{\text{iso}})} \quad (71)$$

where C' is the conversion from E_{iso} at 1 Mpc to N_{sig} : $C' = \frac{1}{4\pi d^2 \int E\lambda(E)dE} \times C = \frac{\int A_{\text{eff}}(E)\lambda(E)dE}{4\pi(1\text{Mpc})^2 \int E\lambda(E)dE}$

And likelihood with distance error can be :

$$\mathcal{L}(E_{\text{iso}}; N_{\text{obs}}, N_{\text{bkg}}) = \int_0^\infty \frac{(N_{\text{bkg}} + C'/r^2 \times E_{\text{iso}})_{\text{obs}}^{N_{\text{obs}}}}{N_{\text{obs}}!} e^{-(N_{\text{bkg}} + C'/r^2 \times E_{\text{iso}})} \times P(r)dr \quad (72)$$

where $P(r) \propto \exp\left[-\frac{(r - d_{\text{mean}})^2}{2\sigma_d^2}\right]$ for $r \geq 0$

So we can get the final Function: $\int F(E_{\text{iso}}, r) \times P(r)dr = \sum_i F(E_{\text{iso}}, r_i)$, where r_i are randomly thrown following the gaussian distribution.

The [Table 10](#) summarises the results for *GW190408.181802*,*GW190424.180648*.

Table 10: Example of Low energy summary Fluence , E_{iso} limits, for the different samples and flavours.

Name	Obs	Type	Fluence limit(Fermi-Dirac)	E_{iso}	$E_{\text{iso}}(\text{DistanceError})$
<i>GW190408.181802</i>	3	ν_e	$6.9 \cdot 10^9$	$6.7 \cdot 10^{61}$	$9.5 \cdot 10^{61}$
		$\bar{\nu}_e$	$1.7 \cdot 10^8$	$1.6 \cdot 10^{60}$	$2.3 \cdot 10^{60}$
		ν_x	$4.3 \cdot 10^{10}$	$4.2 \cdot 10^{62}$	$5.9 \cdot 10^{62}$
		$\bar{\nu}_x$	$5.0 \cdot 10^{10}$	$4.9 \cdot 10^{62}$	$7.0 \cdot 10^{62}$
		<i>Combine</i>	$9.7 \cdot 10^8$	$9.5 \cdot 10^{62}$	$1.3 \cdot 10^{61}$
<i>GW190412.180648</i>	1	ν_e	$3.9 \cdot 10^9$	$1.1 \cdot 10^{62}$	$2.0 \cdot 10^{62}$
		$\bar{\nu}_e$	$9.6 \cdot 10^7$	$2.6 \cdot 10^{60}$	$4.7 \cdot 10^{60}$
		ν_x	$2.4 \cdot 10^{10}$	$6.5 \cdot 10^{62}$	$1.3 \cdot 10^{63}$
		$\bar{\nu}_x$	$2.9 \cdot 10^8$	$7.7 \cdot 10^{62}$	$1.4 \cdot 10^{63}$
		<i>Combine</i>	$5.5 \cdot 10^8$	$1.5 \cdot 10^{61}$	$2.9 \cdot 10^{61}$

6 Result merger and result database

6.1 Inventory of different results

Let's detail all the outputs from the different part of the analysis. In each case, the basic information are stored in a `csv` file, in the form of a dictionary. Some additional information are stored as plot in `png` format or as list in `dat` files.

6.1.1 Alert receiver

The basic information from the GW event is obtained from the GCN notice file (`xml` format):

- `ALERT_FILE`: path to the alert file
- `ALERT_NATURE`: nature of the alert ("GW")
- `NOTICE_TYPE`: type of the GCN notice ("Preliminary", "Initial", "Update")
- `NOTICE_UTC`: date and time of the GCN notice (datetime object)
- `TRIGGER_NAME`: name of the trigger (e.g. S190513bm)
- `TRIGGER_UTC`: date and time of the trigger (datetime object)
- `TRIGGER_DATE`: date of the trigger (string object)
- `TRIGGER_TIME`: time of the trigger (string object)
- `TRIGGER_JD`: Julian date of the trigger
- `GW_DISTANCE`: best-fit distance to the Gravitational Wave (in Mpc)

6.1.2 High Energy analysis

The basic information are coming from `atmpd_results.csv` file (one created for each GW follow-up). For simplicity, there is some redundancy and complementarity with the data from Sec.6.1.1.

- `ALERT_FILE`: path to the alert file
- `GW_TYPE`: type of GW event (BBH, NSBH, BNS...)
- `GW_SKYMAP`: path to the skymap file
- `GW_SKYAREA`: area of the 90% contour (in %)
- `TIMEWINDOW`: size of the used time window (in seconds)
- `SK_LIVETIME`: livetime of the SK detector (in seconds)
- `SK_RUNS`: list of runs and subruns covering the time window (with start time + livetime + overlap with the time window, see Sec.4.2.2)
- `SK_SAMPLE_OBS`⁹: observed number of events in the sample
- `SK_SAMPLE_EXP`: expected number of background events in the sample
- `SK_UPMU_SKYCOV`: which fraction of the GW probability is covered by upgoing sky (altitude < 0)
- `SK_UPMU_SKYCOV_90`: which fraction of the 90% GW contour is covered by upgoing sky (altitude < 0)
- `SK_PVALUE`: what is the p-value obtained by simple Poisson counting as described in Sec.5.2

⁹In the following, `SAMPLE` will already refer to either FC or PC or UPMU or FCPC, variables with this notation are defined for the 4 samples.

All the flux limits are also provided in terms of float values, for the different samples (FC, PC, UPMU, combined) and different neutrino flavours (ν_μ , $\bar{\nu}_\mu$, ν_e , $\bar{\nu}_e$ and combining flavours $\nu_\mu + \bar{\nu}_\mu$, $\nu_e + \bar{\nu}_e$, $\nu_\mu + \bar{\nu}_\mu + \nu_e + \bar{\nu}_e$).

Additional data are provided in the form of additional files:

- `atmpd_events.csv`: list of events in the time window (with their respective sample, time, energy, position...)
- `atmpd_time.png`: plot of the time distribution of events in the time window
- `atmpd_skymap.png`: skymap distribution of events in the time window, on top of the GW probability
- `skymap_SK_coverage.png`: skymap showing the part of the sky covered by UPMU sample (altitude < 0)
- event displays: one for each selected SK events
- flux limit plots: one for each sample and neutrino flavour

Finally all the outputs from statistical analysis (only relevant if at least one event is observed) are provided through a set of variables and plots:

- `SK_PVALUE_Lambda`: p-value from Lambda method
- `SK_PVALUE_Chi2`: p-value from chi-square method
- `Lambda_lambdaData.png` and `Lambda_lambdaBkg.png`: plots like in and
- `Chi2_chi2Bkg.png`: plot like in

6.1.3 Low Energy analysis

The basic information are coming from one `csv` file (one created for each GW follow-up). When imported, the names are modified in order to match above naming conventions

- `NUMBER_OF_OBSERVED_EVENTS` → `SK_LOWE_OBS`: number of observed events
- `BACKGROUND_RECENT` and `BACKGROUND_CONTS`: expected background from LOWE (respectively estimated using recent data and using average value)
- `BACKGROUND_USED` → `SK_LOWE_EXP`: expected number of background events, as explained in lowe section
- `N90` → `SK_LOWE_UP`: 90% upper limit on the number of signal events

In addition:

- `event_*.dat`: list of events with time and energy
- `plot_*.pdf`: plot of Δt vs energy for selected events

6.2 Output processing

When a new gravitational wave alert is received, the result merger code is triggered, waiting for High energy and Low energy results, as presented in [Figure 47](#).

There are two possible outcomes:

- while we are waiting for High Energy/LOWE results, the GW event is retracted by LIGO-Virgo: we can give up waiting for High Energy/LOWE (in parallel, both analyses are stopped as well)
- if there is no retraction, where High Energy and LOWE results are available, we process them

The diagram in [Figure 48](#) is showing the general flow of the result merger script, with its main tasks: collect the results from the different branches (GCN receiver, High Energy, LOWE) ; merge them in the results database ; broadcast the results in different formats (more explanations in the next section).

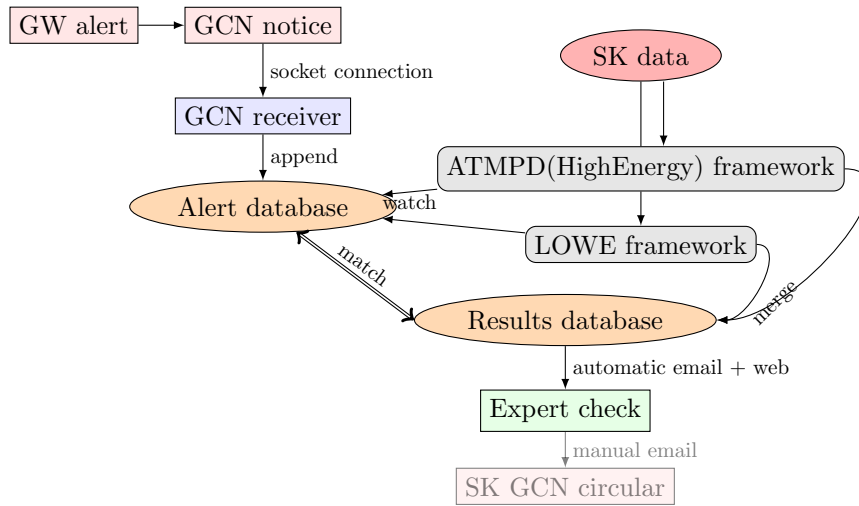


Figure 47: Overview of the general framework

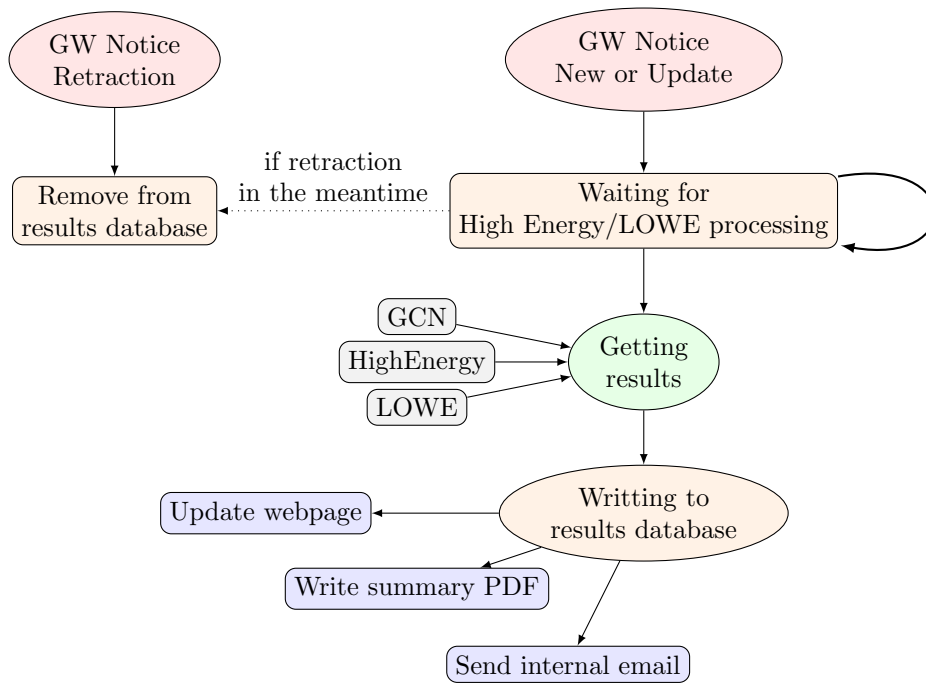


Figure 48: Flow chart of the result merger process

6.3 Output formats

6.3.1 Results database

The different variables described in section 6.1 are stored in the results database, created and updated using `pandas`. The `csv` format is used for storing the database. The plots and additional data files are stored in a dedicated folder (one for each GW trigger).

6.3.2 Web page

The panda database is also exported as HTML format.

The Figure 49 shows a screenshot of the page.

TRIGGER_NAME	Type	Trig.date	Trig.time	GW type	GW 90%	Distance	Livetime	LOWE obs	LOWE bkg	FC obs	FC bkg	PC obs	PC bkg	UPMU obs	UPMU bkg	p-value1	p-value2	PDF
S190408an	Initial	2019-04-08	18:18:02.288180	BBH (100.0%)	386 deg ²	1472.9±357.9 Mpc	993.12 s	3	0.729	0	0.110	0	0.007	0	0.021			Link
S190412m	Initial	2019-04-12	05:30:44.165622	BBH (100.0%)	157 deg ²	812.2±194.1 Mpc	993.13 s	0	0.729	0	0.110	0	0.007	0	0.021			Link
S190421ar	Update	2019-04-21	21:38:56.250977	BBH (96.7%)	1443 deg ²	1628.4±534.6 Mpc	993.08 s	2	0.729	0	0.110	0	0.007	0	0.021			Link
S190425z	Update	2019-04-25	08:18:05.017147	BNS (99.9%)	7461 deg ²	156.1±41.4 Mpc	993.39 s	1	0.729	0	0.110	0	0.007	0	0.021			Link
S190426c	Update	2019-04-26	15:21:55.336540	BNS (49.3%)	1131 deg ²	376.7±100.4 Mpc	992.56 s	0	0.729	0	0.110	0	0.007	1	0.021	100.00%	51.21%	Link
S190503bf	Initial	2019-05-03	18:54:04.294490	BBH (96.3%)	448 deg ²	421.1±104.5 Mpc	993.19 s	0	0.729	0	0.110	0	0.007	0	0.021			Link
S190510g	Update	2019-05-10	02:59:39.291636	Terrestrial (58.0%)	1166 deg ²	227.2±92.4 Mpc	DOWN	-1	-1.000									NaN
S190512at	Update	2019-05-12	18:07:14.422363	BBH (99.0%)	252 deg ²	1387.7±322.1 Mpc	993.67 s	0	0.729	0	0.110	0	0.007	0	0.021			Link
S190513bm	Initial	2019-05-13	20:54:28.747089	BBH (94.3%)	691 deg ²	1987.0±501.2 Mpc	993.57 s	0	0.729	1	0.110	0	0.007	0	0.021	4.85%	15.48%	Link
S190517h	Initial	2019-05-17	05:51:01.830582	BBH (98.3%)	939 deg ²	2950.0±1037.8 Mpc	DOWN	0	3.429									NaN
S190519bj	Initial	2019-05-19	15:35:44.397949	BBH (95.6%)	967 deg ²	3153.5±791.0 Mpc	993.71 s	1	0.729	0	0.110	0	0.007	0	0.021			Link
S190521g	Update	2019-05-21	03:02:29.447266	BBH (96.6%)	765 deg ²	3931.4±953.0 Mpc	994.01 s	3	0.729	0	0.110	0	0.007	0	0.021			Link
S190521r	Initial	2019-05-21	07:43:59.463379	BBH (99.9%)	488 deg ²	1136.1±279.3 Mpc	993.97 s	0	0.729	0	0.110	0	0.007	0	0.021			Link
S190602aq	Initial	2019-06-02	17:59:27.089355	BBH (99.0%)	1172 deg ²	797.3±238.5 Mpc	993.63 s	0	0.729	1	0.110	0	0.007	0	0.021	2.61%	1.57%	Link
S190630ag	Update	2019-06-30	18:52:05.179550	BBH (94.3%)	1483 deg ²	925.7±258.5 Mpc	992.45 s	2	0.729	0	0.110	0	0.007	0	0.021			Link
S190701ah	Update	2019-07-01	20:33:06.577637	BBH (93.4%)	49 deg ²	1848.9±445.5 Mpc	992.49 s	0	0.729	0	0.110	0	0.007	0	0.021			Link
S190706ai	Update	2019-07-06	22:26:41.344727	BBH (99.0%)	825 deg ²	5262.9±1401.9 Mpc	992.37 s	3	0.729	0	0.110	0	0.007	0	0.021			Link
S190707q	Update	2019-07-07	09:33:26.181226	BBH (100.0%)	921 deg ²	781.4±211.3 Mpc	992.43 s	0	0.729	0	0.110	0	0.007	0	0.021			Link
S190718y	Initial	2019-07-18	14:35:12.067865	Terrestrial (97.9%)	7246 deg ²	226.6±164.9 Mpc	992.95 s	2	0.729	0	0.110	0	0.007	0	0.021			Link
S190720a	Update	2019-07-20	00:08:36.704102	BBH (98.9%)	443 deg ²	868.5±282.8 Mpc	992.80 s	0	0.729	0	0.110	0	0.007	0	0.021			Link

Figure 49: Screenshot of the web page on SK intranet summarising the results of GW follow-ups.

6.3.3 PDF

Using PyLaTeX, a PDF is created for each GW trigger, that is containing all relevant information and plots.

Follow-up of S190513bm

The Super-Kamiokande collaboration

April 30, 2020

1 Summary of the alert

- Status of the notice: Initial
- Date of the notice: 2019-05-13 21:22:17
- Unique name of the trigger: S190513bm
- Date of the trigger: 2019-05-13 20:54:28.747089
- JD of the trigger: 2458617.37116
- Type of event: BBH (94.3%)
- Distance: 1987.0 +/- 501.2 Mpc

2 Status of Super-Kamiokande

During the 1000 seconds time window:

Run	Subrun	Start time (JST)	Livetime (seconds)	Overlapping (%)
81163	334	190514/05:44	116.44	30.16
81163	335	190514/05:46	116.11	100.00
81163	336	190514/05:48	114.80	100.00
81163	337	190514/05:50	114.74	100.00
81163	338	190514/05:52	113.10	100.00
81163	339	190514/05:54	114.68	100.00
81163	340	190514/05:56	117.77	100.00
81163	341	190514/05:58	117.79	100.00
81163	342	190514/06:00	116.60	100.00
81163	343	190514/06:02	115.60	28.43
TOTAL (over time window)			993.57 seconds	

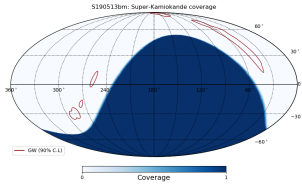


Figure 1: Sky coverage of Super-Kamiokande UPMU

- Fraction of the GW skymap probability covered by Super-Kamiokande UPMU: 0.00%
- Fraction of the GW 90% area covered by Super-Kamiokande UPMU: 0.00%

Table 2: List of Super-Kamiokande ATMPD events

Time	Delta T	Type	RA [deg]	Dec [deg]	Energy [GeV]	Ang.Unc [deg]
2019-05-13 20:51:28	-183.272552	FC	278.917694	-36.721024	0.707847	28.276404

4 Fluence limits

Table 3: Constraints on neutrino fluence using Super-Kamiokande samples

Sample	Obs.	Exp.	min-max 90%UL in GW contour				
			S	$\Phi(\nu_\mu)$ [cm^{-2}]	$\Phi(\nu_e)$ [cm^{-2}]	$\Phi(\bar{\nu}_\mu)$ [cm^{-2}]	$\Phi(\bar{\nu}_e)$ [cm^{-2}]
FC	1	0.110	3.79	$8.79 \cdot 10^4 - 8.92 \cdot 10^4$	$6.46 \cdot 10^4 - 6.62 \cdot 10^4$	$2.49 \cdot 10^5 - 2.52 \cdot 10^5$	$1.69 \cdot 10^5 - 1.76 \cdot 10^5$
PC	0	0.007	2.30	$1.07 \cdot 10^5 - 1.14 \cdot 10^5$	$9.06 \cdot 10^5 - 1.50 \cdot 10^6$	$1.83 \cdot 10^5 - 2.02 \cdot 10^5$	$1.63 \cdot 10^6 - 3.24 \cdot 10^6$
UPMU	0	0.021	2.30	-	-	-	-
LOWE	0	0.729	-	-	-	-	-
$\Lambda (> TS_{\text{bkg},50\%})$	-	-	-	$1.93 \cdot 10^4 - 2.98 \cdot 10^4$	-	-	-
$\Lambda (> TS_{\text{bkg},90\%})$	-	-	-	$2.25 \cdot 10^4 - 3.69 \cdot 10^4$	-	-	-
$\Lambda (> TS_{\text{bkg},99\%})$	-	-	-	$2.80 \cdot 10^4 - 4.79 \cdot 10^4$	-	-	-

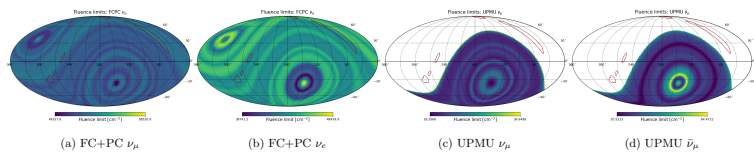


Figure 5: Fluence limits maps [cm^{-2}]

5 ATMPD statistical analysis

The probability to observe data at least as extreme as the real data, given the expected background, using simple Poisson statistics is: 12.92%

Table 4: p-values from statistical analyses

Method	Lambda	Chi-square
p-value	5.67%	12.78%

3 Super-Kamiokande events in the 1000 seconds time window

Table 1: Number of observed events (compared to background expectation)

Sample	FC	PC	UPMU	LOWE
Observed	1	0	0	0
Expected	0.110	0.007	0.021	0.729

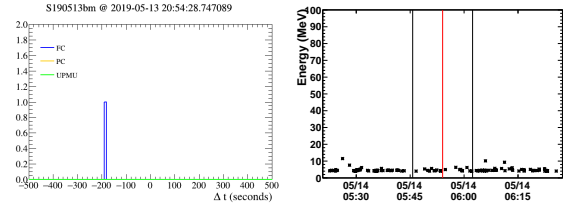


Figure 2: Time distribution of ATMPD (left) and LOWE (right) events in the time window

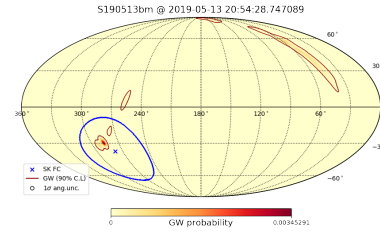


Figure 3: GW skymap and distribution of ATMPD events

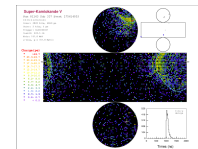


Figure 4: SK ATMPD events display (in the order of appearance in the above table)

No observed LOWE events

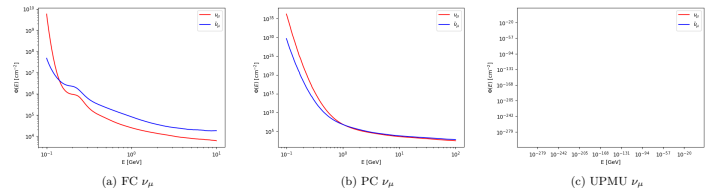


Figure 6: Energy-dependent fluence limits [cm^{-2}]

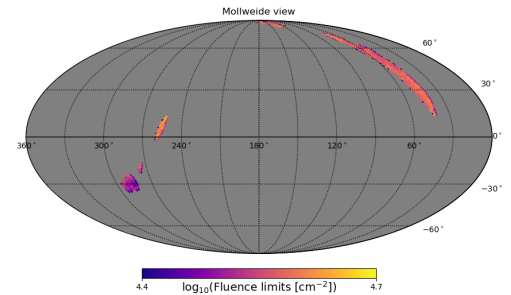


Figure 7: Fluence limits for ν_μ using the Lambda method ($TS_{\text{thr}} > TS_{\text{bkg},99\%}$) [cm^{-2}]

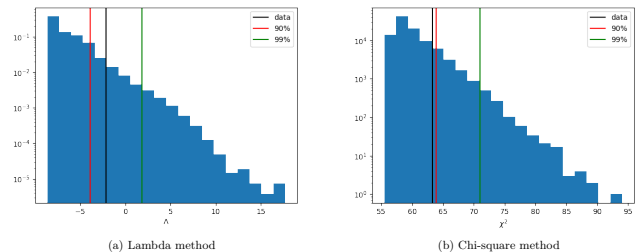


Figure 8: TS background distribution compared to the data value for the two methods

7 Follow-up of O3 real-time events

From April 2019 to March 2020, the LIGO-Virgo collaboration has sent 80 public real-time alerts, 24 of which have been retracted, leaving 56 GW triggers that are interesting for follow-up observations.

7.1 All GW triggers

The [Table 11](#) summarises the follow-ups of O3 events and the [Table 13](#) shows the full description of all follow-ups performed with GW triggers from O3 observation run, including the ones where SK was down. For more information, you can go to the PDF that is created for each trigger, as described in [section 6.3.3](#), on the web page.

Name	Value
Total number of GW triggers	80
Number of non-retracted GW triggers	56
Number of triggers with SK livetime	46
Number of triggers with SK events	8

Table 11: Summary of the number of GW triggers in O3 observation run.

We can sum the number of observed and expected events for each sample to search for any deviation from background expectation.

Sample	Observed	Expected	p-value (%)
FC	6	5.06	39.48
PC	0	0.33	100.00
UPMU	2	0.74	16.98
LOWE	38	31.98	25.67

Table 12: Total number of observed and expected events for all O3 observation run, along with the associated Poisson p-value.

Table 13: Summary of all GW triggers for the O3 observation run. The different columns are: Trigger name ; Alert time in UTC ; Most probable GW event type (with its probability, classification based on the masses) ; area of the 90% GW contour ; best-fit distance to the astrophysical object ; SK detector livetime ; number of observed events and number of expected background events for the four samples.

Name	Alert UTC	Type	$\mathcal{A}_{GW}^{90\%}$ [deg ²]	d [Mpc]	L [s]	FC		PC		UPMU		LOWE	
						N_{obs}	N_{exp}	N_{obs}	N_{exp}	N_{obs}	N_{exp}	N_{obs}	N_{exp}
S190408an	2019-04-08 18:18:02	BBH (100.0%)	386	1472.9	993.1	0	0.111	0	0.007	0	0.016	3	0.729
S190412m	2019-04-12 05:30:44	BBH (100.0%)	157	812.2	993.1	0	0.111	0	0.007	0	0.016	1	0.729
S190421ar	2019-04-21 21:38:56	BBH (96.7%)	1443	1628.4	993.1	0	0.111	0	0.007	0	0.016	3	0.729
S190425z	2019-04-25 08:18:05	BNS (99.9%)	7461	156.1	993.4	0	0.111	0	0.007	0	0.016	1	0.729
S190426c	2019-04-26 15:21:55	BNS (49.3%)	1131	376.7	992.6	0	0.111	0	0.007	1	0.016	0	0.729
S190503bf	2019-05-03 18:54:04	BBH (96.3%)	448	421.1	993.2	0	0.111	0	0.007	0	0.016	0	0.729
S190510g	2019-05-10 02:59:39	Terrestrial (58.0%)	1166	227.2	0.0	-	-	-	-	-	-	-	-
S190512at	2019-05-12 18:07:14	BBH (99.0%)	252	1387.7	993.7	0	0.111	0	0.007	0	0.016	1	0.729
S190513bm	2019-05-13 20:54:28	BBH (94.3%)	691	1987.0	993.6	1	0.111	0	0.007	0	0.016	0	0.729
S190517h	2019-05-17 05:51:01	BBH (98.3%)	939	2950.0	0.0	-	-	-	-	-	-	-	-
S190519bj	2019-05-19 15:35:44	BBH (95.6%)	967	3153.5	993.7	0	0.111	0	0.007	0	0.016	1	0.729
S190521g	2019-05-21 03:02:29	BBH (96.6%)	765	3931.4	994.0	0	0.111	0	0.007	0	0.016	3	0.729
S190521r	2019-05-21 07:43:59	BBH (99.9%)	488	1136.1	994.0	0	0.111	0	0.007	0	0.016	0	0.729
S190602aq	2019-06-02 17:59:27	BBH (99.0%)	1172	797.3	993.6	1	0.111	0	0.007	0	0.016	0	0.729
S190630ag	2019-06-30 18:52:05	BBH (94.3%)	1483	925.7	992.4	0	0.111	0	0.007	0	0.016	2	0.729
S190701ah	2019-07-01 20:33:06	BBH (93.4%)	49	1848.9	992.5	0	0.111	0	0.007	0	0.016	0	0.729
S190706ai	2019-07-06 22:26:41	BBH (99.0%)	825	5262.9	992.4	0	0.111	0	0.007	0	0.016	2	0.729
S190707q	2019-07-07 09:33:26	BBH (100.0%)	921	781.4	992.4	0	0.111	0	0.007	0	0.016	0	0.729
S190718y	2019-07-18 14:35:12	Terrestrial (97.9%)	7246	226.6	993.0	0	0.111	0	0.007	0	0.016	1	0.729
S190720a	2019-07-20 00:08:36	BBH (98.9%)	443	868.5	992.8	0	0.111	0	0.007	0	0.016	0	0.729
S190727h	2019-07-27 06:03:33	BBH (92.2%)	152	2838.6	992.5	0	0.111	0	0.007	0	0.016	0	0.729
S190728q	2019-07-28 06:45:10	BBH (95.4%)	105	873.8	992.5	1	0.111	0	0.007	0	0.016	2	0.955
S190814bv	2019-08-14 21:10:39	NSBH (99.8%)	24	267.4	993.9	1	0.111	0	0.007	0	0.016	0	0.729
S190828j	2019-08-28 06:34:05	BBH (100.0%)	228	1946.3	542.5	0	0.061	0	0.004	0	0.009	1	0.962
S190828l	2019-08-28 06:55:09	BBH (100.0%)	358	1528.3	0.0	-	-	-	-	-	-	-	-
S190901ap	2019-09-01 23:31:01	BNS (86.1%)	14753	240.9	993.9	0	0.111	0	0.007	0	0.016	1	0.729
S190910d	2019-09-10 01:26:19	NSBH (97.6%)	2482	631.5	994.1	0	0.111	0	0.007	0	0.016	1	0.729
S190910h	2019-09-10 08:29:58	BNS (61.2%)	24265	229.5	994.0	0	0.111	0	0.007	0	0.016	0	0.729
S190915ak	2019-09-15 23:57:02	BBH (99.5%)	318	1583.5	0.0	-	-	-	-	-	-	-	-
S190923y	2019-09-23 12:55:59	NSBH (67.8%)	2107	438.1	994.2	0	0.111	0	0.007	0	0.016	1	0.729
S190924h	2019-09-24 02:18:46	MassGap (100.0%)	303	547.9	994.1	1	0.111	0	0.007	0	0.016	0	0.729
S190930s	2019-09-30 13:35:41	MassGap (95.1%)	1747	708.9	994.1	0	0.111	0	0.007	0	0.016	0	0.729
S190930t	2019-09-30 14:34:07	NSBH (74.3%)	24221	108.5	994.3	0	0.111	0	0.007	0	0.016	2	0.729
S191105e	2019-11-05 14:35:21	BBH (95.3%)	643	1182.8	991.6	0	0.111	0	0.007	0	0.016	0	0.729

Table 13: Summary of all GW triggers for the O3 observation run. The different columns are: Trigger name ; Alert time in UTC ; Most probable GW event type (with its probability, classification based on the masses) ; area of the 90% GW contour ; best-fit distance to the astrophysical object ; SK detector livetime ; number of observed events and number of expected background events for the four samples.

Name	Alert UTC	Type	$\mathcal{A}_{GW}^{90\%}$ [deg ²]	d [Mpc]	L [s]	FC		PC		UPMU		LOWE	
						N_{obs}	N_{exp}	N_{obs}	N_{exp}	N_{obs}	N_{exp}	N_{obs}	N_{exp}
S191109d	2019-11-09 01:07:17	BBH (100.0%)	1487	1810.1	0.0	-	-	-	-	-	-	-	-
S191129u	2019-11-29 13:40:29	BBH (100.0%)	852	742.4	992.1	0	0.111	0	0.007	0	0.016	2	0.729
S191204r	2019-12-04 17:15:26	BBH (100.0%)	104	677.5	992.1	0	0.111	0	0.007	0	0.016	0	0.729
S191205ah	2019-12-05 21:52:08	NSBH (93.2%)	6378	385.0	991.9	0	0.111	0	0.007	0	0.016	2	0.729
S191213g	2019-12-13 04:34:08	BNS (76.8%)	4480	200.9	978.6	1	0.110	0	0.007	0	0.016	2	0.729
S191215w	2019-12-15 22:30:52	BBH (99.7%)	361	1769.6	992.0	0	0.111	0	0.007	0	0.016	2	0.729
S191216ap	2019-12-16 21:33:38	BBH (99.1%)	253	375.9	992.0	0	0.111	0	0.007	0	0.016	0	0.729
S191222n	2019-12-22 03:35:37	BBH (100.0%)	1850	2518.1	992.0	0	0.111	0	0.007	0	0.016	0	0.729
S200105ae	2020-01-05 16:24:26	Terrestrial (97.3%)	7373	282.8	991.8	0	0.111	0	0.007	0	0.016	0	0.998
S200112r	2020-01-12 15:58:38	BBH (100.0%)	6199	1136.3	992.1	0	0.111	0	0.007	0	0.016	1	0.729
S200114f	2020-01-14 02:08:18	Unmodeled	403	-	0.0	-	-	-	-	-	-	-	-
S200115j	2020-01-15 04:23:09	MassGap (100.0%)	765	340.2	991.9	0	0.111	0	0.007	0	0.016	0	0.729
S200128d	2020-01-28 02:20:11	BBH (96.9%)	2520	4031.1	991.6	0	0.111	0	0.007	0	0.016	3	0.729
S200129m	2020-01-29 06:54:58	BBH (100.0%)	54	908.4	991.6	0	0.111	0	0.007	0	0.016	1	0.729
S200208q	2020-02-08 13:01:17	BBH (99.3%)	27	2142.0	991.9	0	0.111	0	0.007	0	0.016	0	0.729
S200213t	2020-02-13 04:10:40	BNS (62.9%)	2325	200.9	0.0	-	-	-	-	-	-	-	-
S200219ac	2020-02-19 09:44:15	BBH (96.4%)	781	3533.1	0.0	-	-	-	-	-	-	-	-
S200224ca	2020-02-24 22:22:34	BBH (100.0%)	73	1575.0	0.0	-	-	-	-	-	-	-	-
S200225q	2020-02-25 06:04:21	BBH (95.8%)	22	994.9	991.4	0	0.111	0	0.007	0	0.016	1	0.729
S200302c	2020-03-02 01:58:11	BBH (89.0%)	5656	1820.1	0.0	-	-	-	-	-	-	-	-
S200311bg	2020-03-11 11:58:53	BBH (100.0%)	35	1114.6	992.5	0	0.111	0	0.007	0	0.016	0	0.729
S200316bj	2020-03-16 21:57:56	MassGap (99.6%)	507	1178.0	992.6	0	0.111	0	0.007	1	0.016	1	0.729

8 Follow-up of O3a catalogued events

8.1 All GW triggers

In the new GWTC-2 catalog [7], 39 gravitational waves were reported. Out of these, 36 have SK detector running and 10 have SK events in time coincidence.

The Figure 50 and the Table 15 are showing the final results for all the events. We can sum the number of observed and expected events for each sample to search for any deviation from background expectation.

Sample	Observed	Expected	p-value (%)
FC	8	3.95	4.84
PC	0	0.26	100.00
UPMU	2	0.58	11.47

Table 14: Total number of observed and expected events for O3a observation run, along with the associated Poisson p-value.

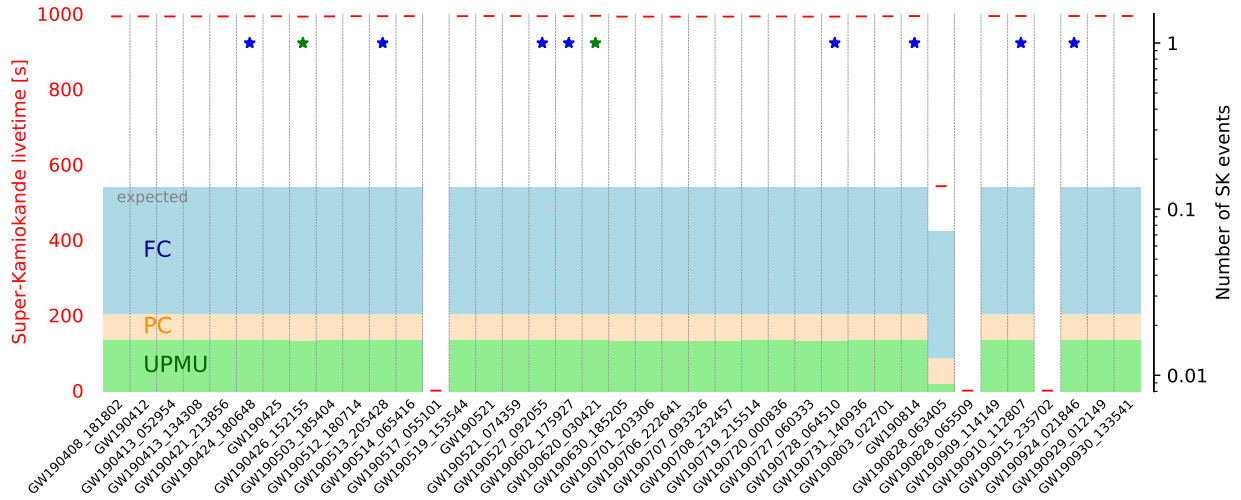


Figure 50: Summary of observations in O3a catalog events.

Table 15: Summary of all GW triggers for the O3a observation run. The different columns are: Trigger name ; Alert time in UTC ; Most probable GW event type (with its probability, classification based on the masses) ; area of the 90% GW contour ; best-fit distance to the astrophysical object ; SK detector livetime ; number of observed events and number of expected background events for the four samples.

Name	Alert UTC	Type	$A_{GW}^{90\%}$ [deg ²]	d [Mpc]	L [s]	FC		PC		UPMU		LOWE	
						N_{obs}	N_{exp}	N_{obs}	N_{exp}	N_{obs}	N_{exp}	N_{obs}	N_{exp}
GW190408_181802	2019-04-08 18:18:02	BBH	41253	1547.5	993.1	0	0.111	0	0.007	0	0.016	3	0.729
GW190412	2019-04-12 05:30:44	BBH	41253	734.1	993.1	0	0.111	0	0.007	0	0.016	0	0.729
GW190413_052954	2019-04-13 05:29:54	BBH	41253	4189.6	993.0	0	0.111	0	0.007	0	0.016	0	0.729
GW190413_134308	2019-04-13 13:43:08	BBH	41253	5181.6	993.1	0	0.111	0	0.007	0	0.016	0	0.729
GW190421_213856	2019-04-21 21:38:56	BBH	41253	3165.5	993.1	0	0.111	0	0.007	0	0.016	3	0.729
GW190424_180648	2019-04-24 18:06:48	BBH	41253	2568.4	993.4	1	0.111	0	0.007	0	0.016	1	0.729
GW190425	2019-04-25 08:18:05	BNS	41253	156.8	993.4	0	0.111	0	0.007	0	0.016	1	0.729
GW190426_152155	2019-04-26 15:21:55	NSBH	41253	377.2	992.6	0	0.111	0	0.007	1	0.016	0	0.729
GW190503_185404	2019-05-03 18:54:04	BBH	41253	1527.3	993.2	0	0.111	0	0.007	0	0.016	0	0.729
GW190512_180714	2019-05-12 18:07:14	BBH	41253	1462.5	993.7	0	0.111	0	0.007	0	0.016	1	0.729
GW190513_205428	2019-05-13 20:54:28	BBH	41253	2189.7	993.6	1	0.111	0	0.007	0	0.016	0	0.729
GW190514_065416	2019-05-14 06:54:16	BBH	41253	4987.6	993.8	0	0.111	0	0.007	0	0.016	1	0.729
GW190517_055101	2019-05-17 05:51:01	BBH	41253	2270.5	0.0	-	-	-	-	-	-	-	-
GW190519_153544	2019-05-19 15:35:44	BBH	41253	3023.5	993.7	0	0.111	0	0.007	0	0.016	1	0.729
GW190521	2019-05-21 03:02:29	BBH	41253	4566.9	994.0	0	0.111	0	0.007	0	0.016	0	0.729
GW190521_074359	2019-05-21 07:43:59	BBH	41253	1244.2	994.0	0	0.111	0	0.007	0	0.016	0	0.729
GW190527_092055	2019-05-27 09:20:55	BBH	41253	3562.9	993.7	1	0.111	0	0.007	0	0.016	1	0.729
GW190602_175927	2019-06-02 17:59:27	BBH	41253	3138.1	993.6	1	0.111	0	0.007	0	0.016	0	0.729
GW190620_030421	2019-06-20 03:04:21	BBH	41253	3210.9	994.5	0	0.111	0	0.007	1	0.016	1	0.729
GW190630_185205	2019-06-30 18:52:05	BBH	41253	956.2	992.4	0	0.111	0	0.007	0	0.016	2	0.729
GW190701_203306	2019-07-01 20:33:06	BBH	41253	2152.4	992.5	0	0.111	0	0.007	0	0.016	0	0.729
GW190706_222641	2019-07-06 22:26:41	BBH	41253	5184.0	992.4	0	0.111	0	0.007	0	0.016	2	0.729
GW190707_093326	2019-07-07 09:33:26	BBH	41253	790.8	992.4	0	0.111	0	0.007	0	0.016	0	0.729
GW190708_232457	2019-07-08 23:24:57	BBH	41253	887.9	992.5	0	0.111	0	0.007	0	0.016	0	0.729
GW190719_215514	2019-07-19 21:55:14	BBH	41253	4786.3	993.0	0	0.111	0	0.007	0	0.016	1	0.729
GW190720_000836	2019-07-20 00:08:36	BBH	41253	906.0	992.8	0	0.111	0	0.007	0	0.016	0	0.729
GW190727_060333	2019-07-27 06:03:34	BBH	41253	3608.9	992.5	0	0.111	0	0.007	0	0.016	0	0.729
GW190728_064510	2019-07-28 06:45:10	BBH	41253	857.6	992.5	1	0.111	0	0.007	0	0.016	2	0.955
GW190731_140936	2019-07-31 14:09:36	BBH	41253	4033.7	993.0	0	0.111	0	0.007	0	0.016	1	0.729
GW190803_022701	2019-08-03 02:27:01	BBH	41253	3749.6	993.4	0	0.111	0	0.007	0	0.016	0	0.729
GW190814	2019-08-14 21:10:38	NSBH	41253	240.7	993.9	1	0.111	0	0.007	0	0.016	0	0.729
GW190828_063405	2019-08-28 06:34:05	BBH	41253	2160.3	542.5	0	0.061	0	0.004	0	0.009	1	0.962
GW190828_065509	2019-08-28 06:55:09	BBH	41253	1657.8	0.0	-	-	-	-	-	-	-	-
GW190909_114149	2019-09-09 11:41:49	BBH	41253	4923.7	994.0	0	0.111	0	0.007	0	0.016	0	0.729

Table 15: Summary of all GW triggers for the O3a observation run. The different columns are: Trigger name ; Alert time in UTC ; Most probable GW event type (with its probability, classification based on the masses) ; area of the 90% GW contour ; best-fit distance to the astrophysical object ; SK detector livetime ; number of observed events and number of expected background events for the four samples.

Name	Alert UTC	Type	$\mathcal{A}_{GW}^{90\%}$ [deg ²]	d [Mpc]	L [s]	FC		PC		UPMU		LOWE	
						N_{obs}	N_{exp}	N_{obs}	N_{exp}	N_{obs}	N_{exp}	N_{obs}	N_{exp}
GW190910_112807	2019-09-10 11:28:07	BBH	41253	1670.1	994.1	1	0.111	0	0.007	0	0.016	2	0.729
GW190915_235702	2019-09-15 23:57:02	BBH	41253	1714.6	0.0	-	-	-	-	-	-	-	-
GW190924_021846	2019-09-24 02:18:46	BBH	41253	572.4	994.1	1	0.111	0	0.007	0	0.016	0	0.729
GW190929_012149	2019-09-29 01:21:49	BBH	41253	3901.5	994.2	0	0.111	0	0.007	0	0.016	0	0.729
GW190930_133541	2019-09-30 13:35:41	BBH	41253	785.9	994.1	0	0.111	0	0.007	0	0.016	0	0.729

8.2 Flux limits and Fluence limits

we can compute flux limits for all GW triggers taking benefit of the three ATMPD samples and marginalising over GW localisation. The [Table 17](#) shows a summary of the results for FC+PC and UPMU, $\nu_\mu + \bar{\nu}_\mu$ and $\nu_e + \bar{\nu}_e$. Similarly, the [Table 16](#) shows the results with the combined (Λ) method.

Table 16: $E^2 dn/dE$ limits [in GeV cm^{-2}] for all GW triggers with the combined method.

Name	ν_μ	$\bar{\nu}_\mu$	ν_e	$\bar{\nu}_e$
GW190408.181802	$2.31 \cdot 10^3$	$4.56 \cdot 10^3$	$1.82 \cdot 10^3$	$3.13 \cdot 10^3$
GW190412	$3.14 \cdot 10^1$	$4.39 \cdot 10^1$	$2.11 \cdot 10^3$	$4.64 \cdot 10^3$
GW190413.052954	$2.23 \cdot 10^3$	$4.41 \cdot 10^3$	$1.83 \cdot 10^3$	$3.31 \cdot 10^3$
GW190413.134308	$2.20 \cdot 10^3$	$4.55 \cdot 10^3$	$1.84 \cdot 10^3$	$3.53 \cdot 10^3$
GW190421.213856	$3.42 \cdot 10^1$	$4.51 \cdot 10^1$	$2.24 \cdot 10^3$	$4.87 \cdot 10^3$
GW190424.180648	$2.67 \cdot 10^3$	$4.92 \cdot 10^3$	$2.99 \cdot 10^3$	$5.81 \cdot 10^3$
GW190425	$2.16 \cdot 10^3$	$4.20 \cdot 10^3$	$2.09 \cdot 10^3$	$4.28 \cdot 10^3$
GW190426.152155	$2.35 \cdot 10^3$	$4.08 \cdot 10^3$	$1.97 \cdot 10^3$	$3.89 \cdot 10^3$
GW190503.185404	$4.29 \cdot 10^1$	$9.02 \cdot 10^1$	$2.10 \cdot 10^3$	$4.20 \cdot 10^3$
GW190512.180714	$2.32 \cdot 10^3$	$4.53 \cdot 10^3$	$1.82 \cdot 10^3$	$3.14 \cdot 10^3$
GW190513.205428	$3.66 \cdot 10^3$	$6.68 \cdot 10^3$	$2.93 \cdot 10^3$	$5.03 \cdot 10^3$
GW190514.065416	$2.27 \cdot 10^3$	$4.45 \cdot 10^3$	$1.86 \cdot 10^3$	$3.29 \cdot 10^3$
GW190519.153544	$2.06 \cdot 10^3$	$4.31 \cdot 10^3$	$1.90 \cdot 10^3$	$3.39 \cdot 10^3$
GW190521	$3.75 \cdot 10^1$	$4.82 \cdot 10^1$	$2.21 \cdot 10^3$	$4.60 \cdot 10^3$
GW190521.074359	$3.52 \cdot 10^1$	$4.04 \cdot 10^1$	$2.26 \cdot 10^3$	$4.86 \cdot 10^3$
GW190527.092055	$3.47 \cdot 10^1$	$4.49 \cdot 10^1$	$2.77 \cdot 10^3$	$6.21 \cdot 10^3$
GW190602.175927	$5.61 \cdot 10^1$	$7.58 \cdot 10^1$	$3.89 \cdot 10^3$	$8.28 \cdot 10^3$
GW190620.030421	$2.11 \cdot 10^3$	$4.14 \cdot 10^3$	$2.16 \cdot 10^3$	$4.39 \cdot 10^3$
GW190630.185205	$2.28 \cdot 10^3$	$4.34 \cdot 10^3$	$2.08 \cdot 10^3$	$4.46 \cdot 10^3$
GW190701.203306	$2.34 \cdot 10^3$	$3.75 \cdot 10^3$	$2.13 \cdot 10^3$	$4.74 \cdot 10^3$
GW190706.222641	$1.29 \cdot 10^3$	$2.25 \cdot 10^3$	$2.23 \cdot 10^3$	$3.33 \cdot 10^3$
GW190707.093326	$1.87 \cdot 10^3$	$3.85 \cdot 10^3$	$2.11 \cdot 10^3$	$3.28 \cdot 10^3$
GW190708.232457	$2.15 \cdot 10^3$	$4.18 \cdot 10^3$	$2.09 \cdot 10^3$	$4.13 \cdot 10^3$
GW190719.215514	$1.92 \cdot 10^3$	$3.78 \cdot 10^3$	$2.09 \cdot 10^3$	$3.32 \cdot 10^3$
GW190720.000836	$3.36 \cdot 10^1$	$4.76 \cdot 10^1$	$2.22 \cdot 10^3$	$4.54 \cdot 10^3$
GW190727.060333	$3.58 \cdot 10^1$	$5.02 \cdot 10^1$	$2.17 \cdot 10^3$	$4.53 \cdot 10^3$
GW190728.064510	$3.59 \cdot 10^1$	$4.00 \cdot 10^1$	$3.30 \cdot 10^3$	$6.95 \cdot 10^3$
GW190731.140936	$3.42 \cdot 10^1$	$4.46 \cdot 10^1$	$2.19 \cdot 10^3$	$4.86 \cdot 10^3$
GW190803.022701	$2.33 \cdot 10^3$	$4.22 \cdot 10^3$	$2.11 \cdot 10^3$	$4.82 \cdot 10^3$
GW190814	$2.16 \cdot 10^3$	$4.58 \cdot 10^3$	$1.82 \cdot 10^3$	$3.62 \cdot 10^3$
GW190828.063405	$1.31 \cdot 10^3$	$2.03 \cdot 10^3$	$2.25 \cdot 10^3$	$3.48 \cdot 10^3$
GW190909.114149	$2.10 \cdot 10^3$	$4.29 \cdot 10^3$	$1.97 \cdot 10^3$	$3.40 \cdot 10^3$
GW190910.112807	$2.36 \cdot 10^3$	$4.46 \cdot 10^3$	$3.09 \cdot 10^3$	$6.08 \cdot 10^3$
GW190924.021846	$2.46 \cdot 10^3$	$4.09 \cdot 10^3$	$2.26 \cdot 10^3$	$5.05 \cdot 10^3$
GW190929.012149	$1.68 \cdot 10^3$	$3.32 \cdot 10^3$	$2.25 \cdot 10^3$	$3.65 \cdot 10^3$
GW190930.133541	$2.34 \cdot 10^3$	$5.47 \cdot 10^3$	$1.96 \cdot 10^3$	$4.52 \cdot 10^3$

Table 17: Summary of $E^2 dn/dE$ limits [in GeV cm^{-2}] for all GW triggers. In the UPMU columns, empty values corresponds to cases where the GW localisation is mainly above the horizon.

Name	FC				PC				UPMU	
	ν_μ	$\bar{\nu}_\mu$	ν_e	$\bar{\nu}_e$	ν_μ	$\bar{\nu}_\mu$	ν_e	$\bar{\nu}_e$	ν_μ	$\bar{\nu}_\mu$
GW190408.181802	$4.02 \cdot 10^3$	$9.00 \cdot 10^3$	$2.10 \cdot 10^3$	$3.26 \cdot 10^3$	$5.26 \cdot 10^3$	$9.03 \cdot 10^3$	$1.13 \cdot 10^4$	$5.98 \cdot 10^4$	(unseen)	(unseen)
GW190412	$3.95 \cdot 10^3$	$9.40 \cdot 10^3$	$2.17 \cdot 10^3$	$4.76 \cdot 10^3$	$4.87 \cdot 10^3$	$8.43 \cdot 10^3$	$3.76 \cdot 10^4$	$9.24 \cdot 10^4$	$3.18 \cdot 10^1$	$4.42 \cdot 10^1$
GW190413.052954	$4.00 \cdot 10^3$	$9.23 \cdot 10^3$	$2.13 \cdot 10^3$	$3.49 \cdot 10^3$	$5.16 \cdot 10^3$	$8.68 \cdot 10^3$	$1.27 \cdot 10^4$	$6.57 \cdot 10^4$	(unseen)	(unseen)
GW190413.134308	$3.97 \cdot 10^3$	$9.62 \cdot 10^3$	$2.11 \cdot 10^3$	$3.72 \cdot 10^3$	$4.89 \cdot 10^3$	$8.73 \cdot 10^3$	$1.31 \cdot 10^4$	$5.51 \cdot 10^4$	(unseen)	(unseen)
GW190421.213856	$3.93 \cdot 10^3$	$9.05 \cdot 10^3$	$2.32 \cdot 10^3$	$5.06 \cdot 10^3$	$4.76 \cdot 10^3$	$8.34 \cdot 10^3$	$3.02 \cdot 10^4$	$8.06 \cdot 10^4$	$3.47 \cdot 10^1$	$4.56 \cdot 10^1$
GW190424.180648	$6.50 \cdot 10^3$	$1.57 \cdot 10^4$	$3.70 \cdot 10^3$	$7.32 \cdot 10^3$	$5.09 \cdot 10^3$	$8.76 \cdot 10^3$	$3.68 \cdot 10^4$	$1.15 \cdot 10^5$	(unseen)	(unseen)
GW190425	$3.95 \cdot 10^3$	$9.47 \cdot 10^3$	$2.25 \cdot 10^3$	$4.45 \cdot 10^3$	$5.08 \cdot 10^3$	$8.77 \cdot 10^3$	$3.61 \cdot 10^4$	$1.15 \cdot 10^5$	(unseen)	(unseen)
GW190426.152155	$4.01 \cdot 10^3$	$8.92 \cdot 10^3$	$2.25 \cdot 10^3$	$3.95 \cdot 10^3$	$5.49 \cdot 10^3$	$7.66 \cdot 10^3$	$1.29 \cdot 10^4$	$1.15 \cdot 10^5$	(unseen)	(unseen)
GW190503.185404	$4.03 \cdot 10^3$	$1.00 \cdot 10^4$	$2.14 \cdot 10^3$	$4.19 \cdot 10^3$	$5.81 \cdot 10^3$	$8.71 \cdot 10^3$	$4.31 \cdot 10^4$	$2.23 \cdot 10^5$	$4.37 \cdot 10^1$	$9.20 \cdot 10^1$
GW190512.180714	$4.02 \cdot 10^3$	$8.96 \cdot 10^3$	$2.11 \cdot 10^3$	$3.27 \cdot 10^3$	$5.29 \cdot 10^3$	$8.96 \cdot 10^3$	$1.14 \cdot 10^4$	$6.35 \cdot 10^4$	(unseen)	(unseen)
GW190513.205428	$6.61 \cdot 10^3$	$1.47 \cdot 10^4$	$3.52 \cdot 10^3$	$5.61 \cdot 10^3$	$5.32 \cdot 10^3$	$8.58 \cdot 10^3$	$1.18 \cdot 10^4$	$7.29 \cdot 10^4$	(unseen)	(unseen)
GW190514.065416	$4.01 \cdot 10^3$	$9.15 \cdot 10^3$	$2.13 \cdot 10^3$	$3.43 \cdot 10^3$	$5.21 \cdot 10^3$	$8.73 \cdot 10^3$	$1.30 \cdot 10^4$	$6.71 \cdot 10^4$	(unseen)	(unseen)
GW190519.153544	$3.96 \cdot 10^3$	$9.84 \cdot 10^3$	$2.15 \cdot 10^3$	$3.59 \cdot 10^3$	$4.82 \cdot 10^3$	$8.59 \cdot 10^3$	$1.71 \cdot 10^4$	$5.19 \cdot 10^4$	(unseen)	(unseen)
GW190521	$3.96 \cdot 10^3$	$9.59 \cdot 10^3$	$2.28 \cdot 10^3$	$4.72 \cdot 10^3$	$4.89 \cdot 10^3$	$8.34 \cdot 10^3$	$4.00 \cdot 10^4$	$1.02 \cdot 10^5$	$3.75 \cdot 10^1$	$4.80 \cdot 10^1$
GW190521.074359	$3.91 \cdot 10^3$	$9.20 \cdot 10^3$	$2.34 \cdot 10^3$	$4.94 \cdot 10^3$	$4.87 \cdot 10^3$	$7.43 \cdot 10^3$	$3.37 \cdot 10^4$	$1.17 \cdot 10^5$	$3.58 \cdot 10^1$	$4.09 \cdot 10^1$
GW190527.092055	$6.39 \cdot 10^3$	$1.49 \cdot 10^4$	$3.59 \cdot 10^3$	$8.21 \cdot 10^3$	$4.62 \cdot 10^3$	$9.97 \cdot 10^3$	$3.22 \cdot 10^4$	$7.41 \cdot 10^4$	$3.50 \cdot 10^1$	$4.52 \cdot 10^1$
GW190602.175927	$6.29 \cdot 10^3$	$1.54 \cdot 10^4$	$3.53 \cdot 10^3$	$7.90 \cdot 10^3$	$4.68 \cdot 10^3$	$1.03 \cdot 10^4$	$3.30 \cdot 10^4$	$7.23 \cdot 10^4$	$3.53 \cdot 10^1$	$4.71 \cdot 10^1$
GW190620.030421	$3.95 \cdot 10^3$	$9.50 \cdot 10^3$	$2.25 \cdot 10^3$	$4.53 \cdot 10^3$	$5.00 \cdot 10^3$	$8.76 \cdot 10^3$	$3.61 \cdot 10^4$	$1.07 \cdot 10^5$	(unseen)	(unseen)
GW190630.185205	$3.94 \cdot 10^3$	$9.29 \cdot 10^3$	$2.24 \cdot 10^3$	$4.62 \cdot 10^3$	$5.26 \cdot 10^3$	$8.84 \cdot 10^3$	$3.66 \cdot 10^4$	$1.50 \cdot 10^5$	(unseen)	(unseen)
GW190701.203306	$3.95 \cdot 10^3$	$9.28 \cdot 10^3$	$2.40 \cdot 10^3$	$4.75 \cdot 10^3$	$5.68 \cdot 10^3$	$6.22 \cdot 10^3$	$1.58 \cdot 10^4$	$1.70 \cdot 10^5$	(unseen)	(unseen)
GW190706.222641	$4.01 \cdot 10^3$	$1.01 \cdot 10^4$	$2.33 \cdot 10^3$	$3.42 \cdot 10^3$	$5.09 \cdot 10^3$	$8.71 \cdot 10^3$	$3.67 \cdot 10^4$	$7.51 \cdot 10^4$	(unseen)	(unseen)
GW190707.093326	$4.00 \cdot 10^3$	$1.01 \cdot 10^4$	$2.28 \cdot 10^3$	$3.43 \cdot 10^3$	$5.01 \cdot 10^3$	$8.68 \cdot 10^3$	$3.37 \cdot 10^4$	$6.94 \cdot 10^4$	(unseen)	(unseen)
GW190708.232457	$3.96 \cdot 10^3$	$9.56 \cdot 10^3$	$2.25 \cdot 10^3$	$4.32 \cdot 10^3$	$5.09 \cdot 10^3$	$8.59 \cdot 10^3$	$3.59 \cdot 10^4$	$1.17 \cdot 10^5$	(unseen)	(unseen)
GW190719.215514	$3.98 \cdot 10^3$	$1.00 \cdot 10^4$	$2.24 \cdot 10^3$	$3.46 \cdot 10^3$	$4.92 \cdot 10^3$	$8.56 \cdot 10^3$	$3.01 \cdot 10^4$	$6.40 \cdot 10^4$	(unseen)	(unseen)
GW190720.000836	$3.94 \cdot 10^3$	$9.67 \cdot 10^3$	$2.27 \cdot 10^3$	$4.63 \cdot 10^3$	$4.90 \cdot 10^3$	$8.31 \cdot 10^3$	$4.12 \cdot 10^4$	$9.52 \cdot 10^4$	$3.43 \cdot 10^1$	$4.78 \cdot 10^1$
GW190727.060333	$3.96 \cdot 10^3$	$9.63 \cdot 10^3$	$2.24 \cdot 10^3$	$4.65 \cdot 10^3$	$4.93 \cdot 10^3$	$8.42 \cdot 10^3$	$4.04 \cdot 10^4$	$9.14 \cdot 10^4$	$3.64 \cdot 10^1$	$5.10 \cdot 10^1$
GW190728.064510	$6.46 \cdot 10^3$	$1.53 \cdot 10^4$	$3.85 \cdot 10^3$	$8.07 \cdot 10^3$	$4.85 \cdot 10^3$	$7.68 \cdot 10^3$	$3.49 \cdot 10^4$	$1.18 \cdot 10^5$	$3.57 \cdot 10^1$	$4.00 \cdot 10^1$
GW190731.140936	$3.92 \cdot 10^3$	$9.05 \cdot 10^3$	$2.28 \cdot 10^3$	$5.05 \cdot 10^3$	$4.69 \cdot 10^3$	$8.83 \cdot 10^3$	$3.11 \cdot 10^4$	$8.31 \cdot 10^4$	$3.48 \cdot 10^1$	$4.50 \cdot 10^1$
GW190803.022701	$3.95 \cdot 10^3$	$9.08 \cdot 10^3$	$2.29 \cdot 10^3$	$4.87 \cdot 10^3$	$5.56 \cdot 10^3$	$8.24 \cdot 10^3$	$3.40 \cdot 10^4$	$1.99 \cdot 10^5$	(unseen)	(unseen)
GW190814	$6.48 \cdot 10^3$	$1.61 \cdot 10^4$	$3.44 \cdot 10^3$	$6.30 \cdot 10^3$	$4.69 \cdot 10^3$	$8.55 \cdot 10^3$	$1.17 \cdot 10^4$	$4.68 \cdot 10^4$	(unseen)	(unseen)
GW190828.063405	$4.01 \cdot 10^3$	$1.01 \cdot 10^4$	$2.37 \cdot 10^3$	$3.63 \cdot 10^3$	$5.11 \cdot 10^3$	$8.74 \cdot 10^3$	$4.10 \cdot 10^4$	$8.06 \cdot 10^4$	(unseen)	(unseen)
GW190909.114149	$3.99 \cdot 10^3$	$9.75 \cdot 10^3$	$2.19 \cdot 10^3$	$3.57 \cdot 10^3$	$4.98 \cdot 10^3$	$8.66 \cdot 10^3$	$2.77 \cdot 10^4$	$6.41 \cdot 10^4$	(unseen)	(unseen)
GW190910.112807	$6.49 \cdot 10^3$	$1.57 \cdot 10^4$	$3.70 \cdot 10^3$	$7.40 \cdot 10^3$	$5.04 \cdot 10^3$	$8.78 \cdot 10^3$	$3.68 \cdot 10^4$	$1.11 \cdot 10^5$	(unseen)	(unseen)
GW190924.021846	$6.49 \cdot 10^3$	$1.51 \cdot 10^4$	$3.85 \cdot 10^3$	$7.96 \cdot 10^3$	$5.67 \cdot 10^3$	$7.11 \cdot 10^3$	$2.31 \cdot 10^4$	$2.06 \cdot 10^5$	(unseen)	(unseen)
GW190929.012149	$4.00 \cdot 10^3$	$1.01 \cdot 10^4$	$2.34 \cdot 10^3$	$3.77 \cdot 10^3$	$5.06 \cdot 10^3$	$8.66 \cdot 10^3$	$4.06 \cdot 10^4$	$7.99 \cdot 10^4$	(unseen)	(unseen)
GW190930.133541	$3.81 \cdot 10^3$	$9.84 \cdot 10^3$	$2.01 \cdot 10^3$	$5.05 \cdot 10^3$	$5.55 \cdot 10^3$	$1.10 \cdot 10^4$	$4.97 \cdot 10^4$	$1.51 \cdot 10^5$	(unseen)	(unseen)

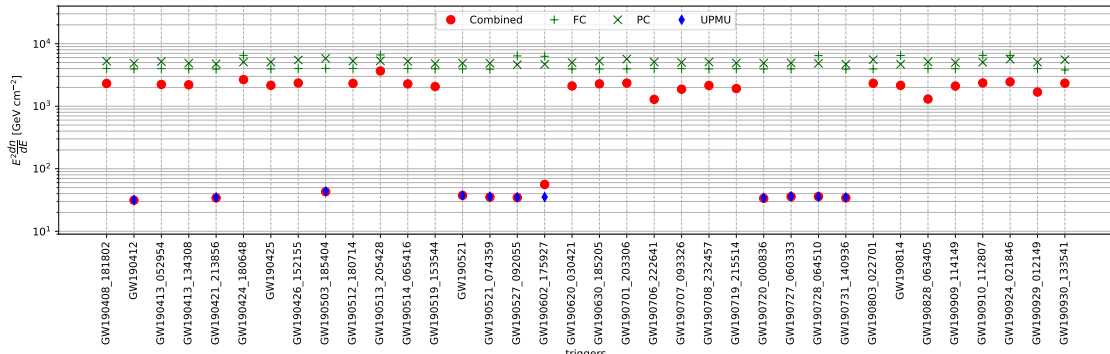
Results can also be summarised in plots, with horizontal=trigger and vertical=limits, like presented in [Figure 51](#). Also, we compute the fluence limit for Low energy sample. [Plot Figure 52](#) shows all triggers in low energy region.

8.3 Total energy limits

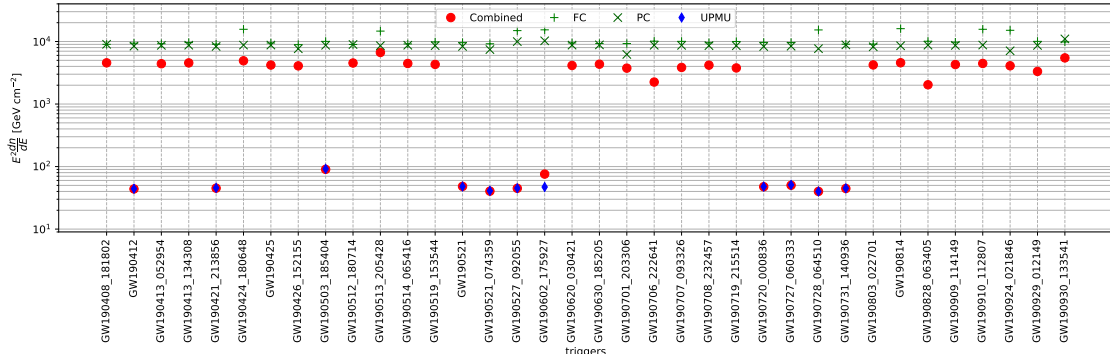
As discussed in [section 5.7](#), we can compute upper limits on the isotropic energy emitted in neutrinos by the source. They are presented in the [Table 18](#) and in the [Figure 53](#).

Trigger	d_{GW} [Mpc]	ν_{μ}	$\bar{\nu}_{\mu}$	ν_e	$\bar{\nu}_e$	All-flavours
GW190408_181802	1548	$1.85 \cdot 10^{58}$	$3.63 \cdot 10^{58}$	$1.44 \cdot 10^{58}$	$2.48 \cdot 10^{58}$	$3.13 \cdot 10^{58}$
GW190412	734	$5.25 \cdot 10^{55}$	$7.33 \cdot 10^{55}$	$3.54 \cdot 10^{57}$	$7.80 \cdot 10^{57}$	$1.81 \cdot 10^{56}$
GW190413_052954	4190	$1.41 \cdot 10^{59}$	$2.79 \cdot 10^{59}$	$1.16 \cdot 10^{59}$	$2.07 \cdot 10^{59}$	$2.51 \cdot 10^{59}$
GW190413_134308	5182	$2.11 \cdot 10^{59}$	$4.36 \cdot 10^{59}$	$1.75 \cdot 10^{59}$	$3.36 \cdot 10^{59}$	$3.81 \cdot 10^{59}$
GW190421_213856	3166	$1.25 \cdot 10^{57}$	$1.64 \cdot 10^{57}$	$8.18 \cdot 10^{58}$	$1.77 \cdot 10^{59}$	$4.25 \cdot 10^{57}$
GW190424_180648	2568	$7.45 \cdot 10^{58}$	$1.31 \cdot 10^{59}$	$9.08 \cdot 10^{58}$	$1.61 \cdot 10^{59}$	$1.30 \cdot 10^{59}$
GW190425	157	$1.92 \cdot 10^{56}$	$3.71 \cdot 10^{56}$	$1.97 \cdot 10^{56}$	$3.83 \cdot 10^{56}$	$3.40 \cdot 10^{56}$
GW190426_152155	377	$1.21 \cdot 10^{57}$	$2.11 \cdot 10^{57}$	$9.96 \cdot 10^{56}$	$1.92 \cdot 10^{57}$	$2.10 \cdot 10^{57}$
GW190503_185404	1527	$3.45 \cdot 10^{56}$	$7.31 \cdot 10^{56}$	$1.70 \cdot 10^{58}$	$3.37 \cdot 10^{58}$	$1.38 \cdot 10^{57}$
GW190512_180714	1462	$1.69 \cdot 10^{58}$	$3.32 \cdot 10^{58}$	$1.33 \cdot 10^{58}$	$2.28 \cdot 10^{58}$	$2.87 \cdot 10^{58}$
GW190513_205428	2190	$6.21 \cdot 10^{58}$	$1.12 \cdot 10^{59}$	$4.96 \cdot 10^{58}$	$8.41 \cdot 10^{58}$	$1.05 \cdot 10^{59}$
GW190514_065416	4988	$2.15 \cdot 10^{59}$	$4.25 \cdot 10^{59}$	$1.73 \cdot 10^{59}$	$3.04 \cdot 10^{59}$	$3.70 \cdot 10^{59}$
GW190519_153544	3024	$6.59 \cdot 10^{58}$	$1.40 \cdot 10^{59}$	$6.38 \cdot 10^{58}$	$1.11 \cdot 10^{59}$	$1.21 \cdot 10^{59}$
GW190521	4567	$2.77 \cdot 10^{57}$	$3.67 \cdot 10^{57}$	$1.69 \cdot 10^{59}$	$3.47 \cdot 10^{59}$	$8.86 \cdot 10^{57}$
GW190521_074359	1244	$1.94 \cdot 10^{56}$	$2.16 \cdot 10^{56}$	$1.23 \cdot 10^{58}$	$2.67 \cdot 10^{58}$	$6.09 \cdot 10^{56}$
GW190527_092055	3563	$6.21 \cdot 10^{60}$	$1.04 \cdot 10^{61}$	$1.34 \cdot 10^{61}$	$1.37 \cdot 10^{61}$	$1.43 \cdot 10^{61}$
GW190602_175927	3138	$2.36 \cdot 10^{57}$	$3.15 \cdot 10^{57}$	$1.79 \cdot 10^{59}$	$3.80 \cdot 10^{59}$	$8.22 \cdot 10^{57}$
GW190620_030421	3211	$7.50 \cdot 10^{58}$	$1.49 \cdot 10^{59}$	$8.65 \cdot 10^{58}$	$1.70 \cdot 10^{59}$	$1.39 \cdot 10^{59}$
GW190630_185205	956	$9.44 \cdot 10^{57}$	$1.58 \cdot 10^{58}$	$8.08 \cdot 10^{57}$	$1.56 \cdot 10^{58}$	$1.60 \cdot 10^{58}$
GW190701_203306	2152	$3.66 \cdot 10^{58}$	$5.84 \cdot 10^{58}$	$3.31 \cdot 10^{58}$	$7.42 \cdot 10^{58}$	$6.79 \cdot 10^{58}$
GW190706_222641	5184	$1.11 \cdot 10^{59}$	$1.83 \cdot 10^{59}$	$2.09 \cdot 10^{59}$	$3.06 \cdot 10^{59}$	$1.97 \cdot 10^{59}$
GW190707_093326	791	$4.60 \cdot 10^{57}$	$9.26 \cdot 10^{57}$	$5.30 \cdot 10^{57}$	$8.16 \cdot 10^{57}$	$8.20 \cdot 10^{57}$
GW190708_232457	888	$5.44 \cdot 10^{57}$	$1.08 \cdot 10^{58}$	$6.29 \cdot 10^{57}$	$1.17 \cdot 10^{58}$	$9.95 \cdot 10^{57}$
GW190719_215514	4786	$2.02 \cdot 10^{59}$	$2.94 \cdot 10^{59}$	$1.82 \cdot 10^{59}$	$2.89 \cdot 10^{59}$	$3.15 \cdot 10^{59}$
GW190720_000836	906	$1.34 \cdot 10^{56}$	$1.72 \cdot 10^{56}$	$8.87 \cdot 10^{57}$	$1.92 \cdot 10^{58}$	$4.34 \cdot 10^{56}$
GW190727_060333	3609	$1.63 \cdot 10^{57}$	$2.28 \cdot 10^{57}$	$1.00 \cdot 10^{59}$	$2.09 \cdot 10^{59}$	$5.62 \cdot 10^{57}$
GW190728_064510	858	$9.10 \cdot 10^{55}$	$9.83 \cdot 10^{55}$	$8.40 \cdot 10^{57}$	$1.76 \cdot 10^{58}$	$2.84 \cdot 10^{56}$
GW190731_140936	4034	$2.27 \cdot 10^{57}$	$2.94 \cdot 10^{57}$	$1.48 \cdot 10^{59}$	$3.16 \cdot 10^{59}$	$7.51 \cdot 10^{57}$
GW190803_022701	3750	$1.21 \cdot 10^{59}$	$2.13 \cdot 10^{59}$	$1.13 \cdot 10^{59}$	$2.59 \cdot 10^{59}$	$2.30 \cdot 10^{59}$
GW190814	241	$3.82 \cdot 10^{56}$	$8.12 \cdot 10^{56}$	$3.23 \cdot 10^{56}$	$6.43 \cdot 10^{56}$	$7.05 \cdot 10^{56}$
GW190828_063405	2160	$1.82 \cdot 10^{58}$	$2.34 \cdot 10^{58}$	$3.58 \cdot 10^{58}$	$5.58 \cdot 10^{58}$	$3.13 \cdot 10^{58}$
GW190909_114149	4924	$2.40 \cdot 10^{59}$	$4.87 \cdot 10^{60}$	$7.96 \cdot 10^{60}$	$4.99 \cdot 10^{60}$	$3.78 \cdot 10^{59}$
GW190910_112807	1670	$2.38 \cdot 10^{58}$	$4.38 \cdot 10^{58}$	$3.46 \cdot 10^{58}$	$6.50 \cdot 10^{58}$	$4.39 \cdot 10^{58}$
GW190924_021846	572	$2.80 \cdot 10^{57}$	$4.61 \cdot 10^{57}$	$2.60 \cdot 10^{57}$	$5.72 \cdot 10^{57}$	$5.27 \cdot 10^{57}$
GW190929_012149	3902	$8.18 \cdot 10^{58}$	$2.26 \cdot 10^{59}$	$2.00 \cdot 10^{59}$	$2.08 \cdot 10^{59}$	$1.43 \cdot 10^{59}$
GW190930_133541	786	$5.22 \cdot 10^{57}$	$1.17 \cdot 10^{58}$	$4.47 \cdot 10^{57}$	$1.07 \cdot 10^{58}$	$1.00 \cdot 10^{58}$

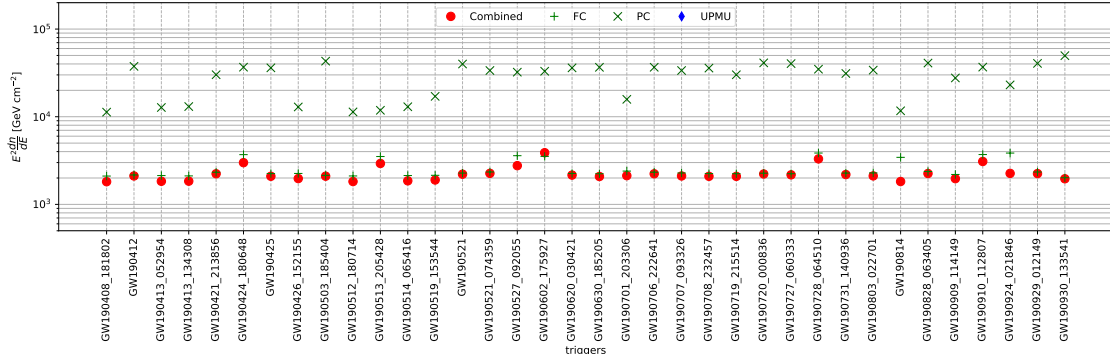
Table 18: 90% upper limits on E_{iso} [in erg] either flavour-by-flavour or by combining flavours and putting limits on the all-flavour emission, assuming equipartition.



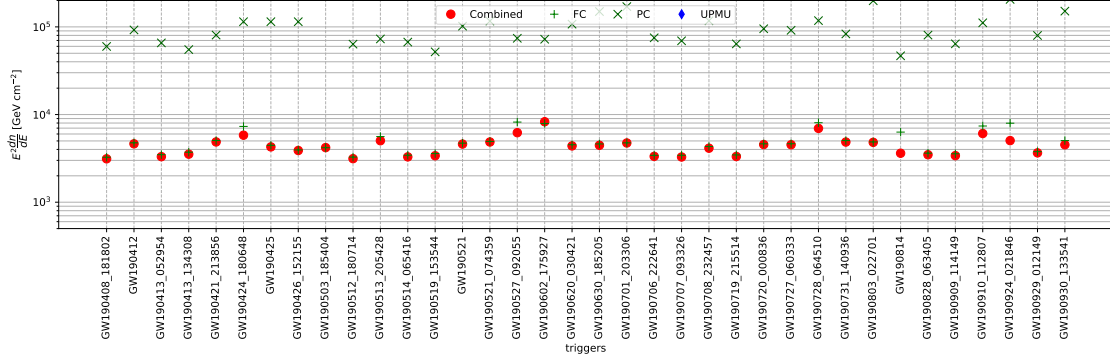
(a) ν_μ



(b) $\bar{\nu}_\mu$



(c) ν_e



(d) $\bar{\nu}_e$

Figure 51: Summary of all flux limits.

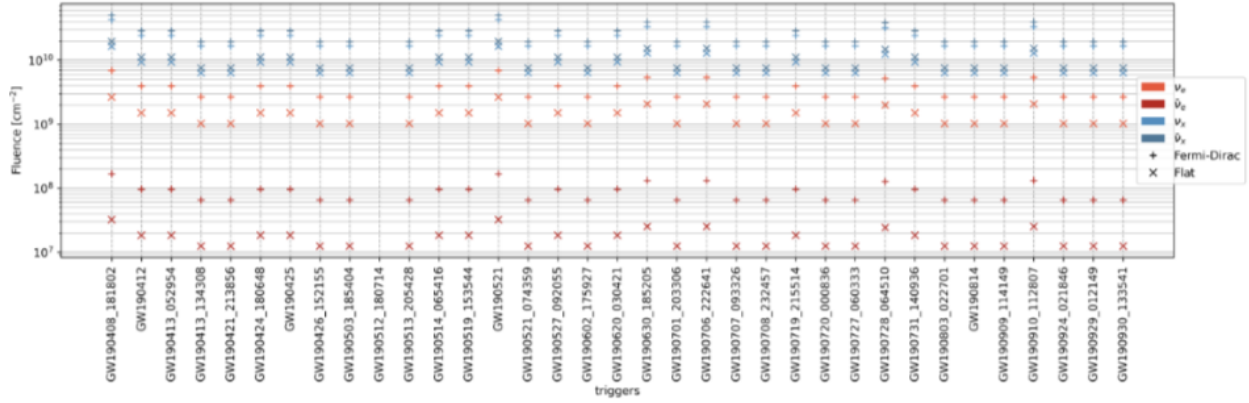


Figure 52: LOW energy triggers fluence limit

9 Summary and Outlook

9.1 Summary

In this thesis, neutrinos related to gravitational waves are searched for in SK detectors. Gravitational waves can be produced by the merger of binary neutron stars and black holes. Among them, the merger of neutron stars is believed to produce light, gamma rays, neutrinos, etc. in addition to gravitational waves. According to different models at present, the energy of the neutrinos produced is different, and detecting neutrinos will help us to study the models of binary neutron star merger.

Until now, no clear neutrino signal is observed with GW. In the previous study of SK, neutrinos for GW170817 in SK were searched for and no significant signal found. In this study, 56 GWs for O3(from Apr. 2019 to Mar. 2020) and 39 GWs for O3a (from Apr. 2019 to Sep. 2019) are the target. After reduction process in SK, 46 events remain in the search window(for O3) and 36 events for O3a, ± 500 sec around each GWs trigger time, while the background rate is 0.111 events/1000 sec for FC, 0.007 events/1000 sec for PC, 0.016 events/1000 sec for UPMU and 0.729 events/1000 sec for LOW energy sample(energy $< 100\text{MeV}$). No obvious excess was seen in the time development of the number of events and energy distribution of the combined data.

Although we did not find a significant signal in this study, we can compute Upper-limit for each flavors in both High energy and Low energy. For High energy, we assume E^{-2} neutrinos spectrum to compute the flux limit. For Low energy, we assume Fermi-Dirac Distribution(average 20 MeV), Flat and mono-energetic spectrum to calculate Fluence-Limit. In both cases, the detailed results have been presented. We also compute the isotropic total neutrino energy limits for each neutrino flavors. Assuming isotropic emissions among the different flavors, upper limits on the total energy as E_{iso} of each types of neutrinos were derived. The limits on E_{iso} for individual GW events, and combined all GW events at each neutrino flavor are shown in Table 18 and Figure 53.

9.2 Outlook

The focus of this research is on the O3 and O3a phases, but as this paper presented in section 3.3, LIGO will start the O4 phase (See section 3.2) at next year. In O4 phase, the expected events for GWs are 1 per day. For SK detector, SK-Gd has started. In SK-Gd, 0.2% gadolinium sulfate $\text{Gd}(\text{SO}_4)_3$ is added to the SK water in order to identify $\bar{\nu}_e$ events. The identify of $\bar{\nu}_e$ is useful for the detection of supernova relic neutrino and direction of supernova bursts(Which is the background of GW research). Gadolinium captures a neutrino from inverse beta decay and emits gamma rays of 8MeV total energy (Figure 54)

In O4 phase, the background of Low energy case will be changed because of SK-Gd. Also more data can be used and significant neutrino signal is expected be found.

In our current automatic system, realtime analysis is not possible, however, development a real-time system is critical to get neutrino signals more quickly.

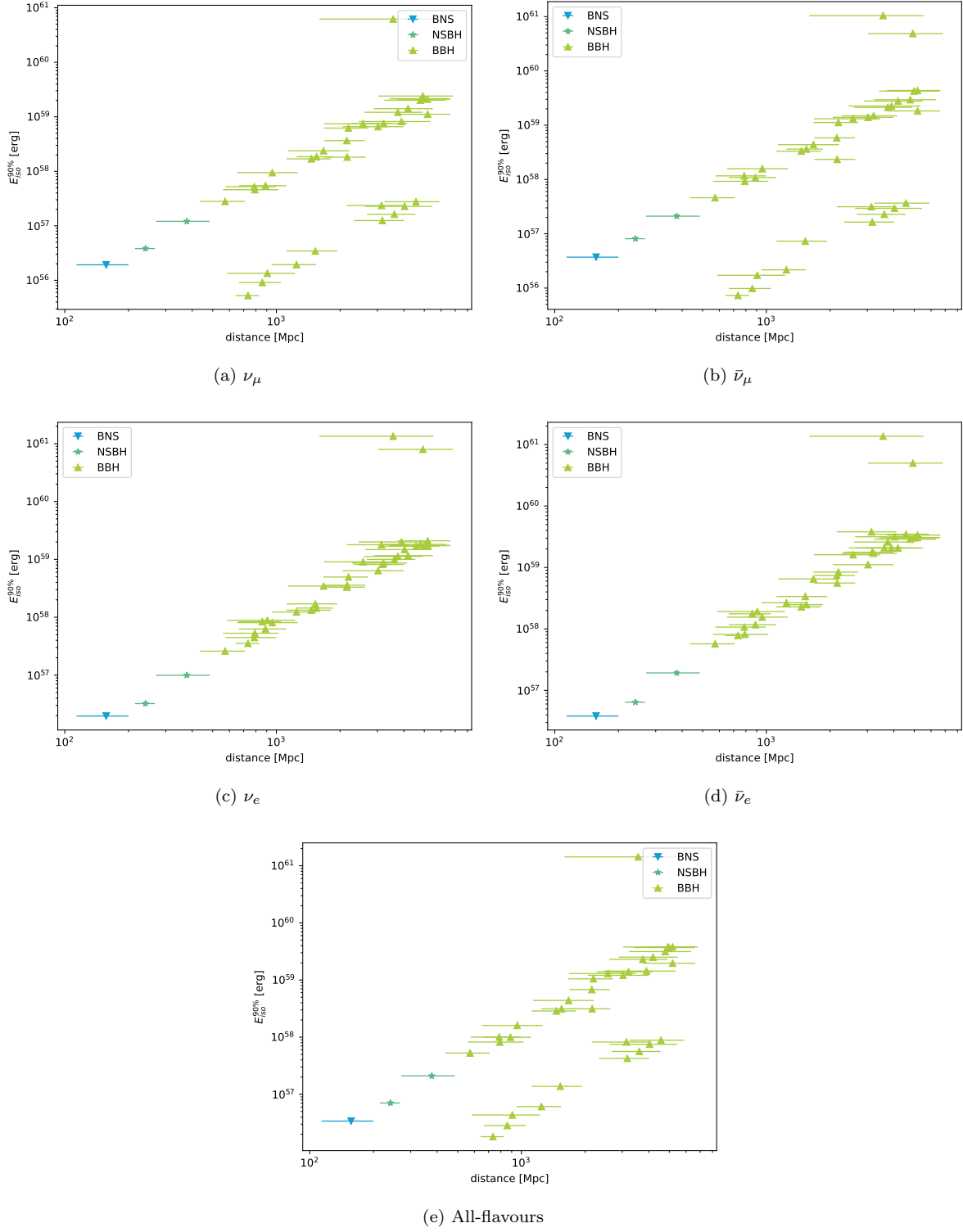


Figure 53: 90% upper limits on E_{iso} [in erg] (either flavour-by-flavour or by combining flavours and putting limits on the all-flavour emission, assuming equipartition), as a function of source distance and separating by source type.

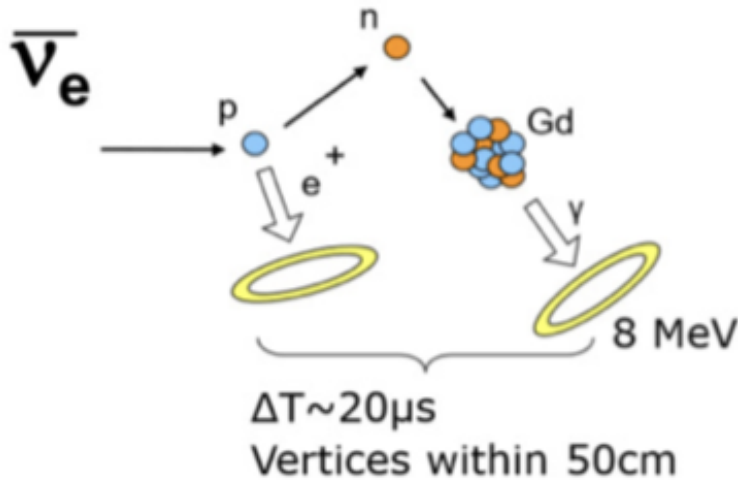


Figure 54: Neutron tagging with gadolinium.[28]

Acknowledgement

Thanks As an international student, the study life of a half-year graduate student and a two-year master in Japan is very fulfilling and rich. When I first came to Japan, communication and communication seemed a little difficult due to language problems. With the careful guidance of teacher Koshio-san, Harada-san of D1, and the help of Okada-san and Sakai-san who are both M2, I gradually got used to life in Japan. Thank you teachers and everyone for your concern for me. After I officially became a master student, the tutor Koshio-san was very dedicated to guiding my research. At the same time, I also communicated with the members of SK, which made me progress. I would like to thank my tutors for their guidance in learning, and also thank all SK members for their help in my research. At the same time, in the research room, we will hold a meeting once a week. During the meeting, everyone will introduce the content of their research and also study the paper. This also allows me to learn more than the content of my own research. know how. Thanks to the members of the research room, Special Researcher Ito-san, Harada-san of D1, Sakai-san and Okada-san of M2, Kitagawa-san of M1, Nakanishi-san of B4, and Shiraishi-san, Tano-san of B3. Finally, I would like to thank Yamamoto-san and Koeda-san, the clerks of the research office, for your support for making my research life smooth.

Thanks to the teachers and everyone who have always supported and encouraged me. It was your support and help that allowed me to complete my two-year research life as a master student.

References

- [1] M. G. Aartsen et al. A Search for MeV to TeV Neutrinos from Fast Radio Bursts with IceCube. 2019.
- [2] M. G. Aartsen et al. IceCube Search for Neutrinos Coincident with Compact Binary Mergers from LIGO-Virgo’s First Gravitational-Wave Transient Catalog IceCube Collaboration. Technical report, 2020.
- [3] B. P. Abbott, R. Abbott, T. Abbott, M. Abernathy, F. Acernese, K. Ackley, C. Adams, T. Adams, P. Addesso, R. Adhikari, et al. Gw150914: The advanced ligo detectors in the era of first discoveries. *Physical review letters*, 116(13):131103, 2016.
- [4] B. P. Abbott, R. Abbott, T. Abbott, M. Abernathy, F. Acernese, K. Ackley, C. Adams, T. Adams, P. Addesso, R. Adhikari, et al. Observation of gravitational waves from a binary black hole merger. *Physical review letters*, 116(6):061102, 2016.
- [5] B. P. Abbott, R. Abbott, T. Abbott, M. Abernathy, F. Acernese, K. Ackley, C. Adams, T. Adams, P. Addesso, R. Adhikari, et al. Observing gravitational-wave transient gw150914 with minimal assumptions. *Physical Review D*, 93(12):122004, 2016.
- [6] B. P. Abbott, R. Abbott, T. Abbott, M. Abernathy, F. Acernese, K. Ackley, C. Adams, T. Adams, P. Addesso, R. Adhikari, et al. Properties of the binary black hole merger gw150914. *Physical review letters*, 116(24):241102, 2016.
- [7] R. Abbott et al. GWTC-2: Compact Binary Coalescences Observed by LIGO and Virgo During the First Half of the Third Observing Run. 10 2020.
- [8] K. Abe et al. Search for Neutrinos in Super-Kamiokande associated with Gravitational Wave Events GW150914 and GW151226. 08 2016.
- [9] K. Abe et al. Search for Neutrinos in Super-Kamiokande associated with the GW170817 neutron-star merger. *The Astrophysical Journal*, 857(1):L4, 02 2018.
- [10] B. Baret et al. Multimessenger Science Reach and Analysis Method for Common Sources of Gravitational Waves and High-energy Neutrinos. Technical report, 12 2011.
- [11] S. Barthelmy. Gcn: The gamma-ray coordinates network. <https://gcn.gsfc.nasa.gov/>.
- [12] L. Blanchet, T. Damour, B. R. Iyer, C. M. Will, and A. G. Wiseman. Gravitational-radiation damping of compact binary systems to second post-newtonian order. *Physical Review Letters*, 74(18):3515, 1995.
- [13] J. Braun, J. Dumm, F. De Palma, C. Finley, A. Karle, and T. Montaruli. Methods for point source analysis in high energy neutrino telescopes. *Astroparticle Physics*, 29(4):299–305, 2008.
- [14] O. Caballero. Neutrino emission, equation of state and the role of strong gravity. In *AIP Conference Proceedings*, volume 1753, page 040002. AIP Publishing LLC, 2016.
- [15] M. Campanelli, C. O. Lousto, P. Marronetti, and Y. Zlochower. Accurate evolutions of orbiting black-hole binaries without excision. *Physical Review Letters*, 96(11):111101, 2006.
- [16] S. Chatterji, L. Blackburn, G. Martin, and E. Katsavounidis. Multiresolution techniques for the detection of gravitational-wave bursts. *Classical and Quantum Gravity*, 21(20):S1809–S1818, sep 2004.
- [17] N. J. Cornish and T. B. Littenberg. Bayeswave: Bayesian inference for gravitational wave bursts and instrument glitches. *Classical and Quantum Gravity*, 32(13):135012, 2015.
- [18] S. Fukuda et al. Search for Neutrinos from Gamma-Ray Bursts Using Super-Kamiokande. *The Astrophysical Journal*, 578(1):317–324, 10 2002.
- [19] S. Fukuda, Y. Fukuda, T. Hayakawa, E. Ichihara, M. Ishitsuka, Y. Itow, T. Kajita, J. Kameda, K. Kaneyuki, S. Kasuga, et al. The super-kamiokande detector. *Nuclear Instruments and Methods in Physics Research Section A: Accelerators, Spectrometers, Detectors and Associated Equipment*, 501(2-3):418–462, 2003.
- [20] É.ourgoulhon. *Special relativity in general frames*. Springer, 2016.

- [21] K. Hagiwara et al. Search for Astronomical Neutrinos from Blazar TXS 0506+056 in Super-Kamiokande. *The Astrophysical Journal Letters*, 887:L6, 2019.
- [22] R. Hussain, J. Vandenbroucke, and J. Wood. A Search for IceCube Neutrinos from the First 33 Detected Gravitational Wave Events. 2019.
- [23] R. P. Kraft, D. N. Burrows, and J. A. Nousek. Determination of Confidence Limits for Experiments with Low Numbers of Counts. *Astrophysical Journal*, 374:344, June 1991.
- [24] A. Le Tiec and J. Novak. Theory of gravitational waves. In *An Overview of Gravitational Waves: Theory, Sources and Detection*, pages 1–41. World Scientific, 2017.
- [25] LSC. Gracedb gravitational-wave candidate event database. <https://gracedb.ligo.org/>.
- [26] A. H. Mroue, M. A. Scheel, B. Szilagyi, H. P. Pfeiffer, M. Boyle, D. A. Hemberger, L. E. Kidder, G. Lovelace, S. Ossokine, N. W. Taylor, et al. Catalog of 174 binary black hole simulations for gravitational wave astronomy. *Physical Review Letters*, 111(24):241104, 2013.
- [27] H. Nishino, K. Awai, Y. Hayato, S. Nakayama, K. Okumura, M. Shiozawa, A. Takeda, K. Ishikawa, A. Minegishi, and Y. Arai. High-speed charge-to-time converter asic for the super-kamiokande detector. *Nuclear Instruments and Methods in Physics Research Section A: Accelerators, Spectrometers, Detectors and Associated Equipment*, 610(3):710–717, 2009.
- [28] A. Orii. *Search for Neutrinos associated with Gamma-ray Bursts in Super-Kamiokande*. PhD thesis, School of Science, The University of Tokyo, 2018.
- [29] A. Suzuki, M. Mori, K. Kaneyuki, T. Tanimori, J. Takeuchi, H. Kyushima, and Y. Ohashi. Improvement of 20 in. diameter photomultiplier tubes. *Nuclear Instruments and Methods in Physics Research Section A: Accelerators, Spectrometers, Detectors and Associated Equipment*, 329(1-2):299–313, 1993.
- [30] E. Thrane et al. Search for neutrinos from GRB 080319B at super-kamiokande. *Astrophysical Journal*, 697(1):730–734, 03 2009.
- [31] D. Veske, Z. Márka, I. Bartos, and S. Márka. Neutrino emission upper limits with maximum likelihood estimators for joint astrophysical neutrino searches with large sky localizations. *JCAP*, 05:016, 2020.
- [32] S. Yamada, K. Awai, Y. Hayato, K. Kaneyuki, Y. Kouzuma, S. Nakayama, H. Nishino, K. Okumura, Y. Obayashi, Y. Shimizu, et al. Commissioning of the new electronics and online system for the super-kamiokande experiment. *IEEE Transactions on Nuclear Science*, 57(2):428–432, 2010.